Static Tire Characterization for Race Vehicle Setup

By

Devin Michael Clancy

Thesis submitted to the faculty of the Virginia Polytechnic Institute and State University
in partial fulfillment of the requirements for the degree of

Master of Science
In
Mechanical Engineering

Saied Taheri, Chair
John B. Ferris
Robert L. West

November 14, 2011
Blacksburg, VA

Keywords: Tire, Static tire analysis, Racing

Static Tire Characterization for Race Vehicle Setup

By

Devin Michael Clancy

Abstract

In order to provide data for non-rolling tire models that are used in computer simulations of vehicle dynamics, a tire test rig is designed and manufactured which attaches to an MTS kinematics and compliance machine. This test rig is developed for the purpose of characterizing the loaded radius, overturning moment, and displacement of multiple tires in the vertical, lateral, and longitudinal test axes. Equations are developed and used to fit these parameters for the purpose of representing them in non-rolling vehicle simulation models.

Acknowledgements

I offer my sincerest gratitude and love to my family, Patrick, Annemarie, and Sean Clancy. For without their continued support, encouragement, and countless packages filled with coffee and candy, I would not have made it through this degree.

All photos in thesis document taken by author, 2011.

Table of Contents

List of Tables

List of Figures

1. Introduction

1.1. Background

Despite the influx of computer simulation into race engineering for prediction of vehicle setups, accurate simulation results cannot be obtained without the use of underlying equations which appropriately represent the state of the car which the simulation is attempting to replicate. One vehicle state in which current simulations fall short on is that of a static or non-rolling tire. Force and moment data for a rolling tire is provided for every tire run during a race season, but the data for a rolling tire is not related to that of static tire by any simple relationship (1).

The data for a static tire is important for vehicle simulations that predict the necessary suspension settings to achieve a particular vehicle setup. Procedures for suspension setup on a race car are still largely iterative due to the lack of relevant non-rolling tire data being implemented into the vehicle models that are used in chassis setup programs. Static tire data is also important in predicting the performance of a vehicle on a kinematics and compliance machine or pull-down test rig. These rigs are used to measure a vehicle's reaction to loading changes. Presently, though, the computer simulations of these tests do not correlate well with the testing results due to the computer simulations using a tire model based on data from a rolling tire.

Therefore, in order to gather static tire data, the project sponsor requests the design and implementation of an in-house, cost-effective test rig to be used for the static characterization of race tires.

1.2. Objectives

Tire testing is typically an expensive endeavor considering the scale of the machinery and automation involved. Industrial-sized belt drive machines such as the MTS Flat-Trac® Tire Test System offer dynamic tire testing capabilities on rolling test beds (2). These machines are large, expensive, and intended for OEM use. For more affordable, low volume tire testing, smaller versions of these machines have been developed, such as the RuotaVia (3), which use a rolling drum or dynamometer and a measuring and actuation hub. Not all applications require the measurement of rolling tire parameters, though, so non-rolling tire test rigs have been developed which utilize an a-frame support structure and automated platen to deflect the tire (4,5). In addition, frictionless platens and pneumatic actuators have also been used in order to apply lateral and longitudinal forces to non-rolling tires for measurement purposes (6).

Despite these variations of tire test rigs already developed, this project aims to develop a new test rig which non-permanently converts an MTS Kinematics and Compliance (K&C) machine into a non-rolling and vehicle independent tire test rig. The K&C machine is chosen as the base for the test rig because its actuation and measurement capabilities are well suited to tire testing.

In addition to the design and validation of a test rig, this project also encompasses the development of empirical fitting equations for test data such that it is possible to represent the measured tire characteristics into vehicle simulation programs. These fitting routines are to be incorporated into a production-ready MATLAB graphical user interface (GUI) which is used to post-process and fit the test data.

2. Test Rig Design

The design of the tire test rig is constrained to the MTS K&C machine at the request of the project sponsor. The functionality of the K&C machine makes an ideal starting point for a non-rolling tire test rig.

2.1. MTS K&C Machine

The MTS K&C machine is a full-scale vehicle testing tool used to measure the kinematics and compliance of a vehicle's suspension by controlling displacement or force inputs to the suspension at the tire contact patch while constraining the chassis. The MTS K&C machine that is used in this project is shown in Figure 2.1.

Figure 2.1: MTS K&C machine layout

The body of the vehicle is clamped to a static beam using four electro-magnetic clamps which attach to the vehicle chassis at the pinch-welds or custom designed pick-up points. Four independently controlled elevators, one at each wheel, are capable of vertical, lateral, longitudinal, and roll motions independent of one another. One of these elevators is shown in Figure 2.2.

Figure 2.2: MTS K&C machine elevator platform

The motion of each elevator is regulated through position or force control by the MTS control system. This control system provides up to 79 channels of data acquisition while utilizing 25 servo-control channels to regulate machine operation. The wheel interface platform on each elevator incorporates a six axis strain gauge load cell while providing the necessary control feedback as well as test data.

Test data is also acquired by motion sensors affixed to the wheel which are capable of tracking wheel position through a typical suspension's full operating range of motion. This motion tracking is accomplished by a six-jointed arm with encoders at each joint measuring position and orientation changes in the wheel. These position and orientation changes are longitudinal, lateral, and vertical translations as well as spin, steer, and camber angle rotations. Figure 2.3 depicts the standard MTS wheel motion sensor arm assembly.

Figure 2.3: MTS K&C machine wheel motion sensor arm

The design area on the K&C machine which is to be used for the tire test rig is shown in Figure 2.4. The electromagnetic clamps ride on an air bearing base for movement and are magnetically coupled to the static I-beam during testing. The static I-beam serves as the mass that reacts the loads applied to the chassis at the elevator pads. The elevator pads are capable of steer and camber inputs independent of the elevator motion and one another.

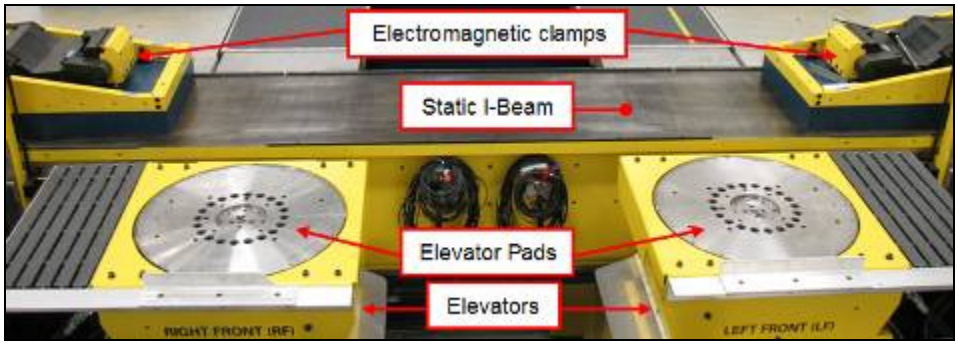

Figure 2.4: Identification of frame design workable area components

2.2. Rig Design Considerations

The capabilities of the K&C machine make it well suited for quasi-static tire testing. Wheel and pad displacements being measured independently, force or position control, and the numerous degrees of freedom of the pad cover most of the testing and control requirements of a tire test rig. With these capabilities as a starting point, the test rig is designed with the following criteria:

Table 2.1: Test Rig Design Considerations

Category	Criteria	Origin
Installation	Test rig must be a non-permanently installed fixture which is easily setup and removed from the MTS K&C machine	**Sponsor**
Layout	Test rig must adhere to a 60 inch track width	**Sponsor**
Layout	Test rig must accommodate two tires at a time	**Sponsor**
Automation	Test rig must be fully-automated in terms of tire indexing and pressure adjustment	**Sponsor**
Rig Stiffness	Test rig compliance should be reduced to a level which induces a possible measurement error which is exceeded by the tire to tire variation of race tires	**Sponsor**
Test Loads	Test rig must be able to withstand the following load ranges: • Vertical: [0:6000] lbf • Lateral: [-4000:4000] lbf • Longitudinal: [-5000:5000] lbf	**Sponsor**

Since the K&C rig is used on a weekly basis by race teams for engineering development, it is not possible for the tire test rig to be permanently fixated to the machine. In addition, since the majority of vehicles which are tested on the K&C rig operate at a 60 inch track width, the test rig must be designed to that same dimension. A different track width would require the machine's track width to be adjusted before and after each tire test from where it is set normally. A further reduction in setup and adjustment time is realized by designing the test rig to be capable of mounting two tires at once.

In order to facilitate test efficiency and decrease personnel demands during test session, the test rig must be fully automated. The K&C machine has its own programming language which allows custom tests to be written and looped. Therefore, in order to achieve full test automation, a method for remotely orienting and affixing the wheel and tire assembly as well as controlling inner and outer liner pressure must be developed. The wheel and tire assembly must be tested at multiple indices in order to avoid testing the tire on a belt splice which would yield erroneous stiffness results. These external systems must integrate with the internal MTS control system as inputs and respond to outputs from the controller.

The tire test rig stiffness goal is based off the tire to tire variation of a race tire, which is experimentally known to fall within a 5% range through measurement of tire forces and moments on a set of 34 of the same tires (7). While the stiffest test rig possible is the most ideal in terms of eliminating measurement error, it is not a practical design goal. The K&C rig, due to its wheel motion and elevator displacement sensors, is suited to account for the deflection of the test rig and remove it from the tire deflection data. Therefore, the test rig's stiffness is designed with the situation in mind that it may be retrofitted to another measurement machine such as a shaker rig in order to capture high frequency data. As a design goal, the rig's stiffness in a test axis must be high enough to not induce more than a 5% error in spring rate measurement. The deflection of the test rig affects overturning moment as well, but that error is not easily quantifiable, so spring rate is used as the standard. This additional possible measurement error is said to be acceptable because trends are more important than absolute magnitude in vehicle simulation due to the number of variables which are unaccounted for at present.

The range of test loads that is required of the test rig is dictated by the maximum loading of the tires during operation (8).

2.3. Frame

The K&C rig area which constrains the design of the tire test rig is shown in Figure 2.4. The layout of the tire test rig is driven by necessity to provide vertical, lateral, and longitudinal elevator actuation clearance at all inclination angles of the elevator pad while existing as a non-permanent fixture which achieves an effective 60 inch track width. In order to keep costs at a minimum, reduce manufacturing complexity, maximize compactness, and allow for simple modification while producing a stiff structure, a box frame design is chosen is chosen over a carbon monocoque or A-frame.

The only mounting option that is afforded by the K&C rig for the test rig frame is the electromagnetic clamps. The problem with using only these clamps to secure the test rig is that it yields a heavily cantilevered test rig since the maximum distance from the center of the clamp to the zero location of the center of the elevator pad is approximately 28 inches. This cantilever problem is addressed by designing the frame to allow for mounting attachments to be added to the bottom of vertical tubes which sit at positions slightly wider than and offset inboard from the elevator pads in order to allow for clearance for elevator pad motion. With these attachment points in mind and the fact that the test rig design requirement for two tires mounted at once necessitates a symmetrical design, Solidworks is used to generate a point cloud which is constrained by boundary planes and equations driven by the dimensional restrictions imposed by the layout of the K&C rig. This point cloud is used to generate a general frame layout using Solidworks'

weldment feature as seen in Figure 2.5. Diagonal connections between nodes are added for rigidity and the large center tube is used in order to provide ample surface area for connection of all the tubes which terminate at this location.

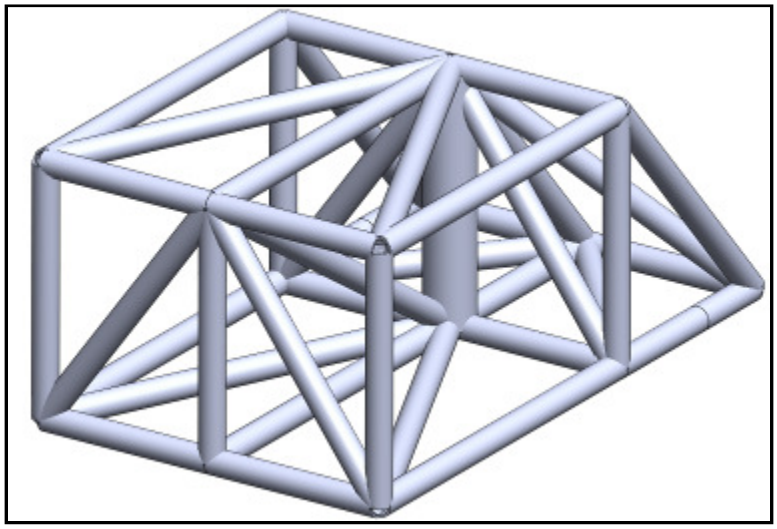

Figure 2.5: Base test rig frame

While the base frame design is influenced heavily by the bounding dimensions of the K&C rig in order to provide clearance for elevator travel while extending a mounting area back to the electro-magnetic clamps, the remaining tubes are designed to serve as a mounting point for the wheel and tire. These support tubes, shown in Figure 2.6, are oriented to react the forces applied in the major test loading axes, vertical, lateral, and longitudinal, mostly along the axis of at least one set of tubes. Figure 2.6 also illustrates the formatted look of the frame with notched tubing.

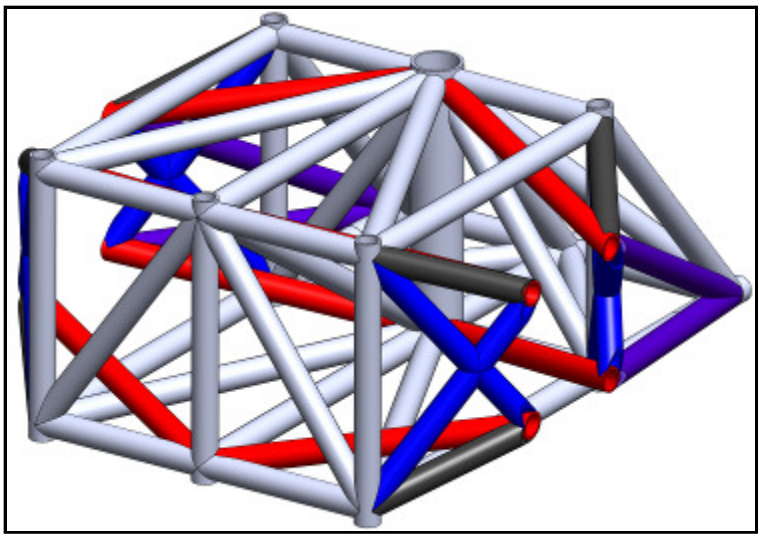

Figure 2.6: Wheel support tubing

The offset of these support tubes from the box frame is driven by the dimensions of the parts to be used for mounting the wheel and tire assembly such that a 60 inch track width is realized. Therefore, this dimension is continuously adjusted throughout the design of the test rig. The goal, though, is to have the wheel and tire assembly parts as short as possible and these tubes offset as far as possible in order to maximize the effective stiffness of the rig. The spacing of the nodes where these support tubes terminate as well as the width and height of the test frame are adjusted with the length of these tubes in order to avoid contact between the tubes at any point before where they terminate. This spacing is made as wide as possible in order to counteract the large overturning moments during testing.

Since the frame is a weldment, the wheel support tubes are welded to a plate, Figure 2.7, in order to facilitate post-assembly machining. Post machining is necessary on a welded frame in order to ensure that it is square with respect to its mounting points in order to eliminate any toe or camber bias that is imparted during welding and machining. This plate also serves as a generic mounting source so the components which are bolted

outboard of the frame can be changed for future testing. The bill of materials for all of these components is found in Appendix A.

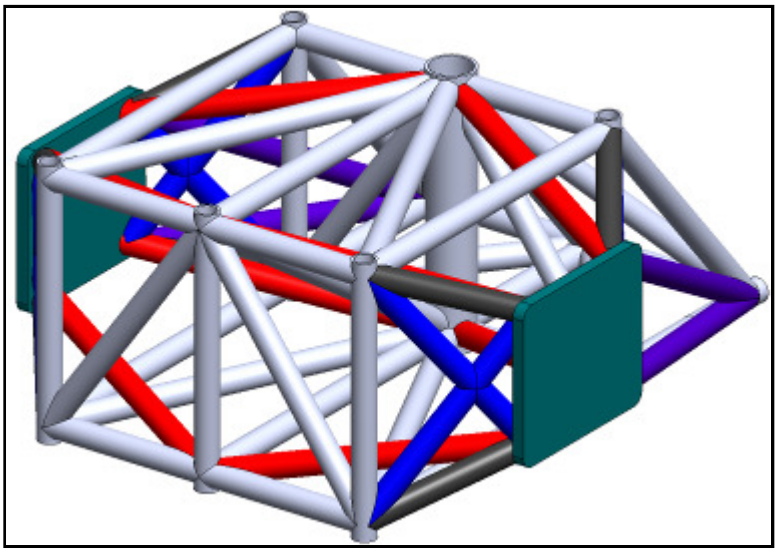

Figure 2.7: Frame flange plate

2.4. Mounting

With the basic layout of the main frame structure established, the attachment of the rig to the K&C machine is established. Figure 2.8 shows the electro-magnetic clamps which provide an ideal mounting point for the frame. The air bearing base of these clamps allows for easy positioning of the test rig, and a strong mounting point is ensured as the clamp base is magnetically coupled to the static I-beam of the K&C rig.

Figure 2.8: Electro-magnetic clamps

Figure 2.9 illustrates welded mounts which attach the frame to the bolt pattern on the base of the electro-magnetic clamps. This frame-to-clamp mount is a second-iteration design as the initially manufactured clamp mount design proved insufficient maintaining the position of the frame in test conditions. This clamp mount design is utilized because it allows for repeatable positioning and leveling of the tire test rig while providing the strength necessary to react the forces at the clamp mounts over the range of possible test loads as shown in Appendix B.

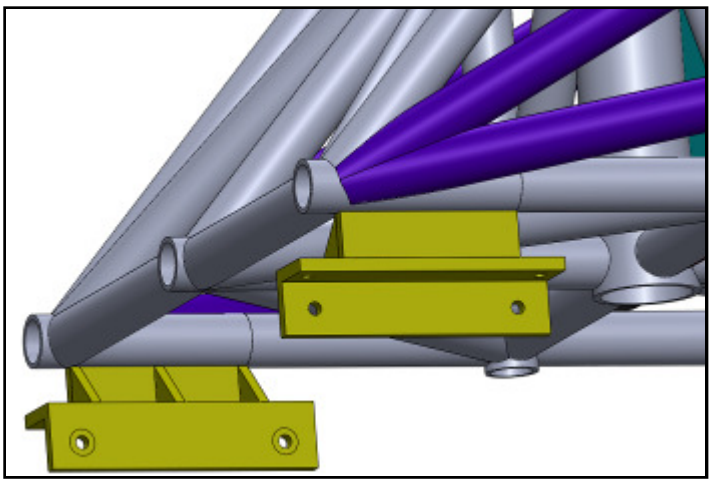

Figure 2.9: Clamp mount design

In order to reduce the cantilever length of the point of force application to the clamp mounts, the frame is designed with vertical tubes which act as nodes that sit fore and aft of the elevator pad. The lack of direct mounting options on the K&C rig at these locations necessitates connecting the frame to a remote mounting location. The vertical tubes closest to the electro-magnetic clamps terminate 10.5 inches above the front of the static I-beam of the K&C rig, and the foremost vertical tubes terminate 92.75 inches above nothing but a concrete floor. Therefore, the frame is connected to the static I-beam and the floor with solid connecting rods as shown in Figure 2.10.

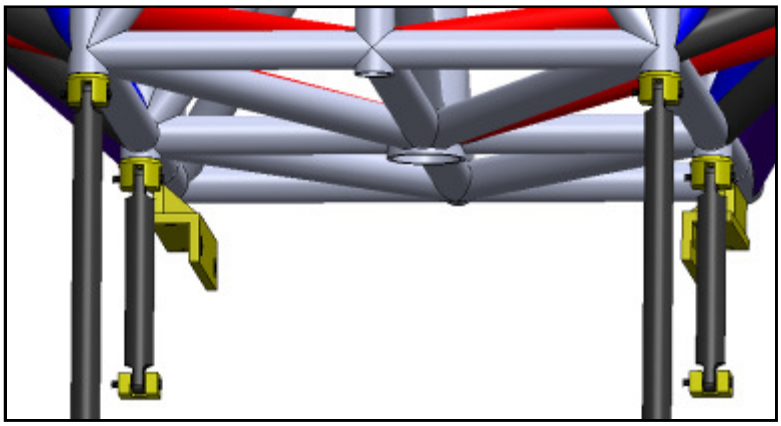

Figure 2.10: Connecting rod layout

These solid connecting rods will take the majority of the vertical loading that is applied to the tire while providing a stiff connection which is fundamental of a solid rod in tension. The initial design of this connection used turnbuckles with rod ends instead of solid connecting rods. The design intent of these turnbuckles was to pre-tension the frame as to reduce frame defection. Unfortunately, these turnbuckles lead to increased setup variability, the rod ends deflected heavily, and the design contributed negligibly to the overall stiffness of the test rig. Therefore, solid connecting rods are used.

Figure 2.11 shows the connection between the connecting rods and the frame with a welded clevis end. This eyelet design is used at each of the bottom four corners of the test rig frame. Calculations and details for all critical bolts and pins are found in Appendix C.

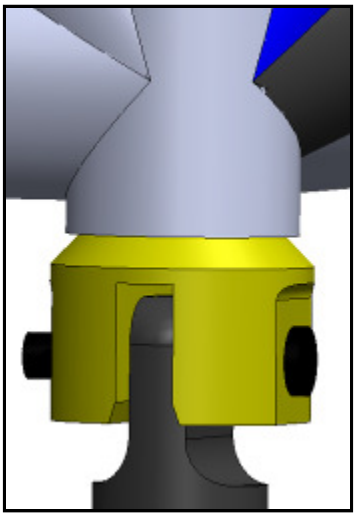

Figure 2.11: Connection rod frame mounting

The link between the front two connecting rods and the floor is established by a clevis mount welded to a large square plate as illustrated in Figure 2.12. This clevis mount is designed to distribute the load from the connecting rods over a large area of the plate. Because the floor under the K&C rig is concrete, this plate is attached to the floor using epoxy-set concrete anchors.

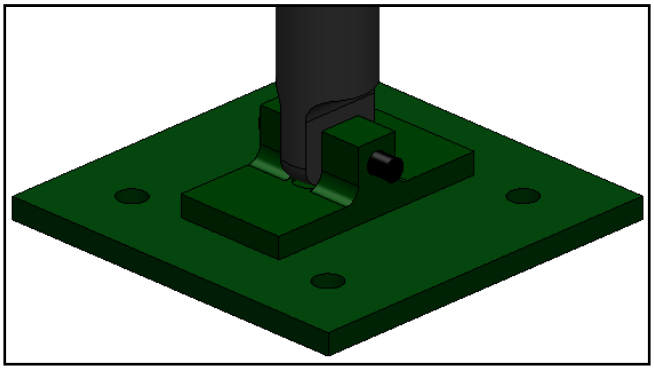

Figure 2.12: Connecting rod floor mount

Figure 2.13 shows a cross-section of the connection between the connecting rods and the static I-beam with a bolt-on clevis mount.

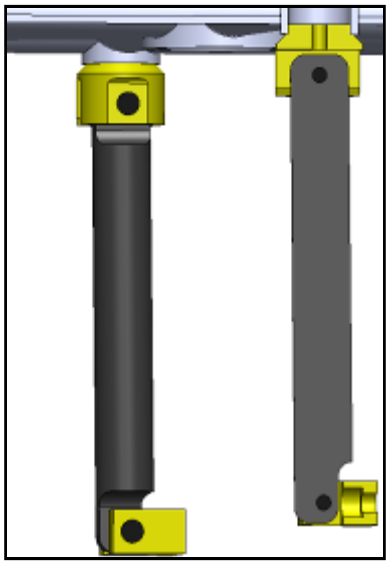

Figure 2.13: Connecting rod static I-beam mount

The location of the floor and static I-beam eyelets is determined by the straightest and shortest routing possible from the bottom of the test rig frame in order increase the stiffness of the connecting rod in this location. The static I-beam clevis mounts bolt directly to the static-I beam using a single bolt and are designed to provide strength and compact mounting while being able to be rotated as to account for small installation differences. FEA for this component is found in Appendix B.

The hole on the top of the welded connecting rod frame mount in Figure 2.13 is present in each frame mount. These holes are threaded and used for the installation of casters such that the tire test rig is easily maneuvered for storage.

2.5. Hub and Indexing

In order to make the frame accessible for testing of components other than tires as well as different sized wheels, the wheel-mounting components which attach to the frame flange are designed to be removable. The challenge in this approach stems from the fact that any play between parts in the assembly will show up in the data giving an inaccurate depiction of tire displacement. Therefore, efforts are made to mitigate the amount of play that exists between parts in the assembly.

Post-machining of the frame assembly squares the mounting plates for the electro-magnetic clamps and frame flange to one another with respect to the centerline of test rig in order to remove any camber or toe which is present after fabrication. In addition to material removal, a bolt-hole pattern is added in order to accommodate a removable plate to which the wheel and tire assembly attaches.

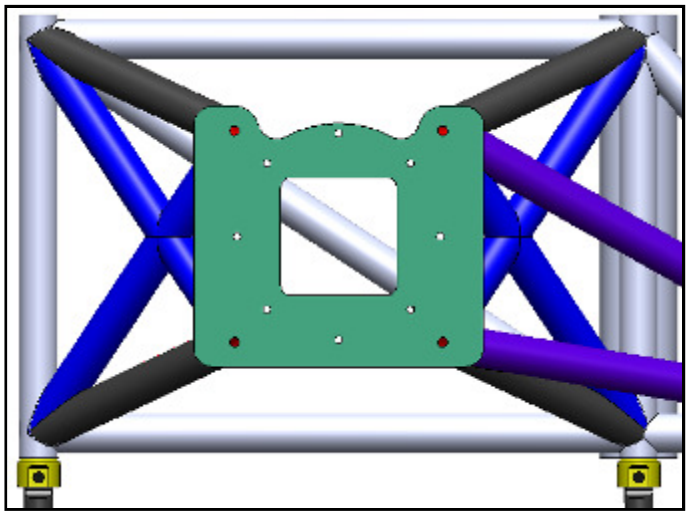

Figure 2.14: Post machined frame flange

The hub snout attachment plate shown in Figure 2.15 provides the connection between the frame flange and the hub snout. The hub snout attachment plate is connected

to the wheel assembly plate using removable dowel pins at the extremities to mitigate play and a circular bolt pattern near the middle in order to reduce plate deflection under load across the span from the hub snout to the dowel pins. The material at the bottom of the plate is removed for tire deflection clearance.

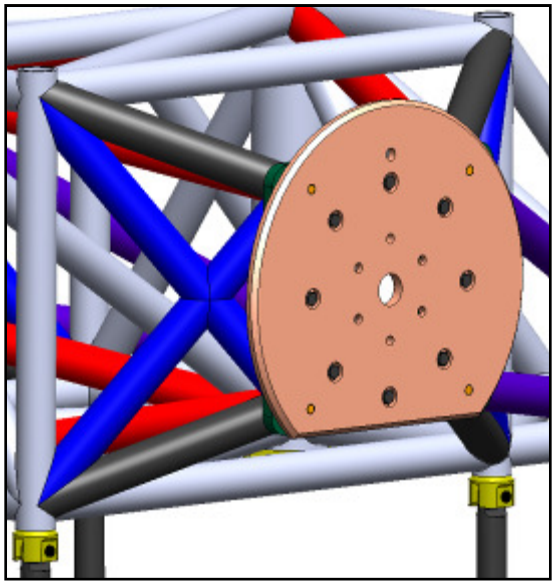

Figure 2.15: Hub snout attachment plate

The hub snout is shown in Figure 2.16 and is affixed similarly with a combination of dowel pins and bolts for the same reasons. FEA for these components is found in Appendix B, and pin sizing calculations are found in Appendix C.

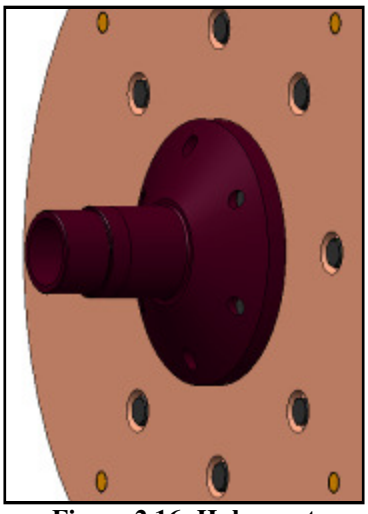

Figure 2.16: Hub snout

The hub snout serves as the base for the rotating components of the wheel and tire assembly. In order to provide this rotation, the hub snout incorporates Timken precision angular contact ball bearings. These ball bearing units are typically used in heavily loaded precision machinery such as lathes and are used in this application due to their radial and axial stiffnesses being an order of magnitude greater than the design goals of the test rig. Angular contact ball bearings exceed the rotation requirements of the tire test rig but are used to serve as a near rigid connection between hub and the hub snout such that they contribute a negligible amount of deflection.

The hub, which rides on the Timken bearings, provides mounting points for the wheels studs as well as bolt circle on the outer extremity of the hub which is used to secure the hub's rotational position during testing. While the wheel stud dimensional layout is dictated by the race car standard, the largest radius possible on the bolt circle is necessary to react moments that are generated at the test loads. A solid hub design is used in order to reduce assembly complexity and endure critical dimensional relationships

between the concentricity of the bearing mounting, wheel studs, and hub-securing bolt circle.

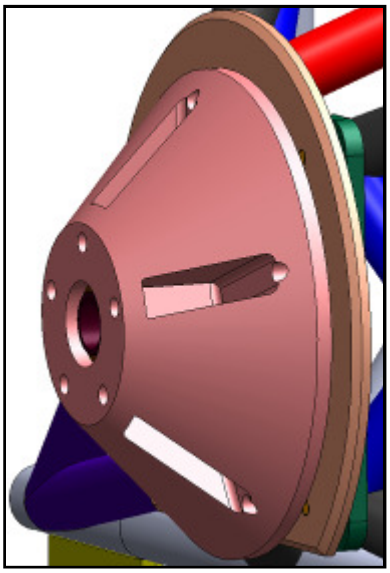

Figure 2.17: Hub

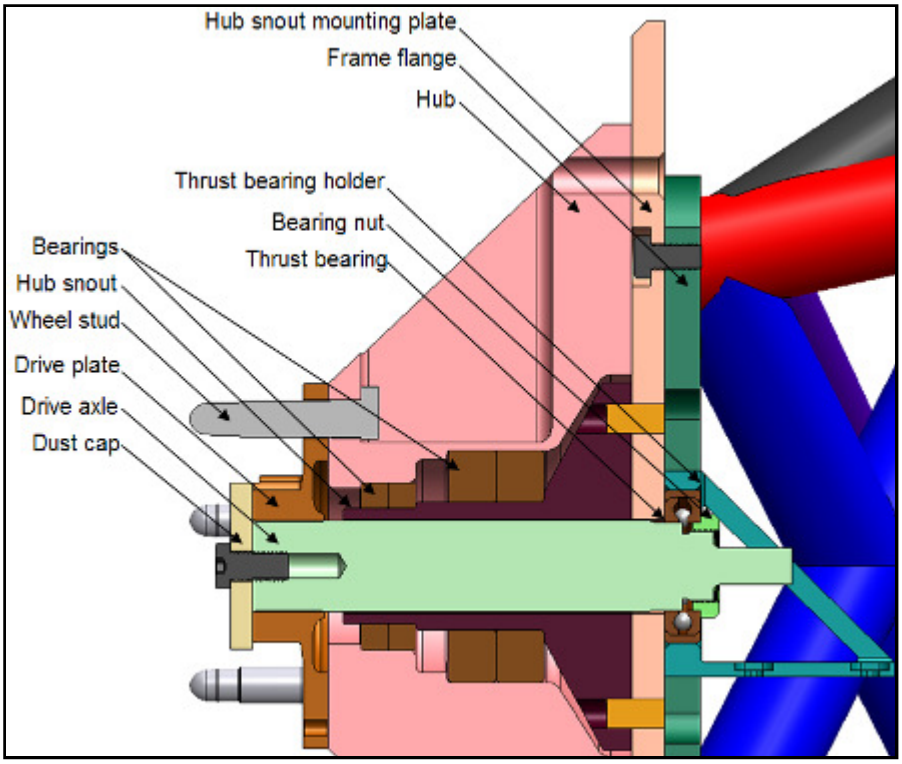

Figure 2.18: Hub assembly cross section

On the face of the hub sits a drive plate. In order to preload the Timken bearings, a drive axle is utilized which connects the splined center of the drive plate with a thrust bearing and bearing nut on the backside of the hub snout mounting plate. This configuration is shown in Figure 2.18. The hole in the frame flange plate exists because the backside of the frame flange cannot be post-machined to be parallel to its front side. Therefore, the concentricity of the drive axle to the thrust bearing cannot be ensured if the thrust bearing mounts to the backside of the frame flange, and as such, it mounts to the backside of the hub snout attachment plate.

Since the test rig design requirements necessitate the need for automation, this hub assembly must be indexed by a motor. Packaging considerations dictate that the indexing motor be mounted vertically. Therefore, the drive axle connects to one end of a 1:1 right angle gearbox while a DC motor and motor head gearbox are attached to the other end. These components are sized to provide enough torque to overcome the stiction in the preloaded bearings as well as spin the assembly slow enough to accurately index the wheel and tire assembly to a desired position. This assembly is shown in Figure 2.19 and design information regarding this gear train is provided in Appendix D.

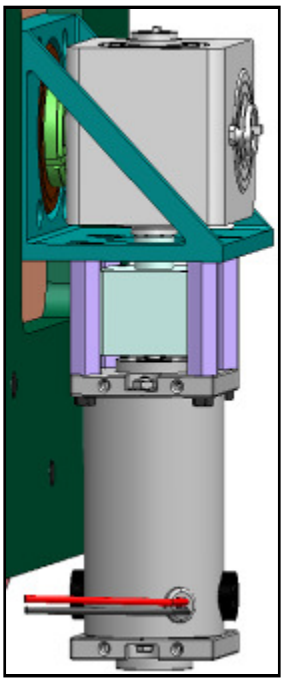

Figure 2.19: Hub indexing assembly

With the hub able to be indexed, a method of securing it during testing which is non-permanent yet does not allow for play within the system must be developed. While other avenues of securing the hub during testing, such as shaft brakes and machining chucks were investigated, this task is accomplished through the use of an expanding diameter pin due to cost, simplicity, and packaging considerations. This pin, shown in Figure 2.20, compresses slit metal sleeves onto ramps such that these sleeves expand up to .01in of their nominal diameter. These expanding diameter pins fit well into the design requirements of the test rig since they are reusable and provide enough clearance to allow them to be inserted and removed from the holes in the hub so that the hub can be indexed and then affixed. These expanding diameter pins also display shear strength which is comparable to their solid equivalents. A problem arises in the fact that this process must be automated and the pin is compressed by holding the center shaft stationary while

tightening the nut or counter rotating the shaft with respect to the nut. Therefore, a gearbox unit must be designed in order to accomplish this task.

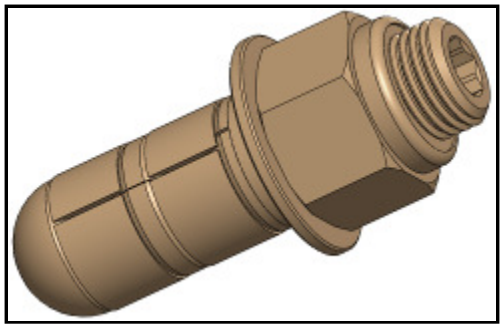

Figure 2.20: Expanding diameter pin

2.6. Gearbox

The function of the gearbox assembly is to automate the repetition of the insertion, tightening, loosening, and removal of the expanding diameter pin. The shaft of the expanding diameter pin must be counter-rotated or held stationary with respect to the rotation of the nut. Since no product is available to accomplish this task with the size requirements that are imposed by the layout of the frame, a gear train is designed which counter-rotates the shaft of the pin with respect to the rotation of the pin nut. Figure 2.21 illustrates the layout of the gear train which is used to rotate the pin nut. The gear sizes are decided through multiple packaging iterations of the gearbox assembly. These iterations are aimed at making the gearbox overall sizing as compact as possibly while using mostly commercially available parts.

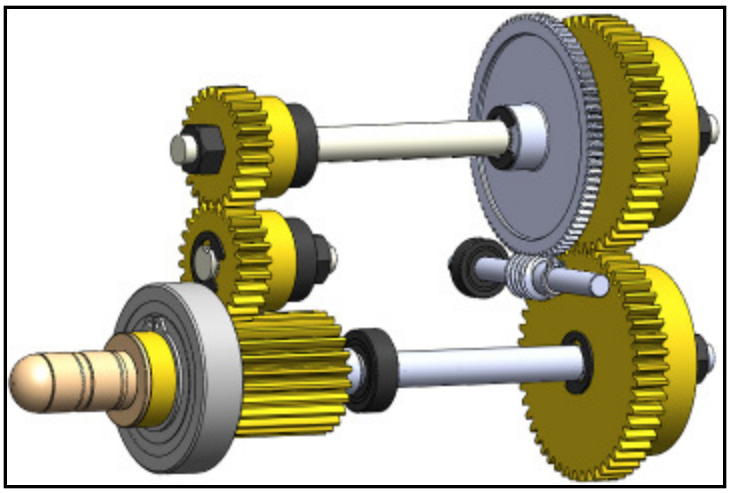

Figure 2.21: Gearbox gear train layout

An unequal gear train arrangement ensures that the gears concentric with the expanding diameter pin are counter-rotating with respect to one another. Therefore, one gear attaches to the nut of the pin while the other gear drives a shaft which connects to the center hex of the pin. A cross section of this shaft arrangement is shown in Figure 2.22.

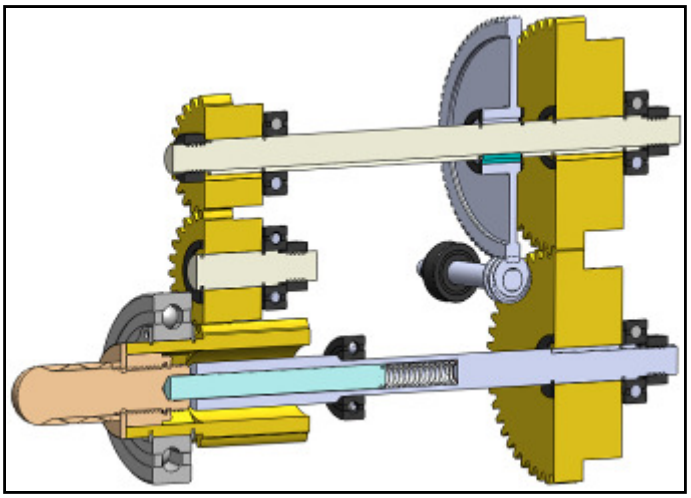

Figure 2.22: Counter-rotating shaft for expanding diameter pin hex

The hollow shaft houses a hex key which is kept in constant contact with the expanding diameter pin hex through a series of springs pushing on one end. The center of

the hollow shaft is cut to the same dimensions hex dimensions as that of the expanding diameter pin shaft head. The shaft in which the hex key resides only rotates and does not translate with the hex key. The useable length of the expanding diameter pin dictates that the pin and, therefore, the hex key and supporting gear must be able to translate an inch in order to insert and remove the useable section of the pin from the corresponding hole in the hub. This actuation is carried out by an air cylinder sized to overcome the force of the springs pushing on the hex key. Monitoring of the state of linear actuation for the control system is performed by two proximity sensors which are adjusted to indicate if the expanding diameter pin is completely inserted in or removed from the hub. This linear actuation assembly is shown in Figure 2.23.

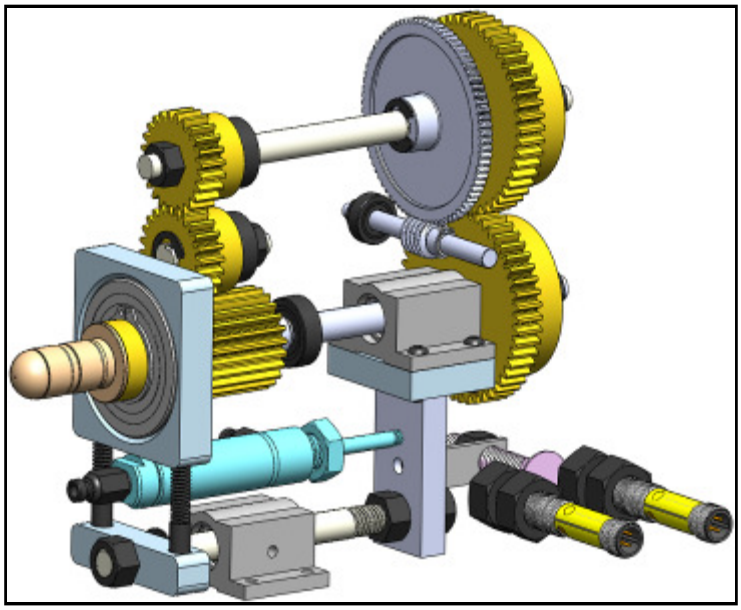

Figure 2.23: Expanding diameter pin linear actuation assembly

Iterations on the layout of the gear train are done in order to compress it into the smallest package possible while still remaining cost effective. A high priority is placed on adjustability of the gearbox in order to avoid the need for high precision machining and allow for easy serviceability. Therefore the entire gear train is housed in an 80/20 Inc.

extruded aluminum frame for ease of mounting and cost effectiveness. Figure 2.24 shows the entire gear train assembly with mounting plates in place while Figure 2.25 illustrates the gear train housed inside the extruded aluminum frame.

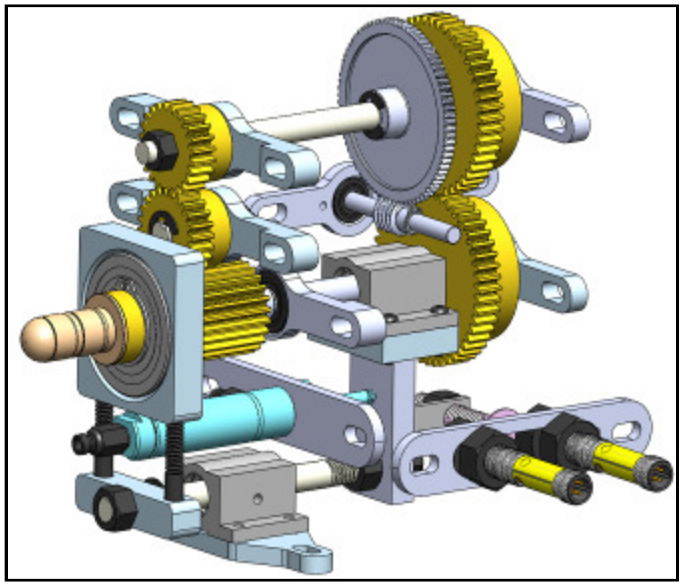

Figure 2.24: Gear train with mounting plates

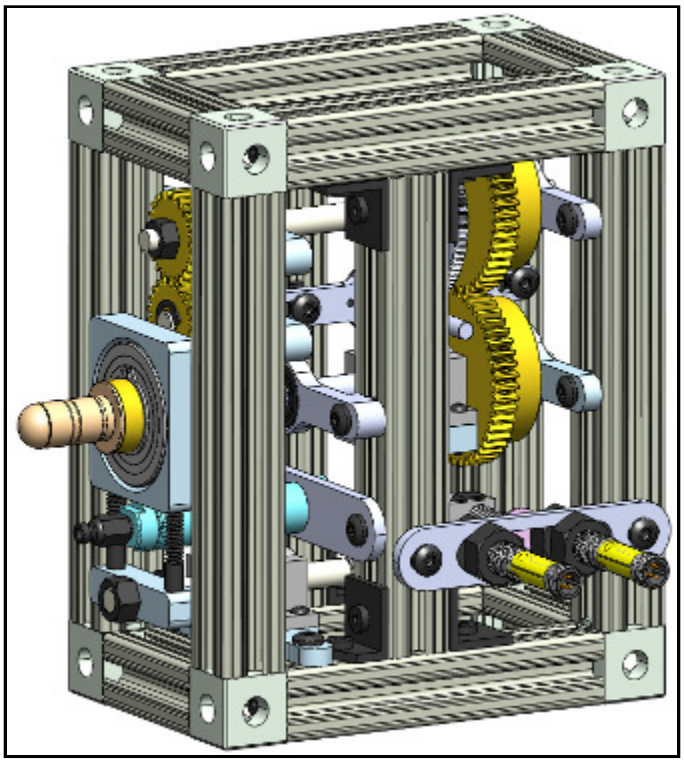

Figure 2.25: Gear train housed inside frame

Recommended tightening torque for the Carr Lane expanding diameter pin is 83ft-lbf (9). In order to accomplish this required torque with packaging space in mind, a DC motor and worm drive arrangement is implemented with the DC motor sitting on the outside of the gearbox frame. Calculations for the selection of the DC motor in conjunction with the existing gear train are found in Appendix E while Figure 2.26 illustrates how this assembly is packaged onto the gearbox frame.

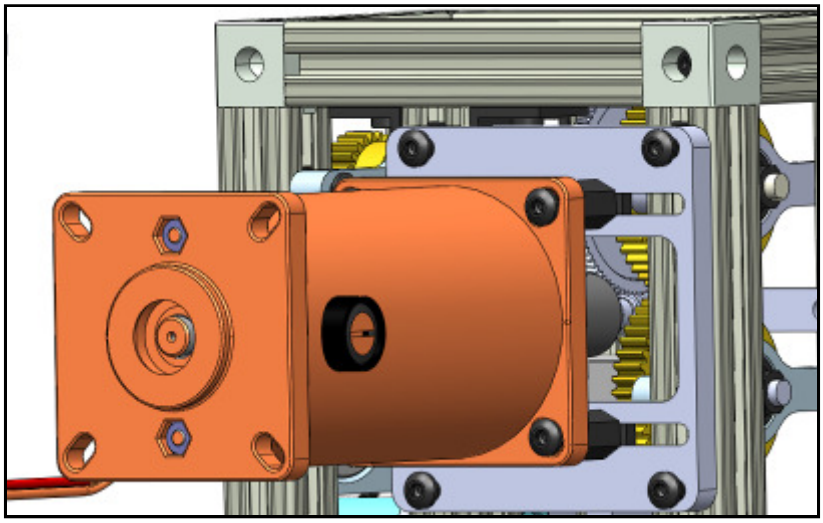

Figure 2.26: DC motor drive for tightening of the expanding diameter pin

The gearbox assembly is attached to the test rig frame through a combination of solid mounts and turnbuckles. The turnbuckles connect the mounts on the gearbox frame to tabs that are welded onto the test rig frame. The solid mounts connect the front of the gearbox to the backside of the hub snout mounting plate. These mounts are shown in Figure 2.27. The solid mounts allow for accurate positioning of the expanding diameter pin with respect to its hole in the hub mounting plate. The turnbuckles ensure that the axis of travel of the pin is collinear with the hole in which it is being extended.

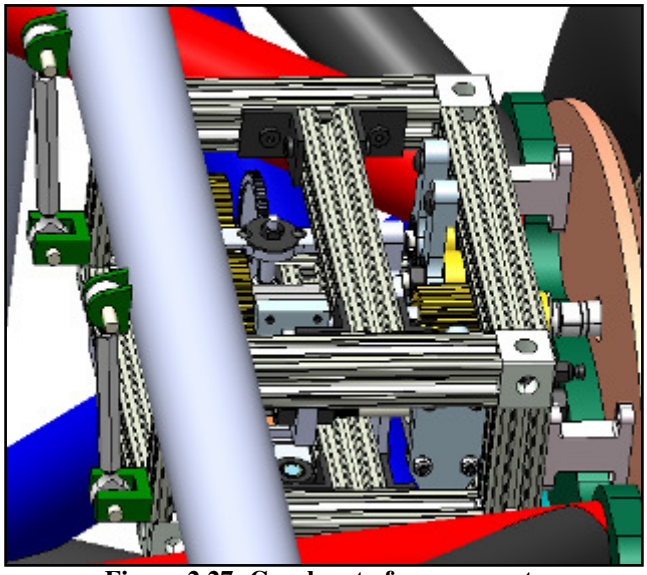

Figure 2.27: Gearbox to frame mounts

Frame and gearbox design are interconnected in the manner that the gearbox must be able to be removed from the frame while fully assembled. This consideration is taken into account in the overall sizing of the gearbox and the layout of the frame structure. The crosshatched areas in Figure 2.28 provide the largest removal space on the test rig frame, and the gearbox is sized to be able to be lifted and rotated through those gaps. The entire layout of the test rig frame is shown in Figure 2.29.

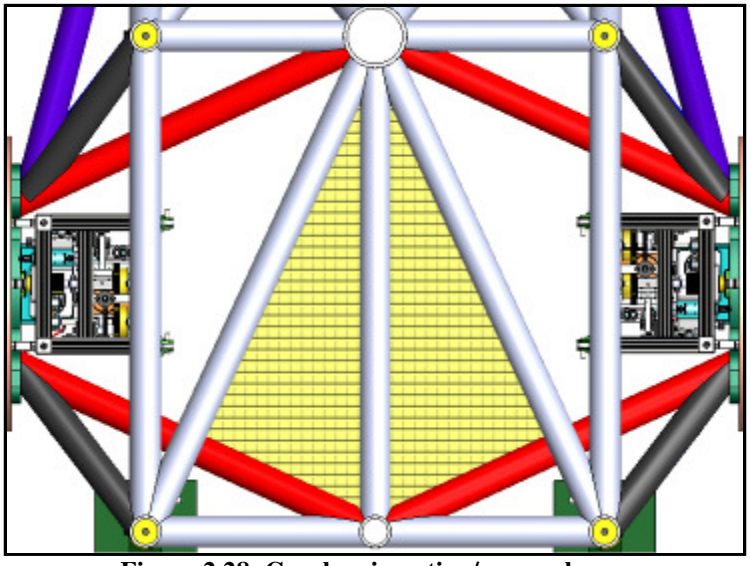

Figure 2.28: Gearbox insertion/removal area

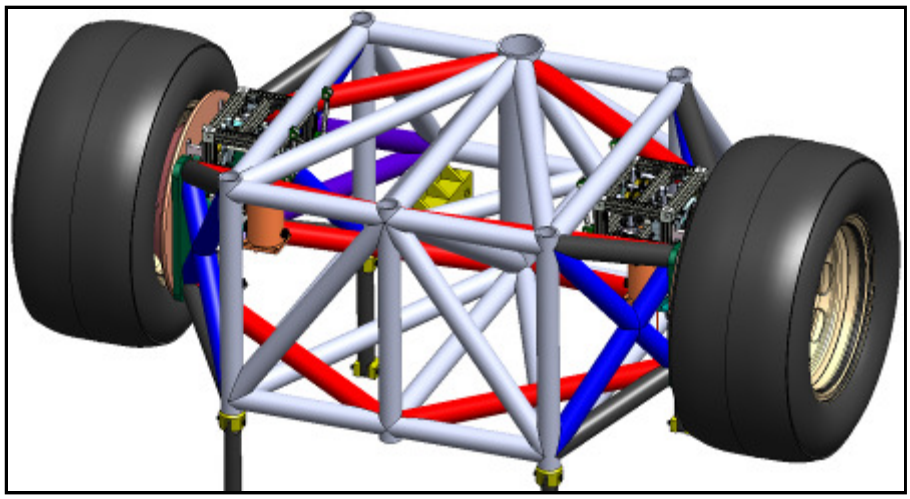

Figure 2.29: Complete tire test rig

Pressure in the tires is controlled through an electronic pressure value that is mounted external to the test rig. The electromagnetic clamps also house a pressure manifold on their base, so, though a combination of connectors, tubing, and the pressure regulating valve, the internal pressure of the tire is controlled. A list of these components as well as all components that are a part of this test rig assembly is found in Appendix A.

2.7. Stiffness

The design of the frame for the tire test rig is driven largely by packaging considerations with respect to fitting the gearbox within the frame, reducing cantilevered component lengths, and allowing suitable clearance for the travel of the elevators of the K&C rig during lateral, longitudinal, and vertical motion. With respect to installation stiffness of the test rig, the most important design areas are those which are cantilevered. The major cantilevered areas of the test rig are the length of hub snout, and the offset of the frame flange plate from the base frame structure. The packaging of the entire assembly is adjusted in order to minimize the cantilevering of these areas.

The area which has the most negative impact on overall frame stiffness is the hub snout due to its distance from the connecting rod mounts and the fact that it is purely cantilevered from its mounting plate. Therefore, the hub snout is shortened as much as possible while still allowing the tire to maintain suitable clearance to the hub snout mounting plate. This gap is set conservatively at a half inch laterally to the sidewall near the bead. This displacement should never be realized even at low inflation, high lateral load test conditions. This gap length allows the length of the snout to be set.

The next most important design area is the offset of the frame flange plate from the edge of the base frame structure which is driven by the length of the support tubes. This offset is tied to the requirement to have the track width of the rig be at 60 inches. The plate is made as thin as possible to accept the countersunk bolts and handle the stresses that are imparted during loading while the support tubes are made as long as necessary to achieve the track width. The angles of the support tubing are driven by the need to have clearance for the gearbox to sit between the tubes at a distance close enough to the hub snout mounting plate such that the expanding diameter pin can be inserted and removed from the hub.

With the packaging of these critical areas addressed, the next step is to determine whether the test rig's compliance. Even though compliance error can be accounted for since the K&C machine measures wheel center as well as elevator pad motion, a stiff test rig is still important. Stiffness is necessary in order to reduce frame fatigue, mitigate any induced camber or toe during testing, and allow for possible repurposing of the test rig for use on another measurement machine where wheel center motion is not tracked and any compliance would result in measurement error

The design goal for the stiffness revolves around making the test rig stiff enough that any measurement error of tire deflection which is incurred by the deflection of the test rig frame does not induce an error more than the tire to tire variation found in race tires. This tire to tire variation is found to be around 5% (7). By modeling the tire and test rig as two springs in series and then comparing the measured stiffness against the actual tire stiffness in each test axis, Figure 2.30 and Table 2.2 are generated. The tire stiffnesses which are used for each test axis are the maximum encountered in standard racing conditions (8).

Test rig stiffness with respect to camber and toe stiffness is also of design interest. The project sponsor's race cars have an induced camber and toe stiffness of approximately 2000lbf/deg and 1250lbf/deg, respectively (10). Therefore, another design objective is to have the frame stiffness be an order of magnitude greater than these values.

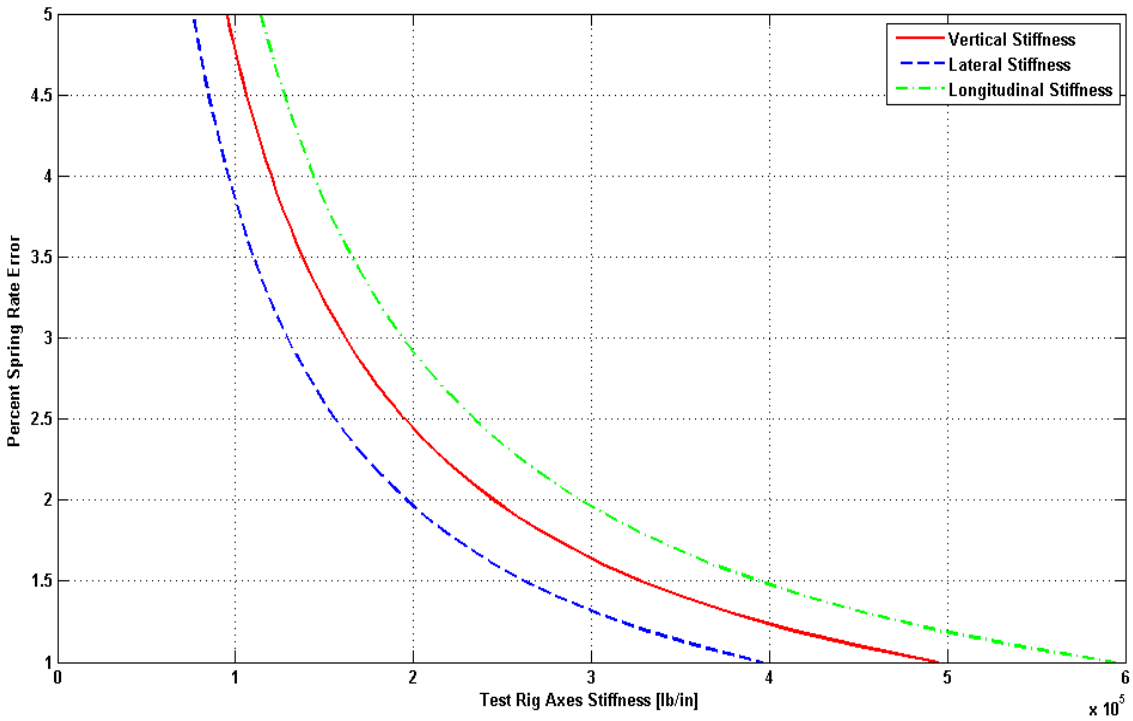

Figure 2.30: Test rig design stiffness goals

Table 2.2: Test Rig Design Stiffness Goals

Test Axes	Stiffness [lb/in]	Allowable Test Rig Stiffness
Tire -Vertical	5000	≥95000 lb/in
Tire - Lateral	4000	≥76000 lb/in
Tire - Longitudinal	6000	≥114000 lb/in
Camber	2000	≥20000 lb/deg
Toe	1250	≥12500 lb/deg

In order to assess the installation stiffness of the test rig, Solidworks Simulation FEA is employed. The model which is analyzed is shown in Figure 2.31 and is a nearly complete test rig assembly with the removal non-structural parts such as the gearbox. A complete description of the setup for the FEA including assumptions, component materials, and constraints is found in Appendix F.

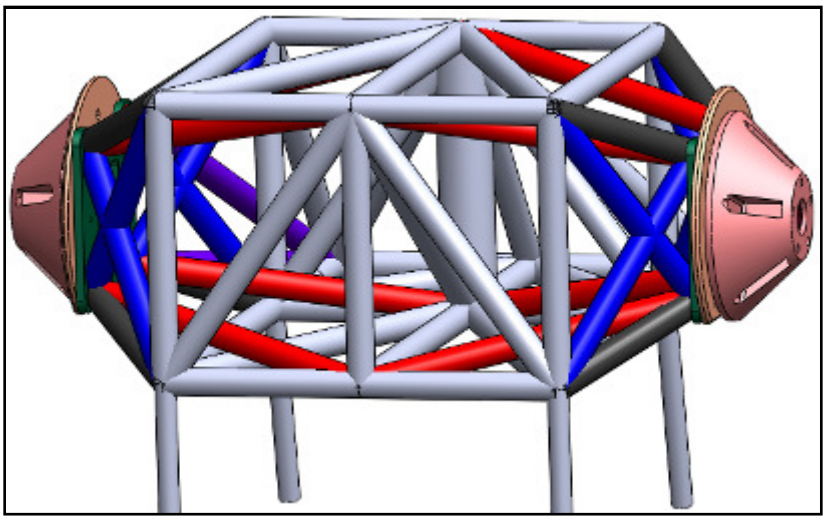

Figure 2.31: FEA assembly

The stiffness of the test rig is evaluated in two planes, the backside of the frame flange and interfacing surface between the hub and the wheel center, with four points on each plane to account for camber and toe. These two locations are evaluated in order to see the difference between the compliance allowed by the frame and that allowed by the frame plus the wheel and tire assembly mounting components. Loads are applied in the wheel center plane at a distance representative of a nominal race tire. Table 2.3 gives the applied loads while the results of the FEA on the frame are displayed in Table 2.4 and Table 2.5 using the SAE coordinate system shown in Figure 5.2.

Table 2.3: FEA Applied Loads

Axes	Force [lbf]
Vertical (Z)	-6000
Lateral (Y)	±4000
Longitudinal (X)	±5000

Table 2.4: FEA Stiffness Results @ Hub

	Vertical Loading	Lateral Loading	Longitudinal Loading
Vertical Stiffness [lb/in]	310398	204603	3513703
Lateral Stiffness [lb/in]	683838	147765	332667
Longitudinal Stiffness [lb/in]	1708428	560695	238663
Camber Stiffness [lb/deg]	55045	21052	454545
Toe Stiffness [lb/deg]	1000000	142857	39682

Table 2.5: FEA Stiffness Results @ Frame

	Vertical Loading	Lateral Loading	Longitudinal Loading
Vertical Stiffness [lb/in]	688626	1335113	1928268
Lateral Stiffness [lb/in]	1305199	251889	394944
Longitudinal Stiffness [lb/in]	1545595	840336	716845
Camber Stiffness [lb/deg]	169787	96677	1332979
Toe Stiffness [lb/deg]	1481052	154397	95341

The stiffness values of the at the frame are larger than those at the hub face, and the stiffness values at the hub exceed the design objectives set for the project as found in Table 2.2. Therefore the main test rig frame assembly design is suitable for the project as shown by Figure 2.32.

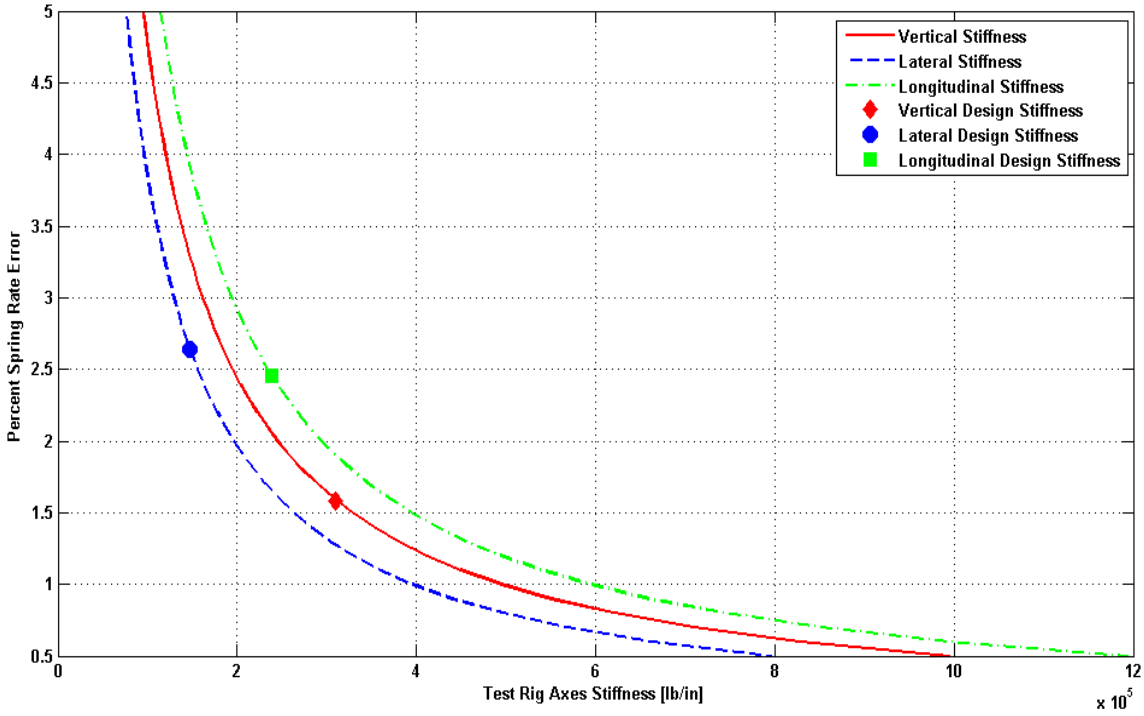

Figure 2.32: Test rig design stiffness

Note that the percent errors shown in Figure 2.32 are calculated using the stiffest axial spring rate which is known for the project sponsor's race tires. Therefore, these values set the upper bound on percent error in design.

3. Validation

With the test rig designed and constructed, the next step is to validate the design through initial testing. The goal of this initial testing is to identify any problem areas in the design or construction and then resolve these problems through redesign or component replacement. A picture of the installed test rig is given by Figure 3.1.

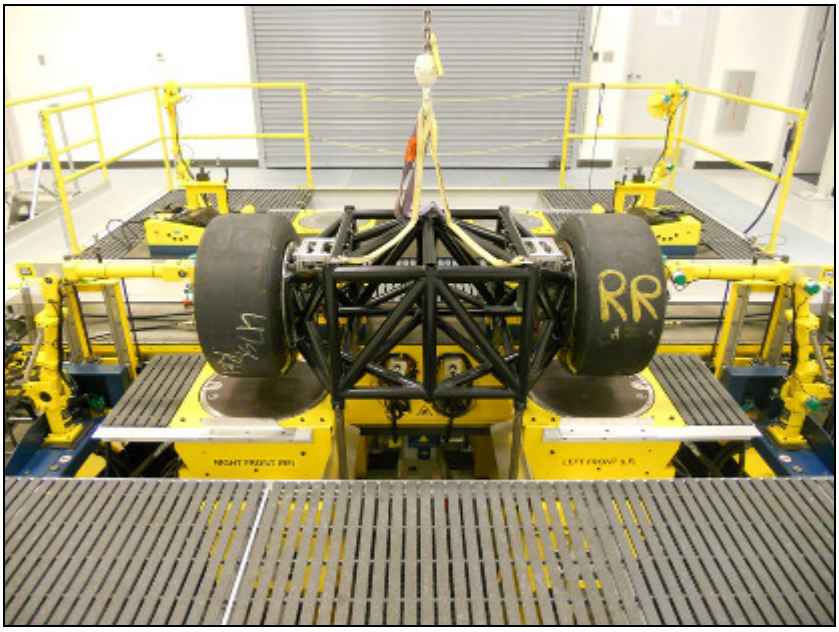

Figure 3.1: Fully constructed and installed test rig

Initial testing of the rig utilizes the rigid mounts which are used by some teams during testing in order to remove the compliance of the tire from the suspension system. This initial testing is confined to vertical-only in order to determine the state of the installed test rig. Figure 3.2 shows the testing configuration while the results of initial testing are given by Table 3.1.

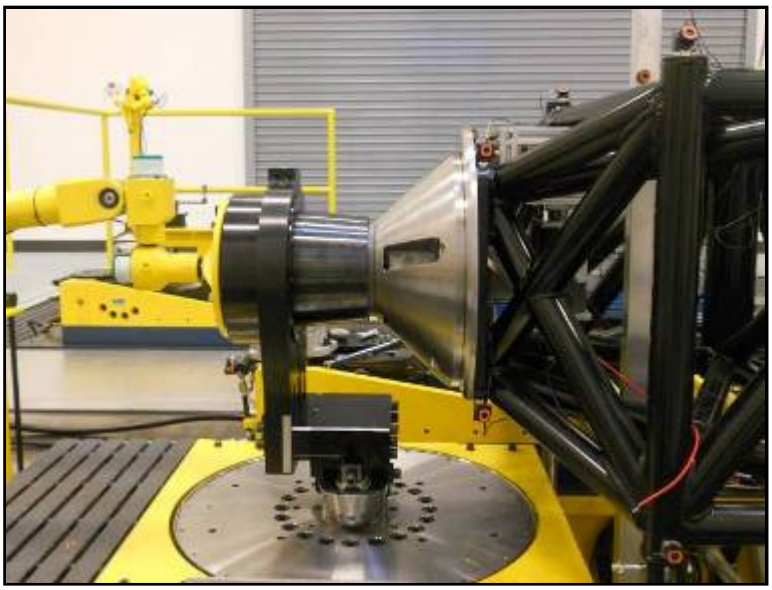

Figure 3.2: Initial testing configuration

Table 3.1: Initial Rig Development Results

Axes	FEA Predicted @ Hub	Measured @ Hub
Vertical Stiffness [lb/in]	310398	58339
Camber Stiffness [lb/deg]	55045	10984

As the results in Table 3.1 show, the installation stiffness of the test rig is much less than that predicted by the FEA. In order to fully understand the movement of the entire test rig frame under loading conditions and not just the hub areas, a Metris K600 dynamic measurement system is employed. This system is capable of tracking the motion of a series of LED sensors which are capable of being mounted anywhere on the test rig which offers a line-of-sight back to the measurement head. An overall picture of this setup is shown in Figure 3.3.

Figure 3.3: Metris LED Measurement System

The following list summarizes the results of this validation study:

- The hub snout bearings are found to have been installed in the incorrect orientation.
- The turnbuckle rod ends and pins are found to exhibit excessive deflection under load and are redesigned to solid rod ends with solid clevis pins.
- The electro-magnetic clamps are found to provide insufficient clamping load to counter the applied loads and are redesigned.

Table 3.2 lays out the results from the design changes made as the result of the rig stiffness validation study.

Table 3.2: Final Rig Development Results

Axes	FEA Predicted @ Hub	Initial Measured @ Hub	Final Measured @ Hub
Vertical Stiffness [lb/in]	310398	58339	139616
Camber Stiffness [lb/deg]	55045	10984	47047

The majority of the excessive rig deflection is the result of the bearings being incorrectly oriented upon installation. The replacement and redesign of other parts which deflected more than initially predicted contributes to the large increase in camber and vertical stiffness. Although still not as stiff as the FEA predicts, the test rig is considered ready for production testing since the final measured stiffness induces a potential measurement error of less than 5% vertically. Small variations in rig displacement lead to large differences in rig stiffness at the displacement magnitude of the test rig. The stiffness of the test rig can be increased through minor changes, but these changes are deemed unnecessary to begin testing considering that the induced error is accounted for and no non-K&C rig tests are planned at time of the writing of this paper. Lateral and longitudinal validation tests are conducted during actual testing of tires.

4. Testing

4.1. Test Conditions

With the test rig validation testing complete, production testing is started. Production testing consists of subjecting a tire to conditions which are determined by planned implementation of the static tire model. The vertical test ranges are set to encompass the possible conditions a tire sees during vehicle suspension setup for each track type encountered during a race season (11). On the other hand, the lateral and longitudinal test more closely mimic the conditions a tire might experience during actual use on a vehicle on these tracks. These lateral and longitudinal conditions are tested in order to develop a model for use on non-rolling test rigs such as a shaker or K&C whereas the vertical tests are focused initially on vehicle setup simulations. All tests are conducted at .2Hz using a sine wave loading profile in order to mimic the rolling tire spring rate testing procedure for which data is already provided.

4.2. Pad Surface

Two elevator pad surfaces are available when testing on the K&C. These two surfaces, shown in Figure 4.1, are spiked or coarse sandpaper.

Figure 4.1: Possible test pad surfaces

While the spiked surface offers the opportunity for more lateral and longitudinal force before slipping than the coarse sandpaper, the spiked plate is not used because the penetration of the spikes into the contact patch are suspected to distort the realistic motion of the tire carcass during loading. Therefore, the coarse sandpaper plates are used for all testing and as such, the maximum G-level that is possible during lateral and longitudinal testing is .8G.

4.3. Indexing

Before a tire undergoes any testing on the rig, it is run through an indexing test sweep in order to determine the test position which is least likely to be at or near a splice in the tire belt. Index testing is done with vertical displacement only and is performed at zero inclination angle, the highest outer liner pressure, and over the corresponding range of vertical force which is associated with the type of tire being tested. The resulting data is condensed to a scatter plot of the measured spring rate at each test index. An example this testing index plot is given by Figure 4.2.

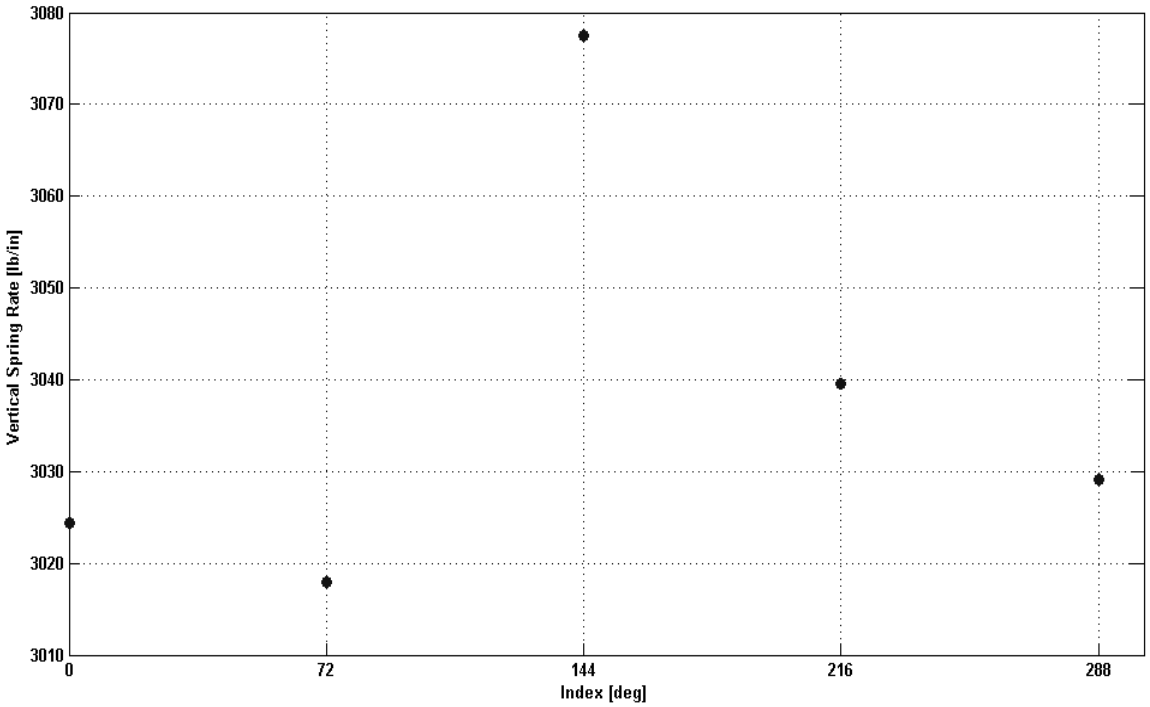

Figure 4.2: Index testing resultant plot example

The identification of splice is done with the knowledge that a splice typically shows a deviation of more than 5% from the mean vertical spring rate (7), and as Figure 4.3 shows, the test repeatability of a tire is ±.5% as collected from successive vertical tests of the same tire on the test rig with the pressure adjusted after each test. Therefore, the data in Figure 4.2 shows an outlier in the data at the 144deg index position, so the indexes nearest to 180deg from the potential splice, 0 and 288deg in this case, are considered for testing. Only one of these indexes is chosen for testing, though, and this choice is subjective and non-critical once the potential splice location is identified.

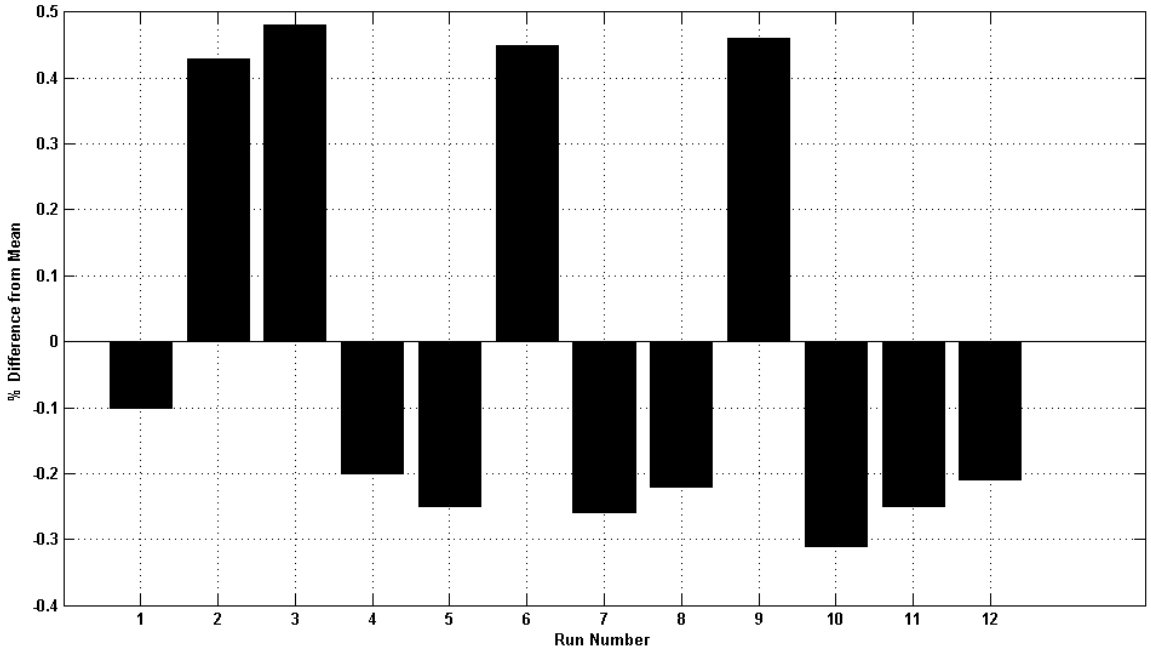

Figure 4.3: Spring rate repeatability

4.4. Elevator control

Control of the elevators on the K&C machine is possible through a force or position feedback loop. In the case of all testing presented in this document, force control is utilized. Force control is used because it is the most direct method of achieving the desired test loads. During vertical, lateral, or longitudinal tests, the implementation of force control causes a small shift in vertical position after every run due to the drift of peak amplitude which is commonly associated with forced vibration. Due to the small number of test cycles, five, this position drift is small and is averaged out of the data which is used for fitting. Table 4.1 gives the breakdown of how the elevator pad is controlled for each test type.

Table 4.1: Pad Control During Testing

	Pad Control Type		
Test Axis	**Vertical**	**Lateral**	**Longitudinal**
Vertical	Position	Floating	Floating
Lateral	Force	Force	Floating
Longitudinal	Force	Floating	Force

4.5. Data Processing

Data processing of the test data for fitting is done through a GUI written in MATLAB. The purpose of the GUI is to streamline data visualization, processing, analysis, and fitting into one tool which handles any combination of possible tire test rig acquired data. The layout and functionality of the GUI is covered in Appendix G. An example of raw data collected from the test rig is shown in Figure 4.4.

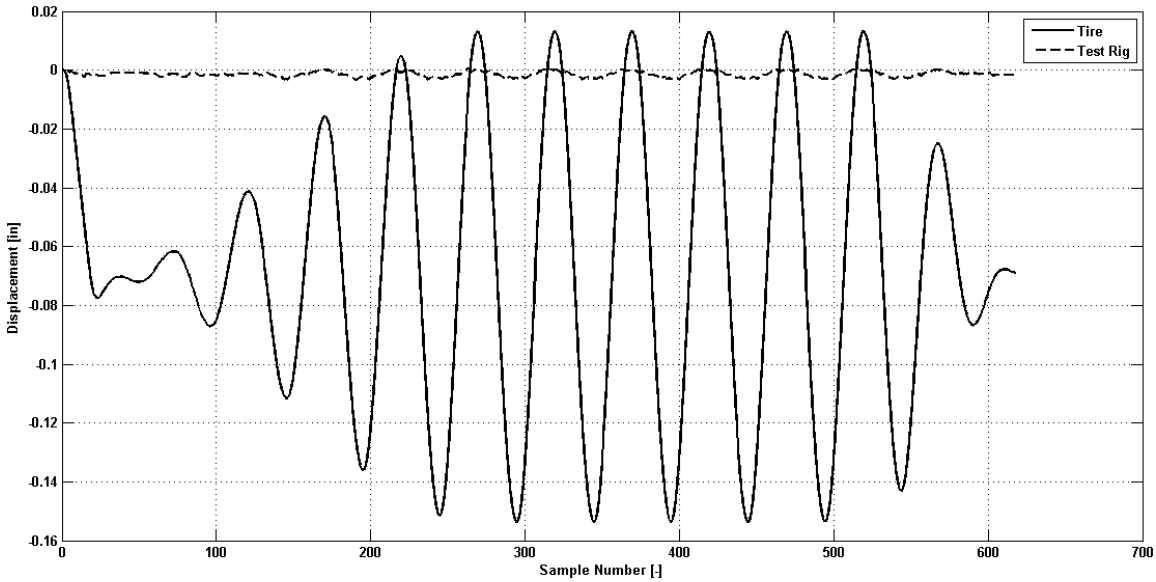

Figure 4.4: Raw tire displacement data

First, the raw test data is processed by subtracting the displacement that is measured at the hub from that which is measured at the contact patch of the tire in the direction of testing in order to resolve the displacement of only the tire. Once this displacement correction is made, the ends of the data are removed from the dataset since these do not represent actual test data, only the warm up and cool down cycles of the test rig. These skewed data areas are evident and the beginning and end of the raw data in Figure 4.4.

These skewed data areas are removed by processing only the middle 90% of the test data and considering peaks of data which fall within ±5% of the mean peak amplitude of the data. Once the data range of interest are found, the data is divided into individual loading and unloading cycles within that range and then averaged to create one data set. This data set is shifted such that first data point is at zero, and the last data point is set equal to the first. The result of these operations is shown in Figure 4.5.

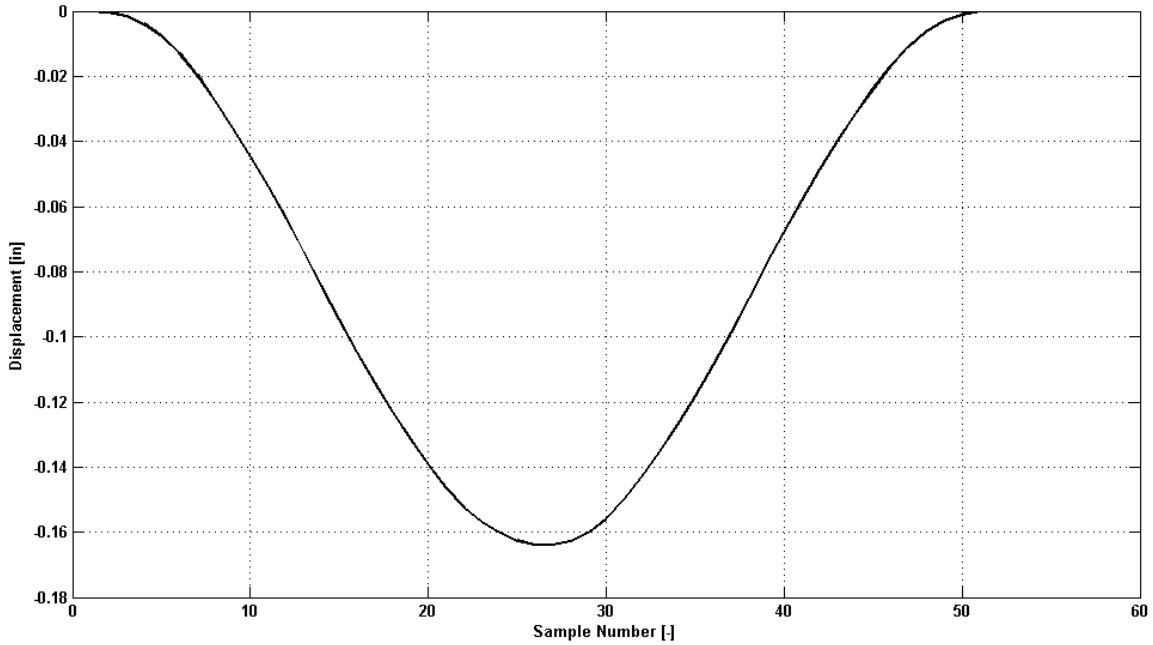

Figure 4.5: Averaged test data

This peak division and subsequent averaging of the data is used to process displacement, loaded radius, and overturning moment data. The collapsing of the hysteric loop is done because no current simulation models are setup to take tire damping into account. Also, the K&C test rig is limited presently to a maximum frequency of 5Hz which only covers a quarter of the frequency range of interest for tire damping.

5. Fitting

The purpose of gathering and processing the tire test rig data is to develop simple formulas which accurately model tire parameters over a range of operation conditions. These tire parameters are measured using the tire test rig and implemented in vehicle simulation programs which utilize a static tire model in order to predict how a vehicle behaves on a test rig or during suspension setup with a particular tire. The parameters which are fit are loaded radius, overturning moment, and tire displacement in the axes of testing. The prediction accuracy of these parameters is set by a consortium of tire engineers from the race teams.

In order to keep the equations simple, a polynomial data fitting approach is chosen for all parameters because the test range is small, the test data exhibits simple trends, and extrapolation is not a concern. The goal of this approach is to keep the order small while establishing a fit which is accurate enough to meet the needs of the teams.

5.1. Fit Parameters

The loaded radius of a tire is a measurement of the distance from the center of the vehicle hub to the ground. In order to maintain consistency with how loaded radius is calculated in rolling tire test data, the distance measurement is taken along the centerline of the tire as shown in Figure 5.1. The maximum error band set for loaded radius is .06in. Loaded radius is utilized in simulation models to predict normal force on the tire.

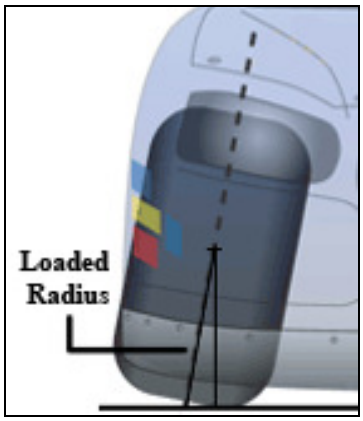

Figure 5.1: Loaded radius measured along tire centerline

The overturning moment of a tire is the torque which is generated about the direction of wheel heading along the centerline of the tire as shown in the SAE coordinate system in Figure 5.2. For vehicle reference, the direction of wheel heading points forward on the vehicle and if looking at a vehicle from the rear, the positive direction of lateral force points from left to right.

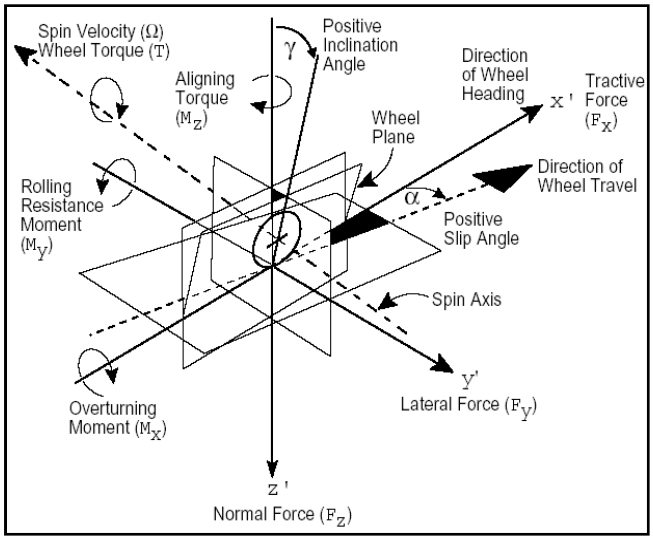

Figure 5.2: SAE coordinate system with overturning moment and displacement axes

The test axes displacements use the SAE coordinate system as well and are measured along the lateral, normal, and tractive force axes. The overturning moment maximum error is 3.5ft-lbf while the displacement error is set at .06in. Overturning

moment is utilized in vehicle simulation models for kinematics and compliance calculations as well vehicle dynamics. The displacement parameter is included in order to evaluate tire stiffness under vehicle operating conditions.

Table 5.1 provides the layout of fit parameters with respect to test variables of which their fits are a function.

Table 5.1: Fit Parameters

Fit Parameters	Test Axes	Fit Function Parameters				
		Vertical Load	Lateral Load	Longitudinal Load	Inclination Angle	Outer Liner Pressure
Loaded Radius	Vertical	✓	-	-	✓	✓
	Lateral	✓	✓		✓	✓
	Longitudinal	✓	-	✓	✓	✓
Overturning Moment	Vertical	✓	-	-	✓	✓
	Lateral	✓	✓	-	✓	✓
	Longitudinal	✓	-	✓	✓	✓
Test Axis Displacement	Lateral	✓	✓	-	✓	✓
	Longitudinal	✓	-	✓	✓	✓

Test axis displacement is not fit for vertical testing since it is possible to derive that measurement from the loaded radius. Not evident in Table 5.1 is that with respect to outer liner pressure, equations are generated which fit the test data across all or at each individually tested pressure. These fits across all tested pressures are referred to as a pressure dependent fit while the individual pressure fits are referred to as pressure independent. In order to facilitate the implementation of pressure independent and dependent fits into simulation packages, the equations are setup to have outer liner pressure be the last fit function parameter which is fit and therefore is easily dropped from the equation.

5.2. Equations

Equation simplicity is also carried over to the number of equations which are implemented to fit the test parameters. The goal is to establish one polynomial equation which fits the necessary parameters within the specified error bounds in order to reduce the debugging time and chance for error inherent with multiple equations being implemented into multiple computer models.

5.2.1. Vertical

Equations 5.1 and 5.2 give the vertical pressure dependent and independent formulations, respectively. The output of these equations can either be loaded radius or overturning moment depending on which coefficients, κ, are used. The 'FZ' term is normal load, the 'IA' term is inclination angle, and the 'P' term is outer liner pressure.

$$Pressure\ Dependent\ Output = A * FZ^2 + B * FZ + C \quad \textbf{(5.1)}$$

$$A = A_1 * IA^3 + A_2 * IA^2 + A_3 * IA + A_4$$
$$A_1 = \kappa_0 * P^3 + \kappa_1 * P^2 + \kappa_2 * P + \kappa_3$$
$$A_2 = \kappa_4 * P^3 + \kappa_5 * P^2 + \kappa_6 * P + \kappa_7$$
$$A_3 = \kappa_8 * P^3 + \kappa_9 * P^2 + \kappa_{10} * P + \kappa_{11}$$
$$A_4 = \kappa_{12} * P^3 + \kappa_{13} * P^2 + \kappa_{14} * P + \kappa_{15}$$
$$B = B_1 * IA^3 + B_2 * IA^2 + B_3 * IA + B_4$$
$$B_1 = \kappa_{16} * P^3 + \kappa_{17} * P^2 + \kappa_{18} * P + \kappa_{19}$$
$$B_2 = \kappa_{20} * P^3 + \kappa_{21} * P^2 + \kappa_{22} * P + \kappa_{23}$$
$$B_3 = \kappa_{24} * P^3 + \kappa_{25} * P^2 + \kappa_{26} * P + \kappa_{27}$$
$$B_4 = \kappa_{28} * P^3 + \kappa_{29} * P^2 + \kappa_{30} * P + \kappa_{31}$$
$$C = C_1 * IA^3 + C_2 * IA^2 + C_3 * IA + C_4$$
$$C_1 = \kappa_{32} * P^3 + \kappa_{33} * P^2 + \kappa_{34} * P + \kappa_{35}$$
$$C_2 = \kappa_{36} * P^3 + \kappa_{37} * P^2 + \kappa_{38} * P + \kappa_{39}$$
$$C_3 = \kappa_{40} * P^3 + \kappa_{41} * P^2 + \kappa_{42} * P + \kappa_{43}$$
$$C_4 = \kappa_{44} * P^3 + \kappa_{45} * P^2 + \kappa_{46} * P + \kappa_{47}$$

$$Pressure\ Independent\ Output = A * FZ^2 + B * FZ + C \quad \textbf{(5.2)}$$

$$A = \kappa_0 * IA^3 + \kappa_1 * IA^2 + \kappa_2 * IA + \kappa_3$$

$$B = \kappa_4 * IA^3 + \kappa_5 * IA^2 + \kappa_6 * IA + \kappa_7$$

$$C = \kappa_8 * IA^3 + \kappa_9 * IA^2 + \kappa_{10} * IA + \kappa_{11}$$

5.2.2. Lateral/Longitudinal

Equations 5.3 and 5.4 give the lateral or longitudinal pressure dependent and independent formulations, respectively. The output of these equations can either be loaded radius, test axes displacement, or overturning moment depending on which coefficients, κ, are used. The 'F' term is the test axes load, the 'FZ' term is normal load, the 'IA' term is inclination angle, and the 'P' term is outer liner pressure.

$$Pressure\ Dependent\ Output = A * F^2 + B * F + C \quad \textbf{(5.3)}$$

$$A = A_1 * FZ^2 + A_2 * FZ + A_3$$

$$A_1 = (\kappa_0 * P^2 + \kappa_1 * P + \kappa_2) * IA^2 + (\kappa_3 * P^2 + \kappa_4 * P + \kappa_5) * IA + (\kappa_6 * P^2 + \kappa_7 * P + \kappa_8)$$

$$A_2 = (\kappa_9 * P^2 + \kappa_{10} * P + \kappa_{11}) * IA^2 + (\kappa_{12} * P^2 + \kappa_{13} * P + \kappa_{14}) * IA + (\kappa_{15} * P^2 + \kappa_{16} * P + \kappa_{17})$$

$$A_3 = (\kappa_{18} * P^2 + \kappa_{19} * P + \kappa_{20}) * IA^2 + (\kappa_{21} * P^2 + \kappa_{22} * P + \kappa_{23}) * IA + (\kappa_{24} * P^2 + \kappa_{25} * P + \kappa_{26})$$

$$B = B_1 * FZ^2 + B_2 * FZ + B_3$$

$$B_1 = (\kappa_{27} * P^2 + \kappa_{28} * P + \kappa_{29}) * IA^2 + (\kappa_{30} * P^2 + \kappa_{31} * P + \kappa_{32}) * IA + (\kappa_{33} * P^2 + \kappa_{34} * P + \kappa_{35})$$

$$B_2 = (\kappa_{36} * P^2 + \kappa_{37} * P + \kappa_{38}) * IA^2 + (\kappa_{39} * P^2 + \kappa_{40} * P + \kappa_{41}) * IA + (\kappa_{42} * P^2 + \kappa_{43} * P + \kappa_{44})$$

$$B_3 = (\kappa_{45} * P^2 + \kappa_{46} * P + \kappa_{47}) * IA^2 + (\kappa_{48} * P^2 + \kappa_{49} * P + \kappa_{50}) * IA + (\kappa_{51} * P^2 + \kappa_{52} * P + \kappa_{53})$$

$$C = C_1 * FZ^2 + C_2 * FZ + C_3$$

$$C_1 = (\kappa_{54} * P^2 + \kappa_{55} * P + \kappa_{56}) * IA^2 + (\kappa_{57} * P^2 + \kappa_{58} * P + \kappa_{59}) * IA + (\kappa_{60} * P^2 + \kappa_{61} * P + \kappa_{62})$$

$$C_2 = (\kappa_{63} * P^2 + \kappa_{64} * P + \kappa_{65}) * IA^2 + (\kappa_{66} * P^2 + \kappa_{67} * P + \kappa_{68}) * IA + (\kappa_{69} * P^2 + \kappa_{70} * P + \kappa_{71})$$

$$C_3 = (\kappa_{72} * P^2 + \kappa_{73} * P + \kappa_{74}) * IA^2 + (\kappa_{75} * P^2 + \kappa_{76} * P + \kappa_{77}) * IA + (\kappa_{78} * P^2 + \kappa_{79} * P + \kappa_{80})$$

$$Pressure\ Independent\ Output = A * F^2 + B * F + C \quad (5.4)$$

$$A = A_1 * FZ^2 + A_2 * FZ + A_3$$
$$A_1 = \kappa_0 * IA^2 + \kappa_1 * IA + \kappa_2$$
$$A_2 = \kappa_3 * IA^2 + \kappa_4 * IA + \kappa_5$$
$$A_3 = \kappa_6 * IA^2 + \kappa_7 * IA + \kappa_8$$
$$B = B_1 * FZ^2 + B_2 * FZ + B_3$$
$$B_1 = \kappa_9 * IA^2 + \kappa_{10} * IA + \kappa_{11}$$
$$B_2 = \kappa_{12} * IA^2 + \kappa_{13} * IA + \kappa_{14}$$
$$B_3 = \kappa_{15} * IA^2 + \kappa_{16} * IA + \kappa_{17}$$
$$C = C_1 * FZ^2 + C_2 * FZ + C_3$$
$$C_1 = \kappa_{18} * IA^2 + \kappa_{19} * IA + \kappa_{20}$$
$$C_2 = \kappa_{21} * IA^2 + \kappa_{22} * IA + \kappa_{23}$$
$$C_3 = \kappa_{24} * IA^2 + \kappa_{25} * IA + \kappa_{26}$$

5.3. Process

The test data is fit using the non-linear least-squares curve fit method in MATLAB (12). This method tries to find the coefficients *x* which solve Equation 5.5 (5.5)where *xdata* contains the inputs to the objective equation and *ydata* is the observed test data. This function seeks to minimize the sum of the squares of the error between the calculated *ydata* and actual *ydata*.

$$\min_x \| F(x, xdata) - ydata \|_2^2 = \min_x \sum_i \left(F(x, xdata_i) - ydata_i\right)^2 \quad (5.5)$$

In order to execute this function in MATLAB, coefficient initial guesses must be provided. These coefficients are garnered by fitting the applicable equation one step at a time. The following description uses data from a pressure independent loaded radius fit but the process is applicable to fitting data to Equations 5.1 through 5.4. Figure 5.3 gives the loaded radius with respect to vertical force for a vertical actuation test for a tire at 0deg IA and 30psi outer liner pressure with no inner liner.

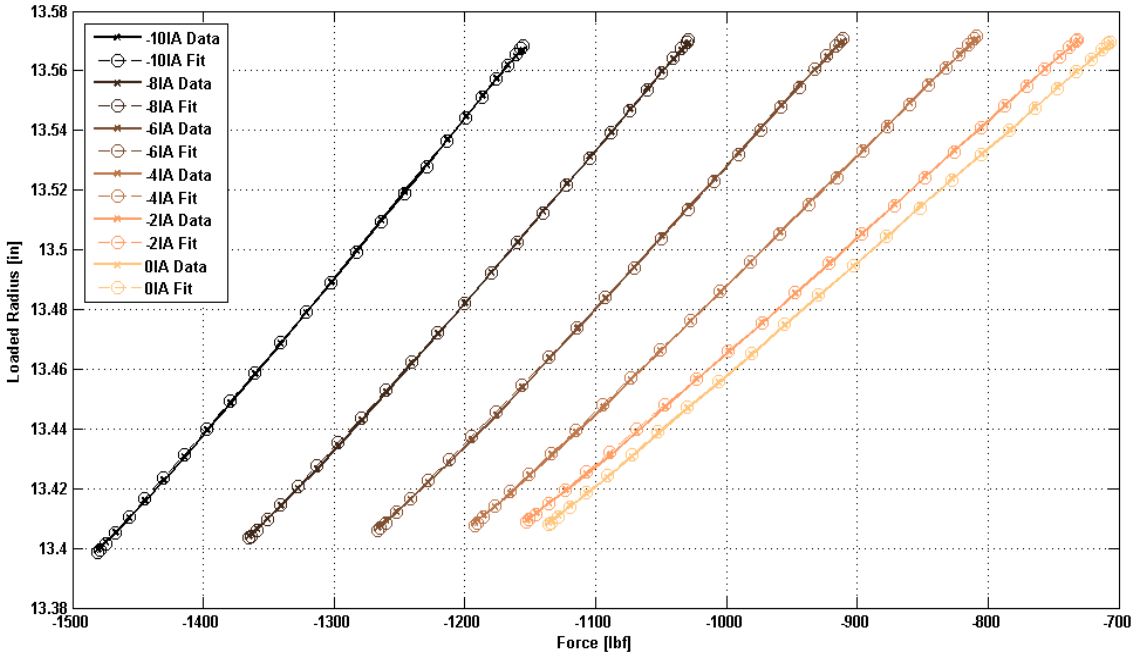

Figure 5.3: Loaded radius versus vertical force

Figure 5.3 also plots the resultant polynomial which is fit to each inclination angle data set using the *polyfit* function in MATLAB. In this case, a second-order fit is used. The resultant coefficients are grouped by order for each pressure and then fit against the next test variable. In this case, the next variable is inclination angle, and this relationship is fit using a third-order polynomial. Figure 5.4 through Figure 5.6 illustrate these grouped-order coefficient fits for each tested pressure.

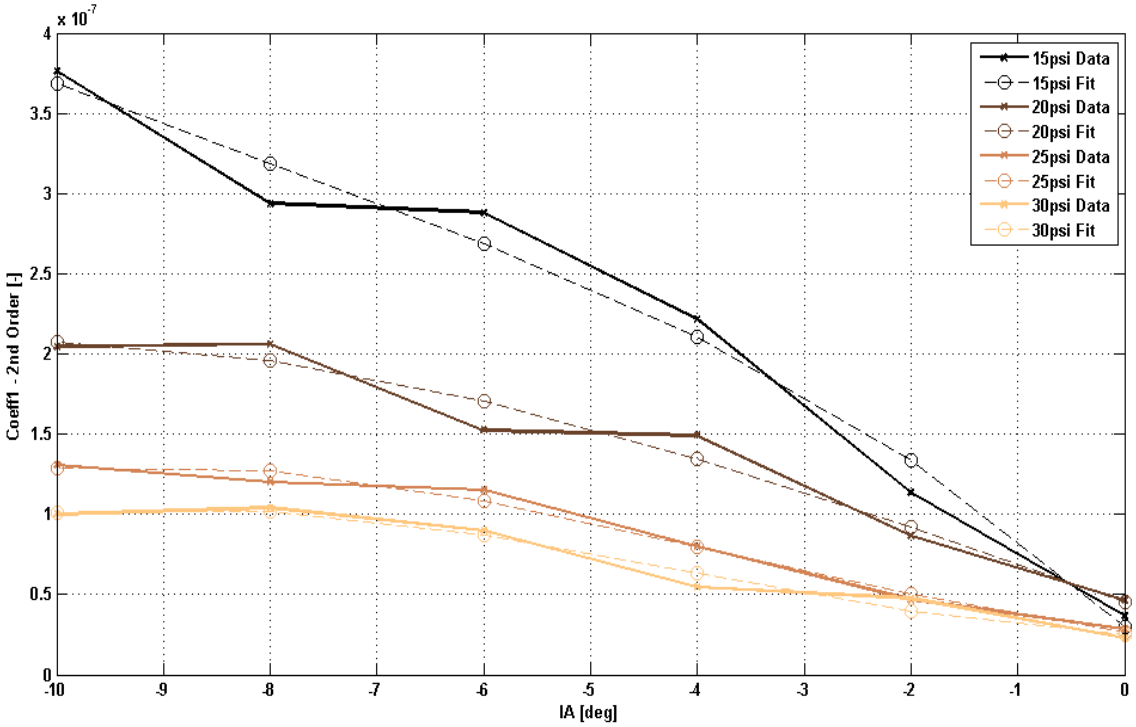

Figure 5.4: 2nd Order coefficients versus inclination angle

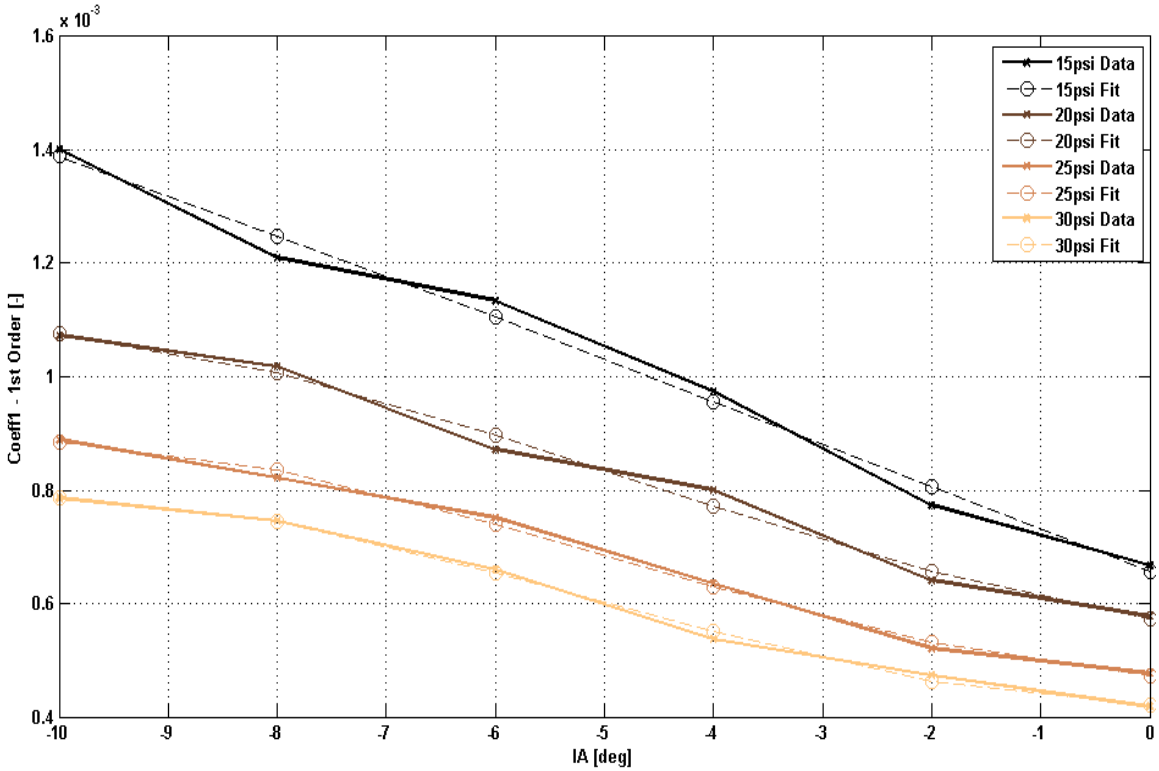

Figure 5.5: 1st Order coefficients versus inclination angle

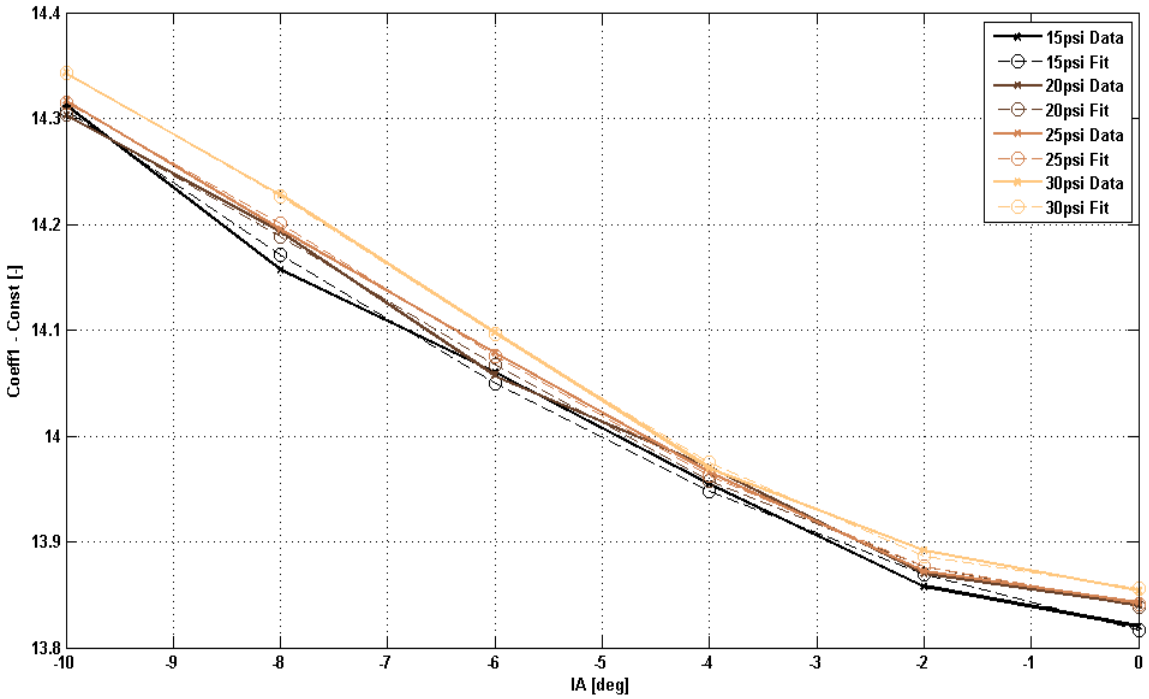

Figure 5.6: Constant coefficients versus inclination angle

In terms of pressure independent loaded radius fit for vertical actuation, these grouped-order coefficient fits provide the initial coefficients which are fed into the least-squares fitting routine with upper and lower bounds to the coefficient range being set at ±500% of the initial guesses. In the case of vertical actuation pressure dependent loaded radius fitting, another step is required which groups the coefficients from these fits into orders and fits them against outer liner pressure. While the sequence of variables fit and polynomial fit order changes depending on which parameter is being fit for a certain test axis, the process remains the same.

5.4. Results

The challenge fitting tire data is effectively characterizing its inherent variability across multiple constructions of tire even if the range of test conditions is small. In order to provide an adequate sample set for testing the fits that are generated using Equations 5.1 through 5.4, a diverse set of tires is tested. This set of tires includes two super speedway, two short track, two road course, and four intermediate track constructions. Figure 5.7 through Figure 5.14 give the distribution of absolute error between the all of test data and fit data for the entire sample set of tires. Statistics for these results are presented in Table 5.2.

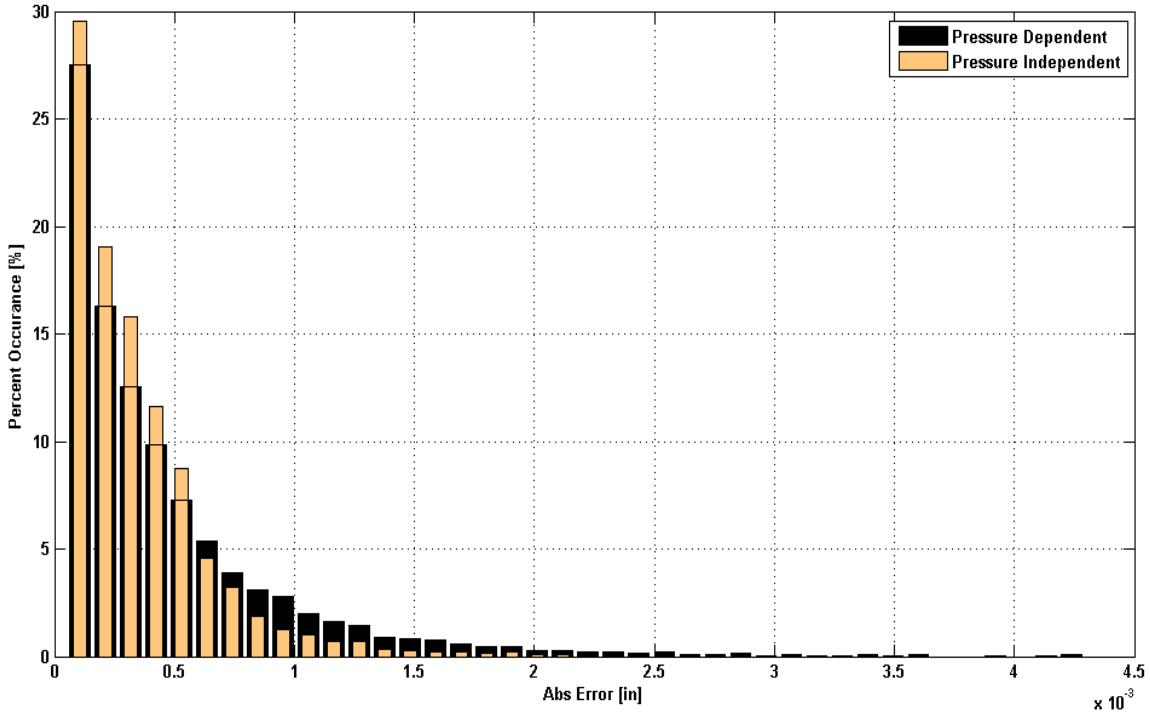

Figure 5.7: Vertical Testing: Loaded radius fit error distribution

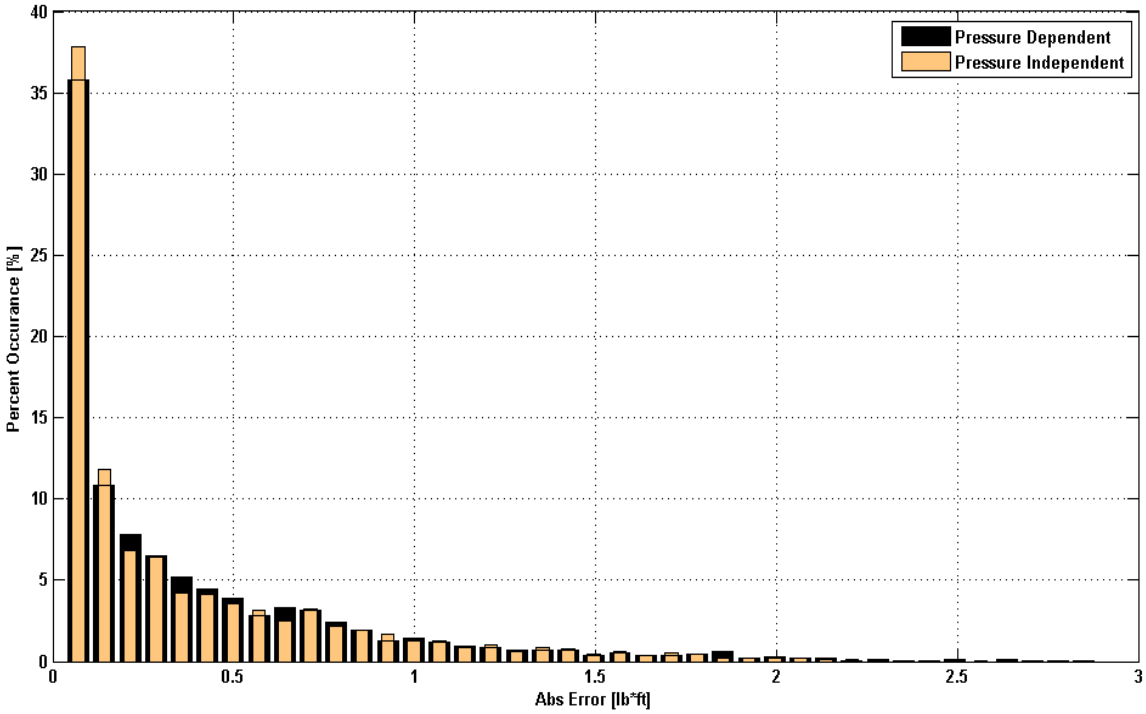

Figure 5.8: Vertical Testing: Overturning moment fit error distribution

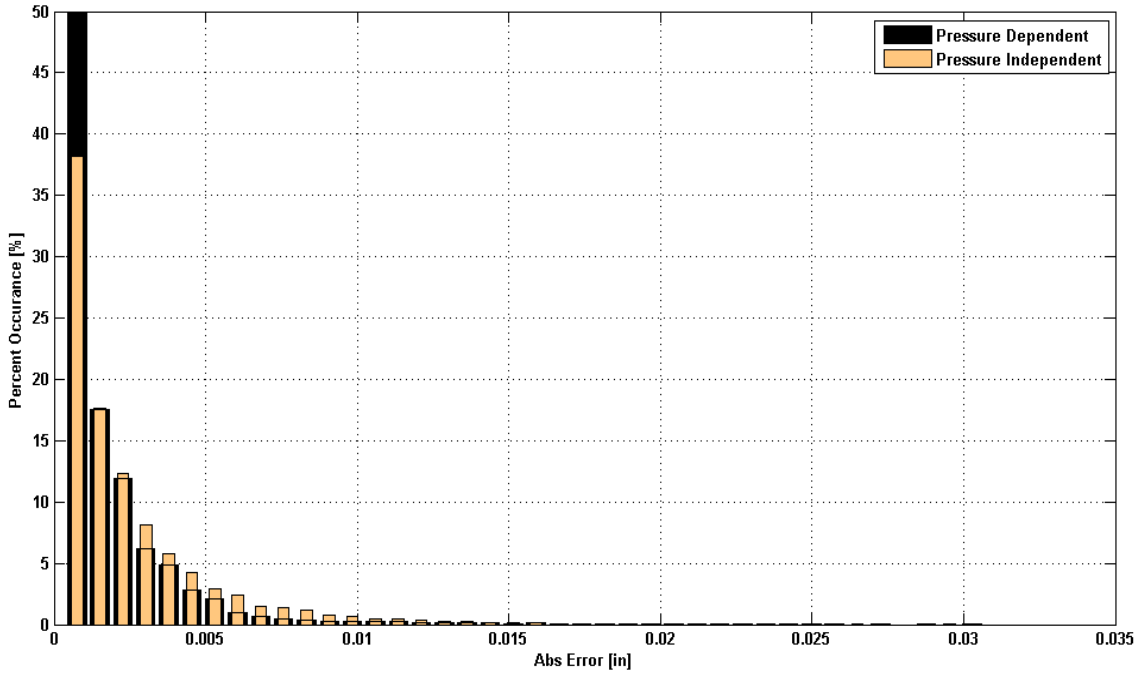

Figure 5.9: Lateral Testing: Loaded radius fit error distribution

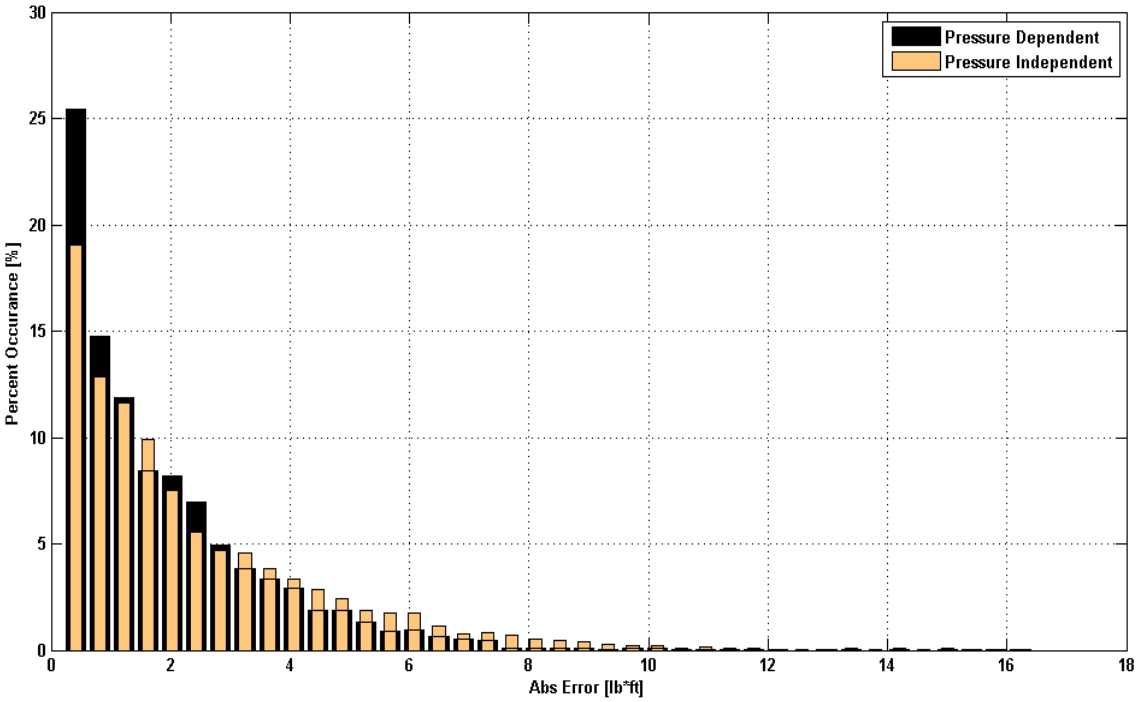

Figure 5.10: Lateral Testing: Overturning moment fit error distribution

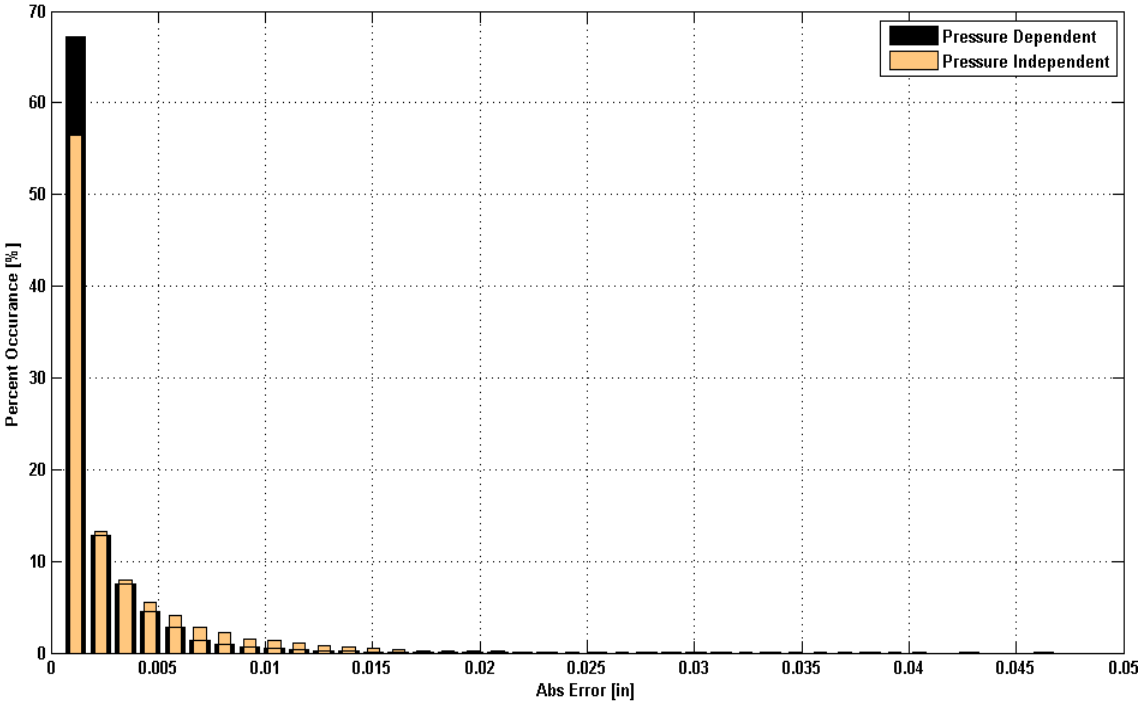

Figure 5.11: Lateral Testing: Lateral displacement fit error distribution

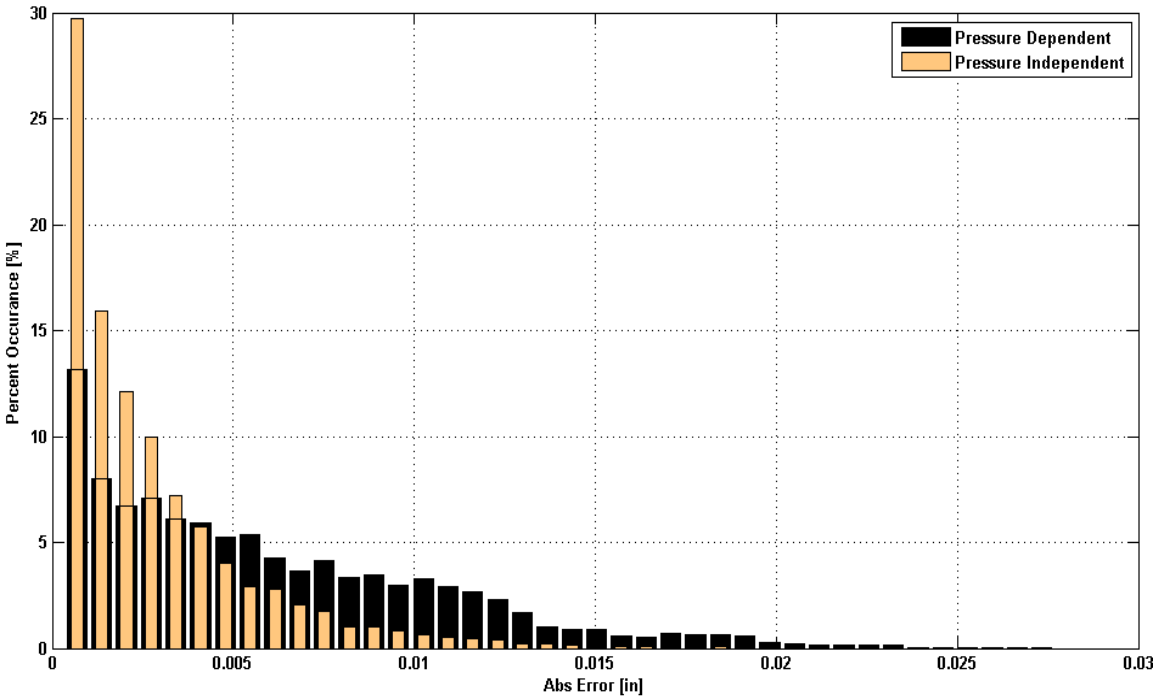

Figure 5.12: Longitudinal Testing: Loaded radius fit error distribution

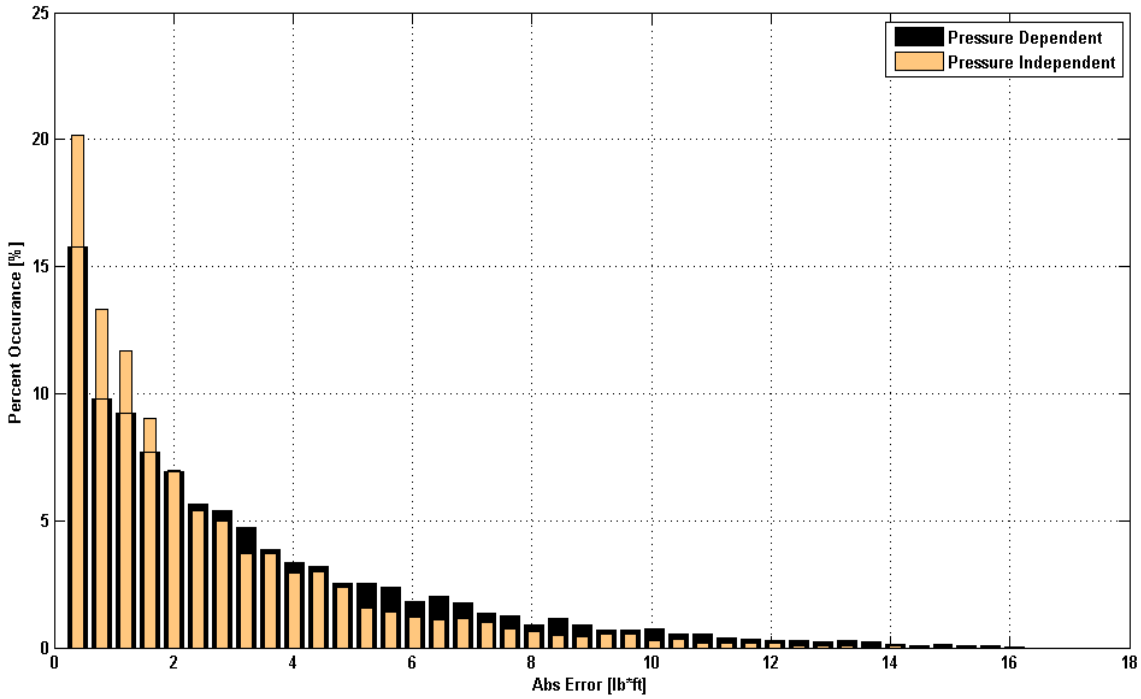

Figure 5.13: Longitudinal Testing: Overturning moment fit error distribution

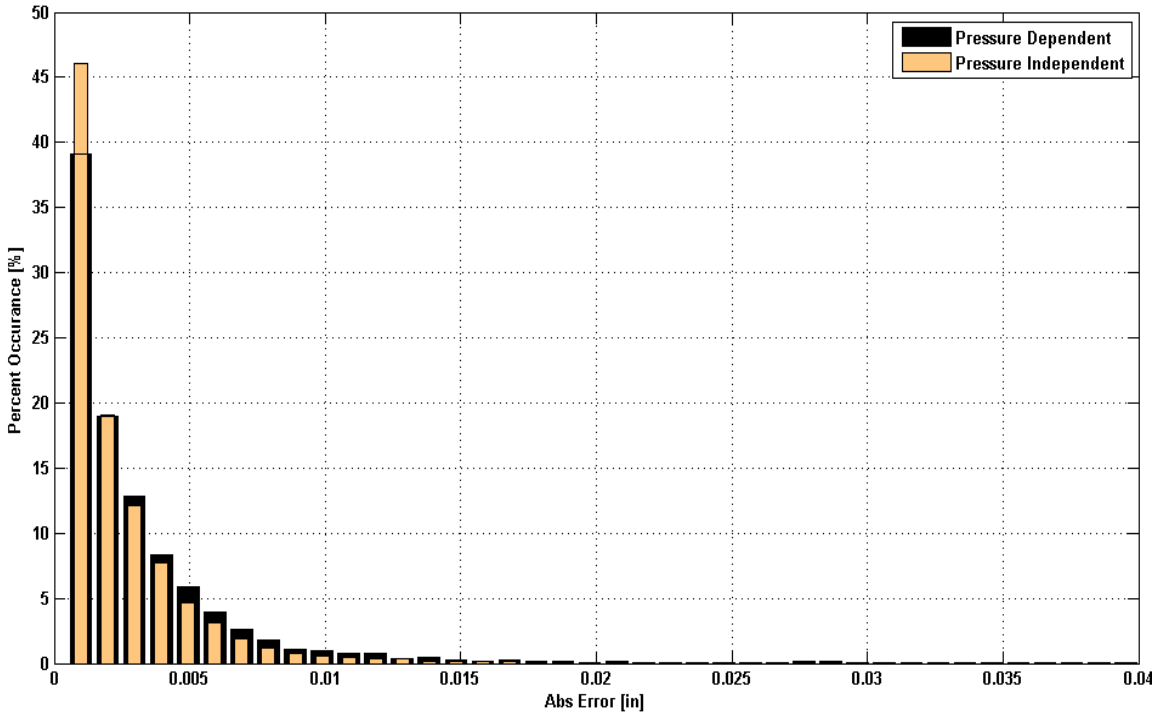

Figure 5.14: Longitudinal Testing: Longitudinal displacement fit error distribution

Table 5.2: Fitting Results Statistics

Fit Axes	Fit Parameter	Fit Type	% Error Less Than Fitting Goal
Vertical	Loaded Radius	Pressure Independent	100
		Pressure Dependent	100
	Overturning Moment	Pressure Independent	100
		Pressure Dependent	100
Lateral	Loaded Radius	Pressure Independent	100
		Pressure Dependent	100
	Overturning Moment	Pressure Independent	88
		Pressure Dependent	82
	Displacement	Pressure Independent	100
		Pressure Dependent	100
Longitudinal	Loaded Radius	Pressure Independent	100
		Pressure Dependent	100
	Overturning Moment	Pressure Independent	71
		Pressure Dependent	80
	Displacement	Pressure Independent	100
		Pressure Dependent	100

Table 5.2 shows that the majority of fit types fall below the fitting goal absolute error thresholds of 3.5 lbf-ft for overturning moment and .06in for loaded radius and displacement. As a general observation, the pressure independent fits are better than the pressure dependent ones due to less data being fit per set of coefficients. This rule does

not hold true for longitudinal overturning moment fits, though, due to the noisy nature of the data since large overturning moments are not developed. In this case, more coefficients help to fit the noisy data better. Lateral and longitudinal overturning moment fits are the only fits in which not all of the fit data exhibits an absolute error less than the fitting goals.

5.5. Tire Comparisons

In addition to fitting equation coefficients for vehicle setup or testing simulations, the tire test rig is used to analyze the differences between two similar tires. The goal of this comparison is identify if tires built with the same construction and in the same mold with only compound changes can be characterized by one set of coefficients or if every tire needs to be tested and fit individually. At the time of this paper, no tires with similar constructions from the same mold have been tested, but two tires made from the same mold but made with different construction methods have been tested. The results of these tests are shown in Figure 5.15 through Figure 5.18 which illustrates the distribution of the difference of loaded radius, overturning moment, and displacement between these tires. The difference shown is the tire with the standard construction from the tire with a modified construction method.

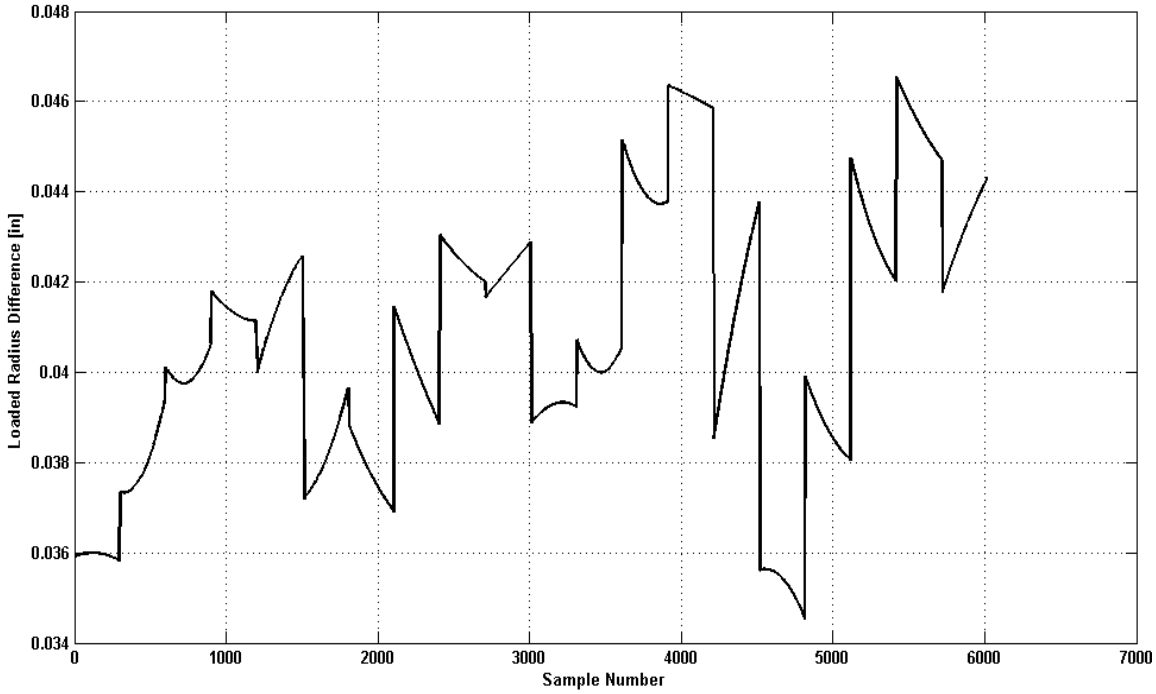

Figure 5.15: Tire comparison – Vertical testing loaded radius difference

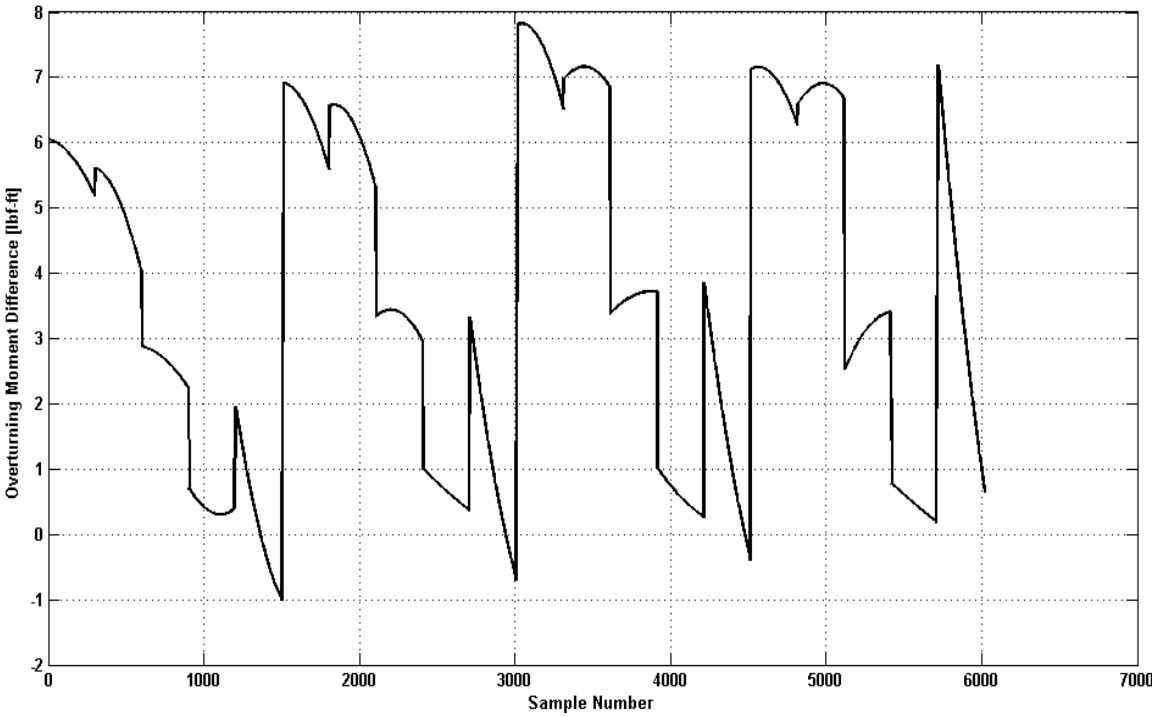

Figure 5.16: Tire comparison – Vertical testing overturning moment difference

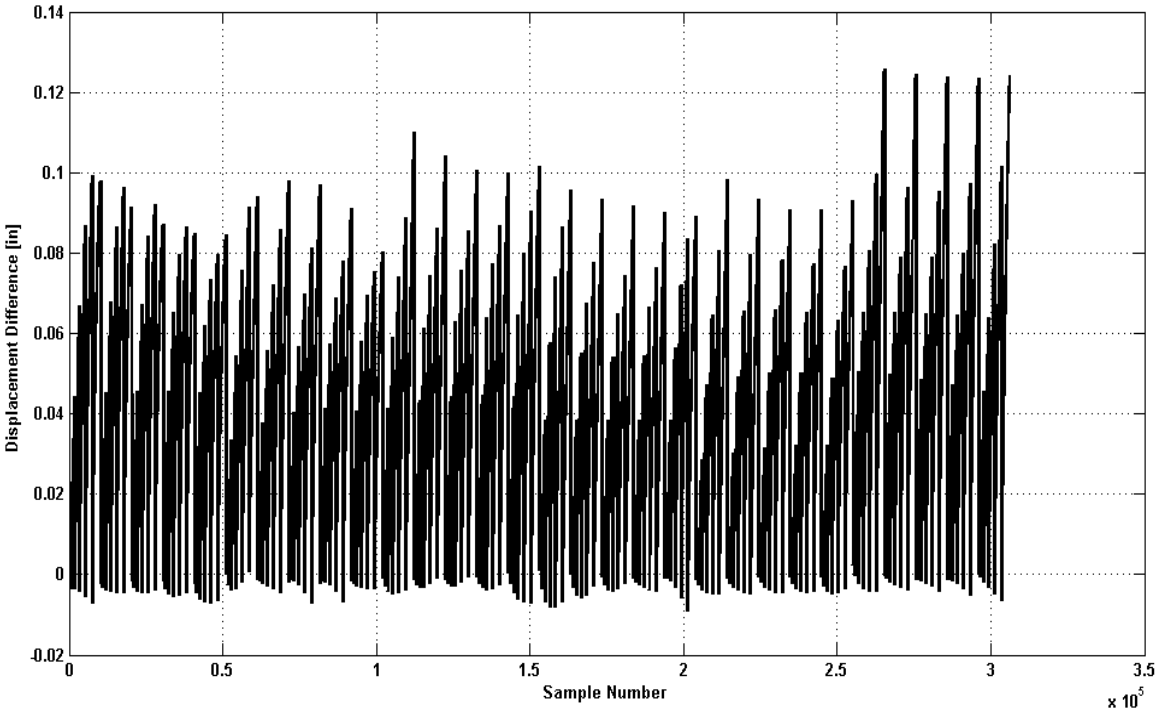

Figure 5.17: Tire comparison – Lateral testing lateral displacement difference

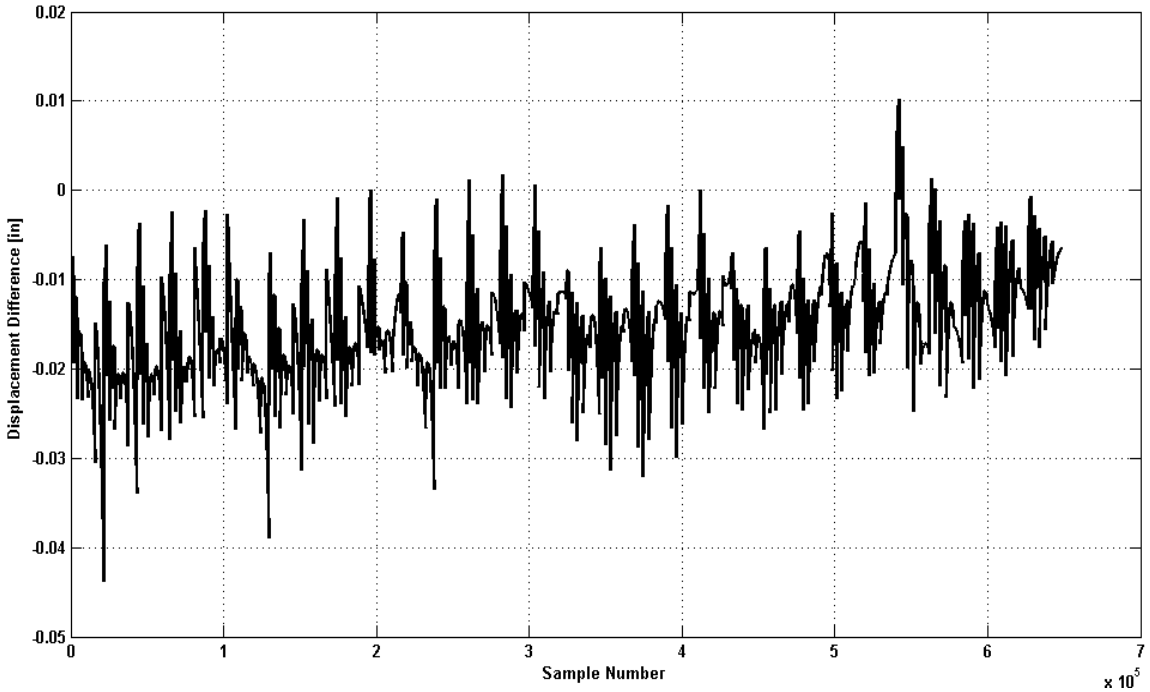

Figure 5.18: Tire comparison – Longitudinal testing longitudinal displacement difference

From these figures it is seen that while overturning moment shows little difference, the loaded radius and axial displacement are affected heavily by this

construction change. The loaded radius difference is a direct result of the two tires exhibiting different circumferences despite being built in the same tire mold. The test axis displacements indicate a difference in stiffness between these two tires with the modified construction tire being less stiff than the standard construction. While Figure 5.17 and Figure 5.18 appear to be simply noisy plots, these figures are useful in identification of global trends since they plot a large quantity of data. These figures compare the difference between the two tires across all of the conditions that are tested. These results and trend information were used by race engineers in order to advise teams on how to adjust their setups to tires assembled using the modified construction method.

5.6. Tire Rig Stiffness Continual Validation

In addition to being fit and compared, the processed data from each test is used to continually evaluate the stiffness performance of the test rig with respect to the tire being tested. This evaluation is not only aimed at affirming design goals but also identifying problems with the test rig due to a decrease in stiffness correlating to improper installation or a failing part. Figure 5.19 through Figure 5.21 give the vertical, lateral, and longitudinal spring rates of the test rig over time, respectively, while Figure 5.22 through Figure 5.24 give the corresponding measurement error over time between the test rig frame stiffness and tire stiffness for a particular test. Table 5.3 tabulates the mean and standard deviation for these measurements.

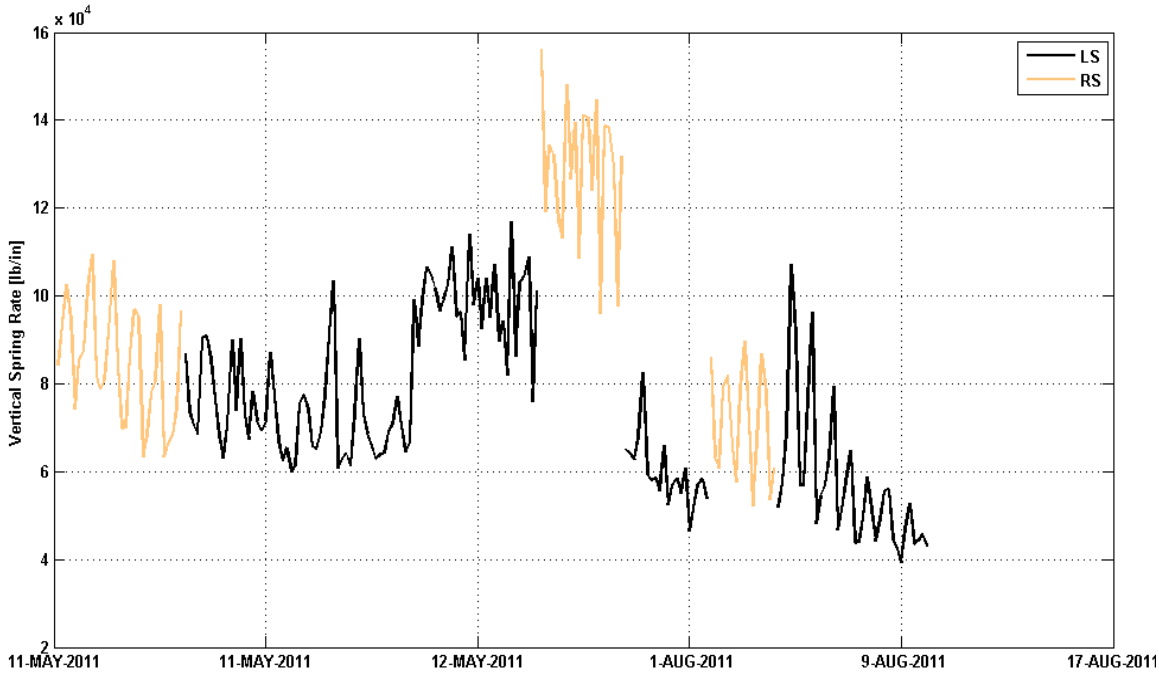

Figure 5.19: Test rig vertical spring rate

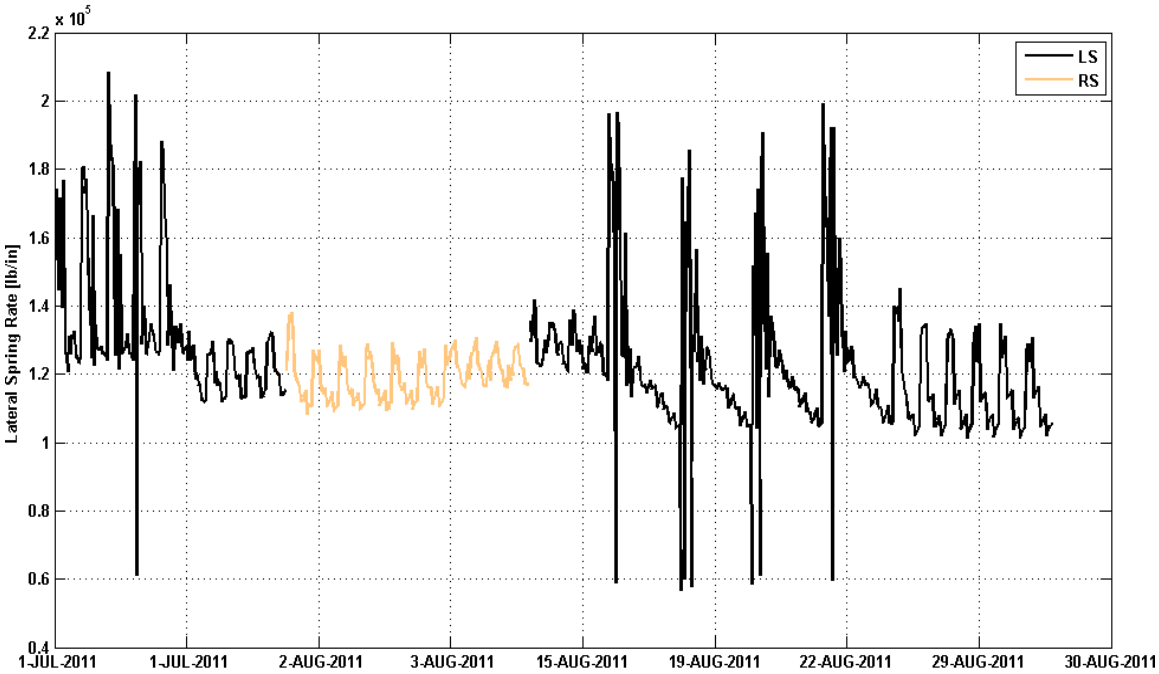

Figure 5.20: Test rig lateral spring rate

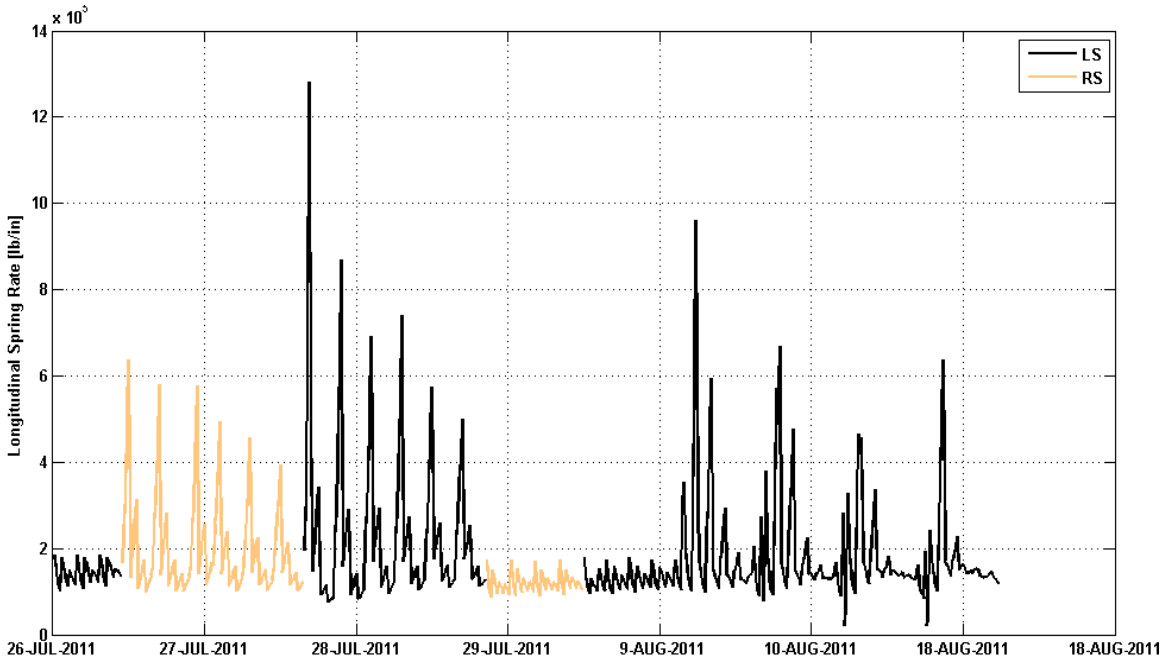

Figure 5.21: Test rig longitudinal spring rate

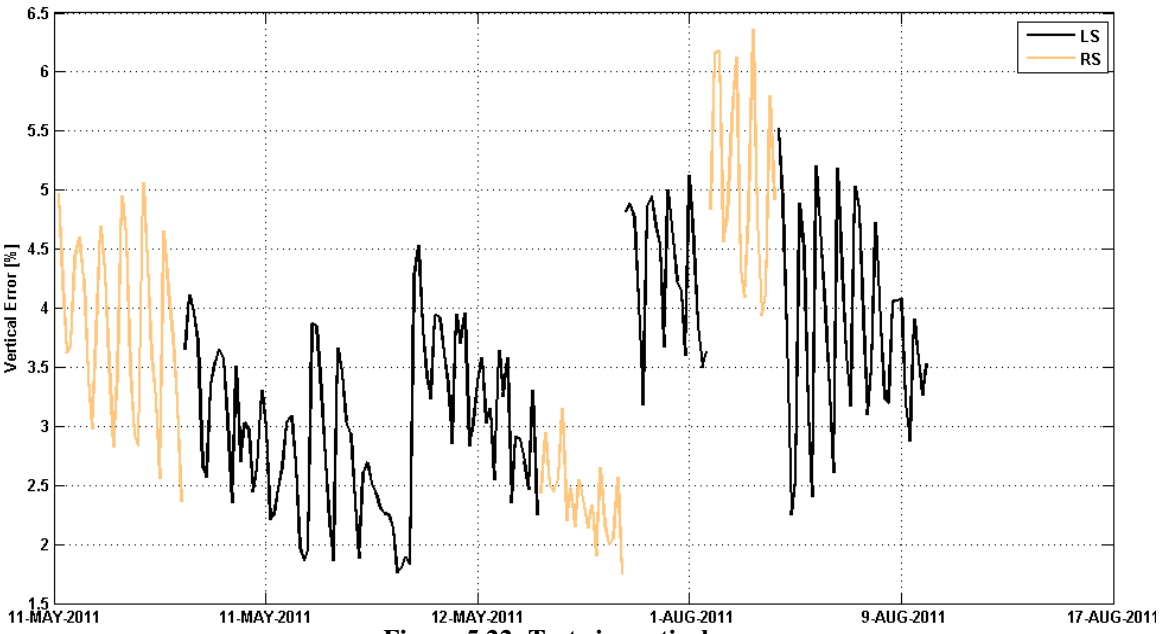

Figure 5.22: Test rig vertical error

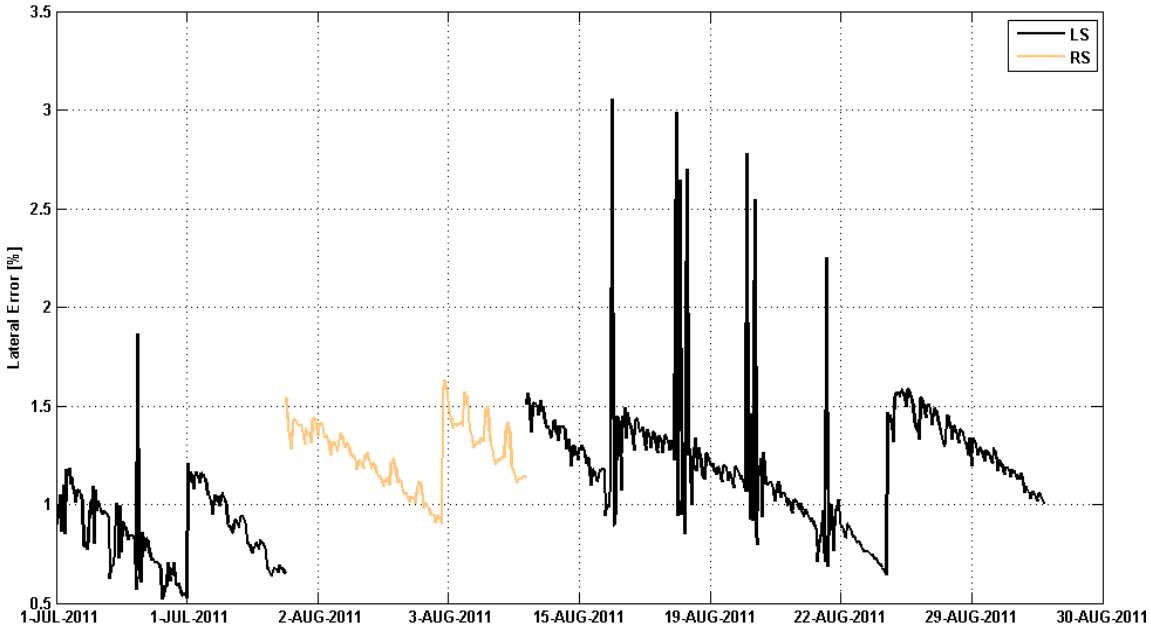

Figure 5.23: Test rig lateral error

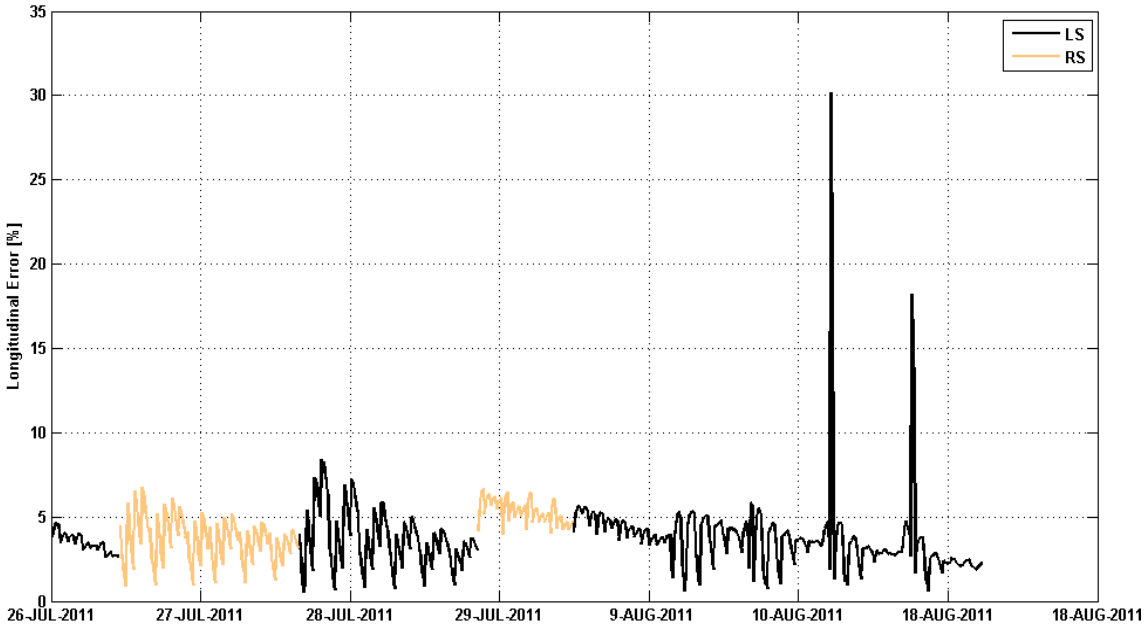

Figure 5.24: Test rig longitudinal error

Table 5.3: Test Rig Continual Validation Results

Test Axis	Spring Rate [lb/in]		Error [%]	
	Mean	Standard Dev.	Mean	Standard Dev.
Vertical	79541	24271	3.48	1.01
Lateral	122744	18469	1.14	0.29
Longitudinal	176634	120682	3.80	1.88

Table 5.3 shows that the mean plus one standard deviation of stiffness in all test axes fall under the design limit of 5 percent error with respect to tire stiffness. Notable in the spring rate figures is the deviation in spring rate from one test to the next. This deviation is due to changing inclination angles in testing such that more lateral force is applied to the test rig, with lateral being the stiffest axes of the rig. The vertical stiffness trend over time, Figure 5.19, indicates that vertical stiffness appears to be decreasing. This decrease attributed to the deflection of the static I-beam connecting rod mounts, and these mounts will be redesigned if stiffness continues to fall. The cause of the outlier peaks and valleys for longitudinal and lateral test rig stiffness are still being investigated. Longitudinal stiffness percent error is higher than is anticipated because the average longitudinal stiffness of the race tires tested is around 2000lb/in higher than the tire stiffness that is used in designing the test rig.

In addition to tracking test rig stiffness, the output data from the tire test rig is compared to rolling tire spring rate test data and the output data from a tire model that is generated from force and moment testing of a rolling tire. The comparison to the rolling tire spring rate data is performed out of academic inquiry at the moment in order to see how the values compare. An example of this comparison is shown in Figure 5.25 at 0 degrees inclination angle.

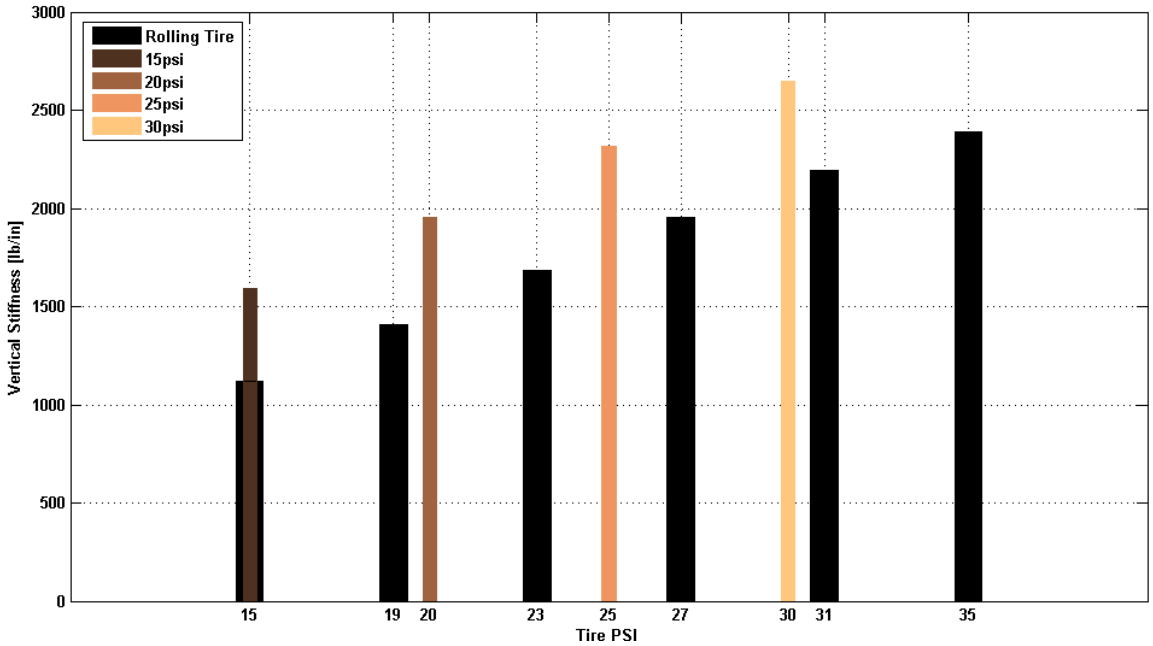

Figure 5.25: Comparison of rolling and static tire vertical spring rates

Figure 5.25 shows a trend which holds true for all of the tires presently tested when their test-rig-measured static spring rates are compared to the rolling tire spring rates: the tire test rig spring rates are 20-30% higher. The rolling tire spring rates are measured on an MTS Flat-Trac® machine while the tire is rolling without any camber, steer, or forces, other than vertical being, applied to the tire. The tests on tire test rig confirm that tire stiffness decreases with increased forward velocity (1). No model has been investigated to convert from the rolling tire spring rates to the tire test rig spring rates because overturning moment and loaded radius for the static tire model are more important, and these parameters are not easily predicted from the rolling tire force and moment test data.

Overturning moments and loaded radiuses which are measured on the static tire test rig are compared to the tire model fits of the rolling tire data, as shown in Figure 5.26 for a tire a -2degrees inclination angle. Analyzing all of the comparable data, no trend

exists that is easily discerned. Therefore, static tire model tests must be conducted on the tire test rig machine developed in this report.

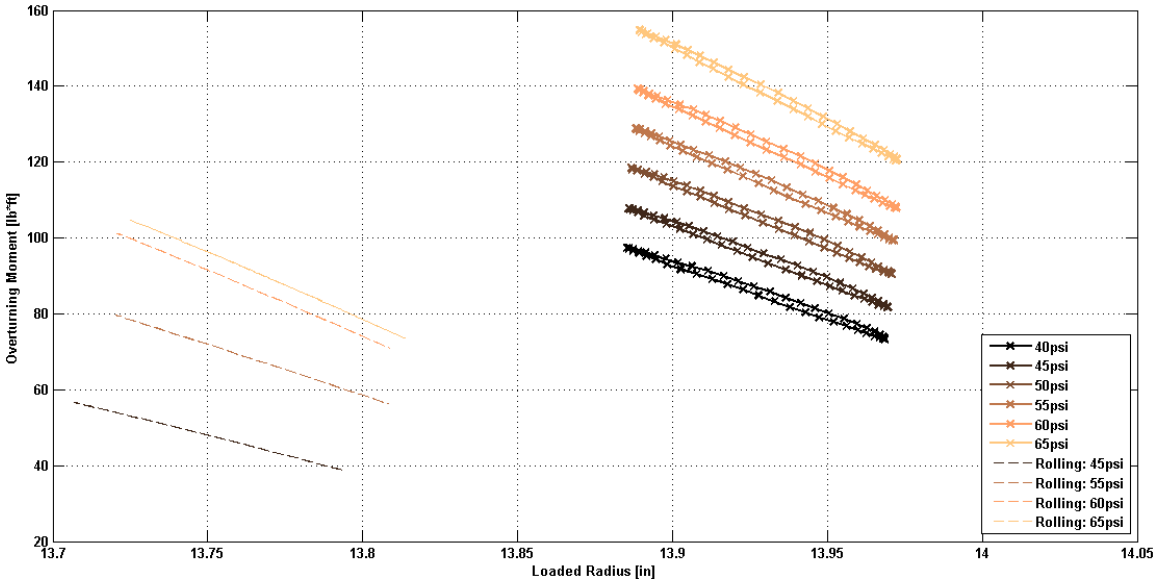

Figure 5.26: Comparison of rolling tire model and tire test rig measured overturning moment and loaded radius

6. Conclusion

The static tire test rig meets the needs of the project sponsor by being a non-permanent, reliable, fully automated, and cost effective test rig which mounts to the MTS K&C machine and delivers repeatable and useful tire data. By designing the tire test rig with the mitigation of clearances between load bearing parts in mind, the tire test rig yields data which is indicative of the pure motion of the tire during testing with only the deflection of the material of the test rig being added to the tire deflection results. This test rig material deflection is accounted for and removed from the results because the motion of the wheel and tire is measured at the hub of the wheel and the contact patch of the tire by the K&C machine. Even without subtracting motion of the test rig from the results, the stiffness of tire test rig is designed and measured to fall within the tire to tire variation of the project sponsor's race tires being tested such that the test rig deflection plays a minor role in the measurement error possible.

While accuracy of measurement is important, it comes in a close second to accurately representing the trends of the data in vehicle simulation packages. The equations that are developed to fit the loaded radius, overturning moment, and tire displacement parameters from vertical, lateral, and longitudinal axes tests on the tire test rig represent the majority of the data within the error bounds that are required. The error bounds that are established by the race team engineers are met 95 percent of the time across all of the tested data using simple polynomial equations.

The processing of the test data is completed using a MATLAB-developed GUI which allows users to load in files output from the K&C machine tire test rig tests and

quickly visualize the data. This data is then organized, fit, and output in one file using the same GUI. These output files are then used to pass the coefficients for the equations to the vehicle dynamics engineers for implementation in vehicle simulation packages. The inclusion of data from the tire test rig into simulations allows for more accurate prediction of how a vehicle reacts to setup changes in static conditions and on test rigs such as the MTS K&C machine. Virtual testing allows these vehicle dynamics engineers to better focus their real-world test plans by eliminating test conditions that are not useful, as predicted by simulation, from their test plan. These simulations also allow for the vehicle's suspension to be setup with fewer iterations needed since the effects of the static tire on the vehicle are more accurately predicted than using data from rolling tire tests.

7. Recommendations

While the testing life of the tire test rig that is described in this report is still in its infancy, a couple of improvements are possible to increase the accuracy of the test rig data and expand the testing capabilities. A redesign of the rear connecting rod mounts to a more robust layout with more than one attachment bolt would increase the rigs installation stiffness as well as increase the repeatability of installation by removing a degree of freedom from the positioning of the mount. Secondly, the frequency testing capabilities of the MTS K&C test rig should be explored such that a quasi-static tire model can be generated. The frequency limits of the elevator pads of the K&C rig are hydraulically limited to 5Hz because the first mode of the K&C rig exists at 7Hz. Therefore, to do quasi-static frequency testing above 5Hz, the hydraulic system of the K&C rig must be upgraded and its first mode shape should be increased or avoided altogether. MTS should be consulted with regards to how the test rig responds at other frequencies up to 20Hz such that they can be avoided or addressed.

References

1. Lines, J.A., and Murphy, K.: *The Stiffness of Agricultural Tractor Tires*. *J. Terramech*, 28(1): pp. 49-64. 1991

2. Langer, W.J., and Potts, G.R.: *Development of a Flat Surface Tire Testing Machine*. SAE Paper 800245, Feb. 1980.

3. Gobbi, M., Mastinu, G., and Pennati, M.: *Design and Construction of a Test Rig for Assessing Tyre Characteristics at Rollover*. SAE Paper 2002-01-2077, July 2009.

4. Davis, P. A.: *Quasi-Static and Dynamic Response Characteristics of F-4 Bias-Ply and Radial-Belted Main Gear Tires. NASA TP-3586*, Feb. 1997.

5. Essma, S. Vertical Tire Vibration Modeling. MS Thesis. Purdue University, West Lafayette, 1996. Print.

6. Lacombe, J.: *Tire Model for Simulations of Vehicle Motion on High and Low Friction Road Surfaces*. In *Proc. of the 2000 Winter Simulation Conference*, pp. 1025-1034, 2000.

7. Race Engineer #1. [Tire Engineer]. Interview. 1 April 2010.

8. Race Engineer #2. [Tire Engineer]. Interview. 10 April 2010.

9. Carr Lane Manufacturing Co. Expanding diameter pin [Catalogue]. Accessed March 5, 2010 from http://www.carrlane.com/catalog/

10. Race Engineer #3. [Vehicle Dynamics Engineer]. Interview. 5 March 2010.

11. Race Engineer #4. *Re: Static Tire Model*. E-mail to Race Engineer #2. 18 May 2011.

12. Dennis, J. E. Jr., "Nonlinear Least-Squares," *State of the Art in Numerical Analysis*, ed. D. Jacobs, Academic Press, pp. 269-312, 1977

13. Deutschman, A.D., Michaels, W.A., and Wilson, C.E.; Machine Design Theory and Practice. MacMillian Publishing, 1975.

14. *AISI 1020 Steel, Cold Rolled*. MatWeb. Accessed March 5, 2010 from http://www.matweb.com/index.aspx

15. SAE Standard, J429. Approved by American National Standards Institute, July 18, 1984.

16. Suggested Tightening Torque Values to Produce Corresponding Bolt Clamping Loads. Spaeneur Fasteners [Catalogue], p D.48. Accessed March 15, 2010 from http://www.spaenaur.com/pdf/sectionD/D48.pdf

Appendix A: Bill of Materials

Table A.1: Frame Bill of Materials

Sub Assembly	Component	Mounting Hardware	QTY	Supplier	Part Number
	Tubing Structure		1	Sponsor	P1
	Frame Flange		2	Sponsor	P2
	Hubplate Adapter		2	Sponsor	P3
		Dowel Pin	4	McMaster-Carr	97352A330
		7/16-20" - 7/8" Long, Hex Head Cap Screw	8	McMaster-Carr	92620A698
	Hub		2	Sponsor	P4
		Wheel Studs	5	Sponsor	300-7714
		Precision Ball Bearing 1	2	Timken	2MMV9310HX
		Precision Ball Bearing 2	2	Timken	2MM211WI
	Hub Snout		2	Sponsor	P5
		1/2"-13 - 1" Long Socket Head Cap Screw	4	McMaster-Carr	92220A261
		Dowel Pin	2	McMaster-Carr	97352A330
	Wheel		2	-	-
	Tire		2	-	-
	Modfied Drive Plate		2	Sponsor	794-1LAX2
	Axle Bearing Holder		2	Sponsor	P6
		2-19/32" OD Thrust Bearing	1	McMaster-Carr	60715K29
		1/4"-20, 3/4" Long Button Head Allen Bolt	4	McMaster-Carr	91255A540
	Drive Axle		2	Sponsor	P7
		N-06 Shaft Collar	1	McMaster-Carr	6343K17
	Drive-Plate Plate		2	Sponsor	P8
		5/16"-24 Allen Head Cap Screw	3	McMaster-Carr	91251A378
		1/2"-13 - 1" Long Socket Head Cap Screw	1	McMaster-Carr	92220A261
	Right Angle Gearbox		2	Tolomatic	0122-0400
	DC Motor Shaft Adapter		2	Sponsor	P9
		#10-32 Set Screw	1	McMaster-Carr	91385A337
	Motor-Mounted Gearbox		1	Sponsor	P10
		Socket Head Cap Screw #10-24 - 2"	4	McMaster-Carr	91251A253
Motor Gearhead			2	Sponsor	P11
	Gearbox to Motor Adapter		1	Sponsor	P12
	Motor Gear		1	SDP-SI	A1C8MYS06018
		#4-40 Set Screw	1	McMaster-Carr	91385A105
	Hex Shaft Motor Spacer		8	Sponsor	P13
		M5x.08 - 16mm Long Hex Bolt	2	McMaster-Carr	91280A226
	Groschopp DC Motor 2		2	Groschopp	P14
		M5x.08 - 16mm Long Hex Bolt	2	McMaster-Carr	91280A226
Gearbox			2	Sponsor	-
	Gearbox Mount		2	Sponsor	P15
		T-Nut	1	McMaster-Carr	47065T142
		1/4"-20, 3/8" Long Low-Profile Allen Bolt	1	McMaster-Carr	92220A182
		1/4"OD, 1.125" Long Clevis Pin	1	McMaster-Carr	98306A160
		1/16" Wire Dia. Cotter Pin	1	McMaster-Carr	98335A049
	Mounting Tab		2	Sponsor	P16
		1/4"-20, 3/8" Long Low-Profile Allen Bolt	1	McMaster-Carr	92220A182
		1/4"OD, 1.125" Long Clevis Pin	1	McMaster-Carr	98306A160
		1/16" Wire Dia. Cotter Pin	1	McMaster-Carr	98335A049
		1/4"-28 RH-Thread Rod End	1	McMaster-Carr	4483T201
		1/4"-28 LH-Thread Rod End	1	McMaster-Carr	4483T202
		3", 1/4-28 Female-Threaded Connecting Rod	1	McMaster-Carr	8419K220
	Gearbox Spacer		2	Sponsor	P17
		1/4"-20, 3/8" Long Low-Profile Allen Bolt	4	McMaster-Carr	92220A182
Mounting Plate Assembly			2	Sponsor	P18
	Mounting Plate 1		1	Sponsor	P19
	Mounting Plate 2		1	Sponsor	P20
	Mouting Plate Rib		3	Sponsor	P21
		M12X1.75-45mm Hex Screw	4	McMaster-Carr	91310A722
	Frame Mount		4	Sponsor	P22
		3/8"OD, 2.125" Long Clevis Pin	1	McMaster-Carr	98306A722
		1/8" Wire Dia. Cotter Pin	1	McMaster-Carr	98335A064
	Connecting Rod 1		2	Sponsor	P23
	K&C Mount		2	Sponsor	P24
		3/8"OD, 2.125" Long Clevis Pin	1	McMaster-Carr	98306A722
		1/8" Wire Dia. Cotter Pin	1	McMaster-Carr	98335A064
		M12X1.75-50mm Socket Head Cap Screw	1	McMaster-Carr	91290A626
	Vibration Damping Tube Mount		2	ZSI	S-5024S
		1/4"-20, 3" Long Hex Bolt	2	McMaster-Carr	91247A554
		1/4"-20 Nylon Locknut	2	McMaster-Carr	93298A110
	Tube Mount		2	Sponsor	P25
		3/8"OD, 1.375" Long Clevis Pin	1	McMaster-Carr	97245A337
		1/8" Wire Dia. Cotter Pin	1	McMaster-Carr	98335A064
	Turnbuckle Rod		1	Sponsor	P26
		3/8"-24 RH-Thread Rod End	1	McMaster-Carr	6072K230
		3/8"-24 LH-Thread Rod End	1	McMaster-Carr	6072K231
	Connecting Rod 2		2	Sponsor	P27
Floor Mount			2	Sponsor	P28
	Floor Mount Clevis		1	Sponsor	P29
	Floor Mount Plate		1	Sponsor	P30
		3/8"OD, 1.375" Long Clevis Pin	1	McMaster-Carr	97245A337
		1/8" Wire Dia. Cotter Pin	1	McMaster-Carr	98335A064
		Epoxy Concrete Anchor	4	McMaster-Carr	93980A190

Table A.2: Gearbox Bill of Materials

Sub Assembly	Component	Mounting Hardware	QTY	Supplier	Part Number
Gearbox Frame			1	Sponsor	-
	Gearbox1a		4	Sponsor	P31
	Gearbox1b		2	Sponsor	P32
	Gearbox2		4	Sponsor	P33
	Gearbox3		4	Sponsor	P34
		3-Way Corner Connector	8	McMaster-Carr	47065T244
		Single, 2-Hole, 90° Corner Bracket	6	McMaster-Carr	47065T223
		Modified Corner Bracket	2	Sponsor	P35
		T-Nut	16	McMaster-Carr	47065T142
		1/4"-20, 3/8" Long Low-Profile Allen Bolt	40	McMaster-Carr	92220A182
Main Bearing Holder			-	Sponsor	-
	Bearing Holder 1		2	Sponsor	P36
		7/8" OD Ball Bearing	1	McMaster-Carr	2342K185
		T-Nut	2	McMaster-Carr	47065T142
		1/4"-20, 1/2" Long Button Head Allen Bolt	2	McMaster-Carr	91255A537
Secondary Main Bearing Holder			3	Sponsor	-
	Bearing Holder 4		1	Sponsor	P37
	7/8" OD Ball Bearing		1	McMaster-Carr	2342K185
		T-Nut	2	McMaster-Carr	47065T142
		1/4"-20, 3/4" Long Button Head Allen Bolt	2	McMaster-Carr	91255A540
Secondary Bearing Holder			1	Sponsor	-
	Bearing Holder 3		1	Sponsor	P38
	2" OD Ball Bearing		1	McMaster-Carr	2342K191
	Offset Bearing Holder 3		1	Sponsor	P39
		1/4"-20 Thread, 1-1/2" Long Allen Bolt	2	McMaster-Carr	91251A546
	Bearing Holder 2		1	Sponsor	P40
		T-Nut	2	McMaster-Carr	47065T142
		1/4"-20, 1/2" Long Button Head Allen Bolt	2	McMaster-Carr	91255A537
		#6-32 Nylon Locknut	4	McMaster-Carr	90631A007
	Linear Rotational Bearing		2	McMaster-Carr	6485K110
	Linear Bearing Housing		2	McMaster-Carr	9804K200
		#6-32, 5/8" Button Cap Screw	4	McMaster-Carr	91255A150
	Air Cylinder Holder		1	Sponsor	P41
		T-Nut	2	McMaster-Carr	47065T142
		1/4"-20, 3/4" Long Button Head Allen Bolt	2	McMaster-Carr	91255A540
	Air Cylinder		1	McMaster-Carr	6498K329
		Push-to-Connect UNF Fitting	2	McMaster-Carr	51025K167
		Push-to-Connect NPTF Fitting	2	McMaster-Carr	51055K7
		Quick-Disconnect Female Hose Coupling	2	McMaster-Carr	6534K18
		Nylon Tubing	-	McMaster-Carr	5112K52
	Air Cylinder Mounting Plate		1	Sponsor	P42
	L-Bracket		1	Sponsor	P43
		1/4"-20, 3/8" Long Low-Profile Allen Bolt	1	McMaster-Carr	92220A182
		3/8-16 Flat Head Bolt	1	McMaster-Carr	90005A632
		3/8"-16 Nut	3	McMaster-Carr	93827A225
	Linear-Rotation Bearing Plate		1	Sponsor	P44
	Driveshaft 1		1	Sponsor	P45
		5/16"-18 Nut	1	McMaster-Carr	93827A219
		Shaft E-clips	2	McMaster-Carr	97431A320
	Hex Key		1	Sponsor	P46
		Compression Springs	2	McMaster-Carr	9434K44
		Spring Shim	3	McMaster-Carr	93574A211
		3/8"-16 Nylon Locknut	1	McMaster-Carr	90630A121
	Driveshaft 3		1	Sponsor	P47
		5/16"-18 Nut	2	McMaster-Carr	93827A219
		Shaft E-clips	1	McMaster-Carr	97431A320
	Driveshaft 4		1	Sponsor	P48
		5/16"-18 Nut	2	McMaster-Carr	93827A219
		Shaft E-clips	5	McMaster-Carr	97431A320
	Driveshaft 2		1	Sponsor	P49
		Shaft E-clips	1	McMaster-Carr	97431A320
		3/8"-16 Nut	3	McMaster-Carr	93827A225
	Input Side Gear		2	Sponsor	P50
		Keyway 1	2	Sponsor	P51
	Output Side Gear		2	Sponsor	P52
		Keyway 2	2	Sponsor	P53
	Pin Gear		1	Sponsor	P54
		Pin Gear Retaining Clips	2	McMaster-Carr	97633A300
	Worm Gear		1	Sponsor	P55
		Keyway 3	1	Sponsor	P56
	Expanding Diameter Pin		1	Carr-Lane	CL-10-EXPH-1.00
	Sensor Holder		1	Sponsor	P57
		T-Nut	2	McMaster-Carr	47065T142
		1/4"-20, 1/2" Long Button Head Allen Bolt	2	McMaster-Carr	91255A537
		Photoelectric Sensor	2	Banner Engineering	M12NFF25Q8
		M12X1.0 Nut	4	McMaster-Carr	91415A150
	DC Motor Flange		1	Sponsor	P58
		1/4"-20, 5/8" Long Button Head Allen Bolt	4	McMaster-Carr	91255A539
		T-Nut	4	McMaster-Carr	47065T142
		1/4"-20 Standoff	4	McMaster-Carr	93620A194
		1/4"-20 Square Nut	4	McMaster-Carr	94859A111
	Groschopp DC Motor 1		1	Groschopp	PM8014-2006
		1/4"-20, 3/4" Long Button Head Allen Bolt	4	McMaster-Carr	91255A540
Tertiary Bearing Holder			1	Sponsor	-
	Bearing Holder 5		1	Sponsor	P59
	5/8" OD Ball Bearing		1	McMaster-Carr	2342K183
		T-Nut	2	McMaster-Carr	47065T142
		1/4"-20, 1/2" Button Head Allen Bolt	2	McMaster-Carr	91255A537
	Bearing Cap		1	Sponsor	P60
		6-32, 1/4" Button Head Allen Bolt	2	McMaster-Carr	91255A144
	Driveshaft 5		1	Sponsor	P61
		1/4" Shaft Snap Rings	2	McMaster-Carr	91590A113
		#10-24 Nylon Locknut	1	McMaster-Carr	90633A011
		Spider Coupler Part 1	1	McMaster-Carr	2401K145
		Spider Coupler Part 2	1	McMaster-Carr	2401K142
		Spider Coupler Part 3	1	McMaster-Carr	2401K85
	Worm		1	SDP-SI	A 1Q55-N24
		#4-40 Set Screw	2	McMaster-Carr	91385A105

Appendix B: Component FEA

Solidworks Simulation is used to perform FEA on critical components in order to validate their design under projected test rig loading conditions. These components are evaluated with respect to their ability to handle the test loads with a factor of safety greater than 1.5 and deflect an amount suitable to the part. This deflection evaluation is specified in each component sub-section.

B.1 Wheel / Tire Mounting Assembly

B.1.1 Model Setup

While an FEA for these components is completed in Appendix F, that FEA includes the weldment structure through mixed meshing and as such is performed only to analyze the deflection of the entire structure. This FEA of the wheel/tire mounting assembly aims to remove the weldment structure from the analysis and look at component stresses as well as deflections. The model which is used in this analysis is shown in Figure B.1, and the component list is given in Table B.1.

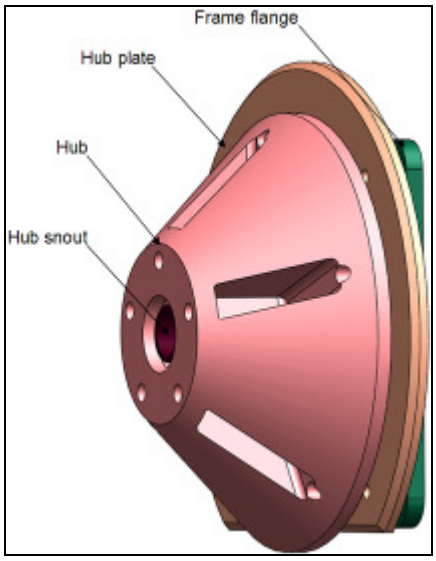

Figure B.1: Hub assembly FEA model

Table B.1: Hub Assembly FEA Components

Part	Material / Sizing
Frame Flange	Steel 4130 Normalized @ 870°C
Hub Snout Mounting Plate	Steel 4130 Normalized @ 870°C
Hub	Steel 4130 Normalized @ 870°C
Hub Snout	Steel 4130 Normalized @ 870°C

B.1.2 Connections

Figure B.2 shows that in lieu of the frame tubing connecting to the backside of the frame flange plate, a fixed constraint is used in order to simulate worse case scenario in which all the hub snout and attached components absorb all of the applied loading. Contact sets between all parts are set to no penetration.

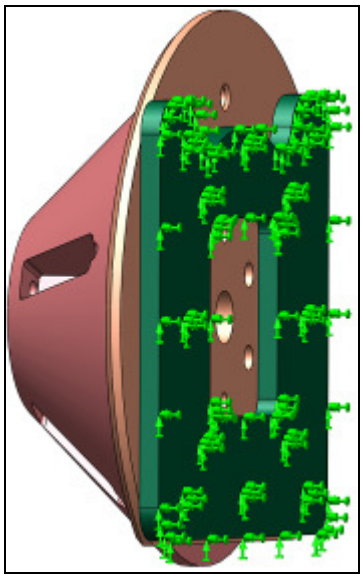

Figure B.2: Frame flange fixed constraint

The entire list of connections is given in Table B.2.

Table B.2: Hub Assembly FEA Connections

Part	Connection to	Location	Connection Type	Connection Details
Frame flange	-	Back face	Fixed	-
Hub snout mounting plate	Frame flange	Four corners of frame flange	Pin	No rotation and no translation
Hub snout mounting plate	Frame flange	Bolt circle	Bolt	7/16-20 with 145000psi tensile strength and 10000lbf clamping force
Hub snout	Hub snout mounting plate	Back face of mounting plate	Pinned at top and bottom of bolt circle	No rotation and no translation
Hub snout	Hub snout mounting plate	Back face of mounting plate	Bolted at remaining bolt circle locations	7/16-20 with 145000psi tensile strength and 10000lbf clamping force
Hub	Hub snout	Bearing surfaces	Rigid connector	-
Hub	Hub snout mounting plate	Indexing hole	Pin	No rotation and no translation

B.1.3 Loads

The loads which are used in the FEA are set by the test range to which the rig is expected to be subjected. The load is applied as a remote point load in plane with the contact face between the wheel and the hub at the contact patch of the sponsor's nominal

race tire, which yields a hub center to contact patch radius of 13.875in. Table B.3 gives the forces that are applied in the FEA coordinate system.

Table B.3: Hub FEA Loading Conditions

Axes	Force [lbf]	Load Location
Vertical (Y)	-6000	Wheel stud holes
Lateral (Z)	±4000	Face of wheel stud holes
Longitudinal (X)	±5000	Wheel stud holes

Figure B.3 through Figure B.5 illustrate these loads and locations with respect to the hub assembly model. While these locations are not entirely realistic representations of how the loads applied to the tire are transferred to the hub, they provide a reasonable approximation.

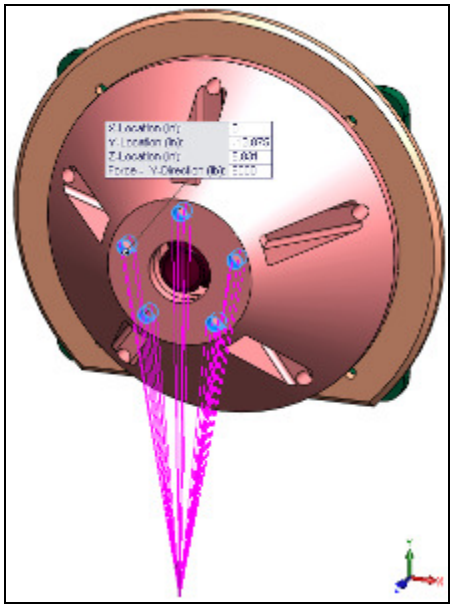

Figure B.3: Hub vertical loading

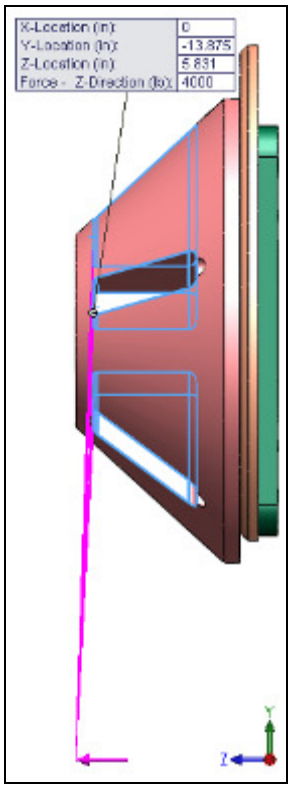

Figure B.4: Hub lateral loading

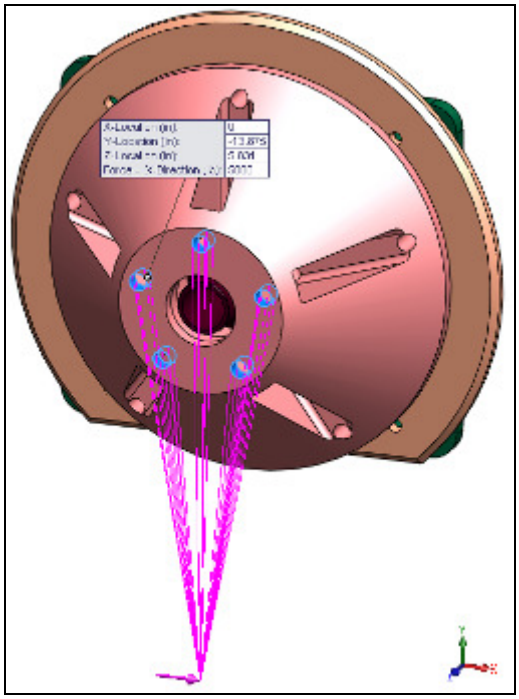

Figure B.5: Hub longitudinal loading

B.1.4 Mesh

The mesh for the hub assembly FEA is documented by Figure B.6 through Figure B.8. Mesh controls are used at bolt or pin locations and on the hub snout in order to increase mesh density around areas where stress evaluation is critical. Global mesh element size is .477in with a tolerance of .0277in. Mesh controls are set to half of these values.

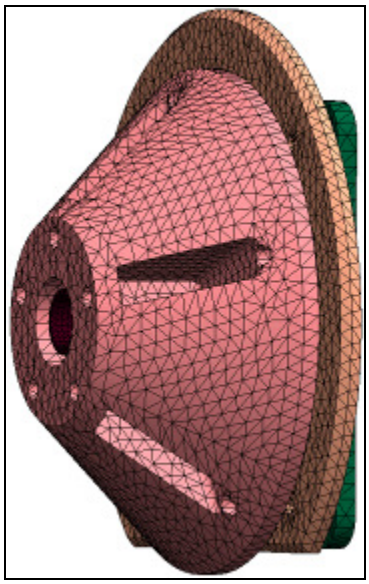

Figure B.6: Hub assembly FEA mesh - ISO

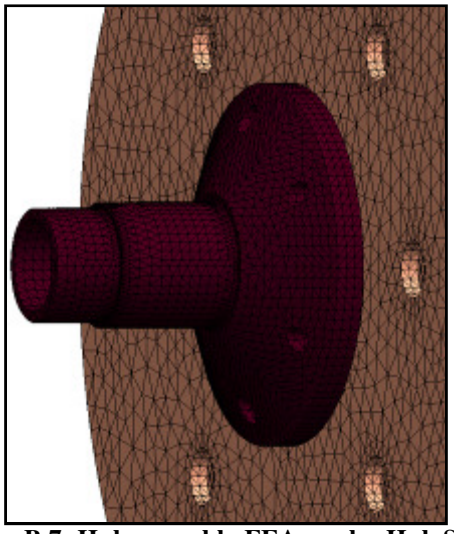

Figure B.7: Hub assembly FEA mesh - Hub Snout

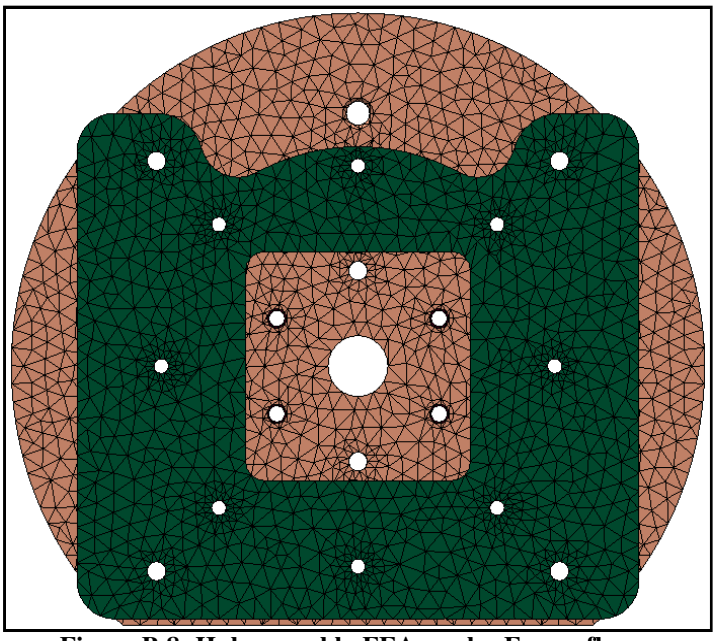

Figure B.8: Hub assembly FEA mesh - Frame flange

B.1.5 Results

B.1.5.1 Summary

The area of interest of FEA results is the stress response of the parts of the hub assembly. In this regard, the parts are analyzed in order to make sure that they exhibit a factor of safety of greater than 1.5. While this loading scenario with the backside of the frame flange being fixed is unrealistic because it disregards the deflection of the frame, the loading scenario does place the parts of the assembly in a worst case situation where the frame is rigid. In addition to stress being investigated, deflection is monitored in order to evaluate the stiffness of this assembly when it is decoupled from the frame deflection. Table B.4 gives the results of the FEA.

Table B.4: Hub FEA Results

Test Axis	Factor of Safety		Max Displacement	Stiffness
	Minimum	Location	in	lb/in
Vertical	2.23	Hub snout	.0025	2400000
Lateral	1.64	Hub snout	.011	364000
Longitudinal	1.58	Hub snout	.0056	893000

Because there is no frame deflection included in this model as of that in Appendix F, stress in the hub snout region is amplified with the maximum stress being located on the underside of the bolted end of the hub snout. Even in this unrealistic constraint situation, the hub snout exhibits a minimum factor of safety of 1.58 for a couple elements with the majority of factor of safety existing above 2. The stiffness values in Table B.4 show that the hub assembly is very stiff on its own and increasing the stiffness of these parts has little return on the stiffness of the entire frame assembly. Figure B.9 through Figure B.20 graphically depict the results given in Table B.4. All of the bolts and pins in the assembly are subjected to stresses less than their yield stresses. It is also important to note that these components will not be subjected to this amount of loading in normal test conditions. Normal test conditions will impart loads at nearly half of the loads that the test rig is designed to handle. Therefore, it can be said that the stress on these components falls well below the endurance limit of the materials and as such, the design life of this test rig is nearly infinite.

B.1.5.2 Vertical Loading Figures

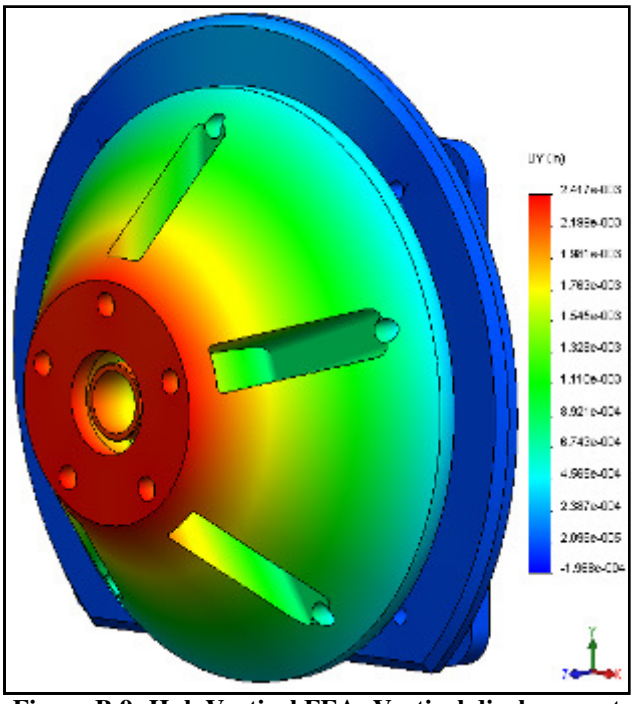

Figure B.9: Hub Vertical FEA -Vertical displacement

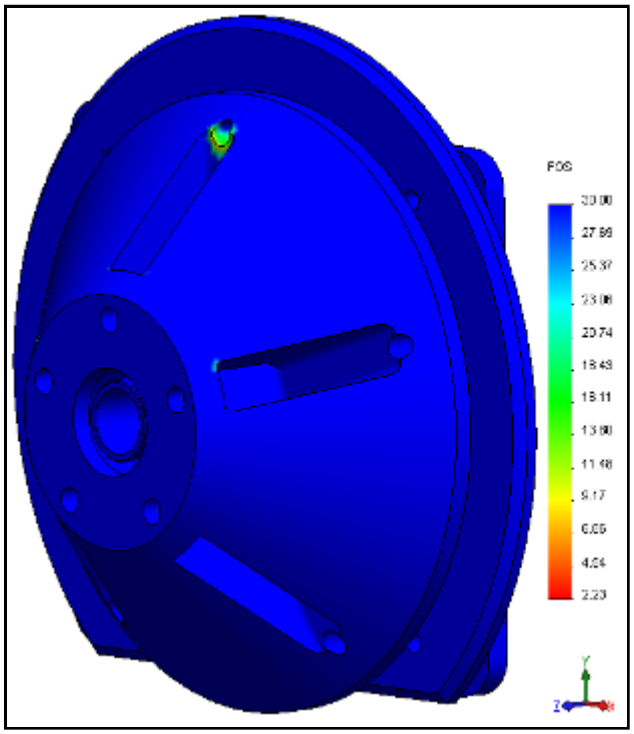

Figure B.10: Hub Vertical FEA - Hub factor of safety distribution

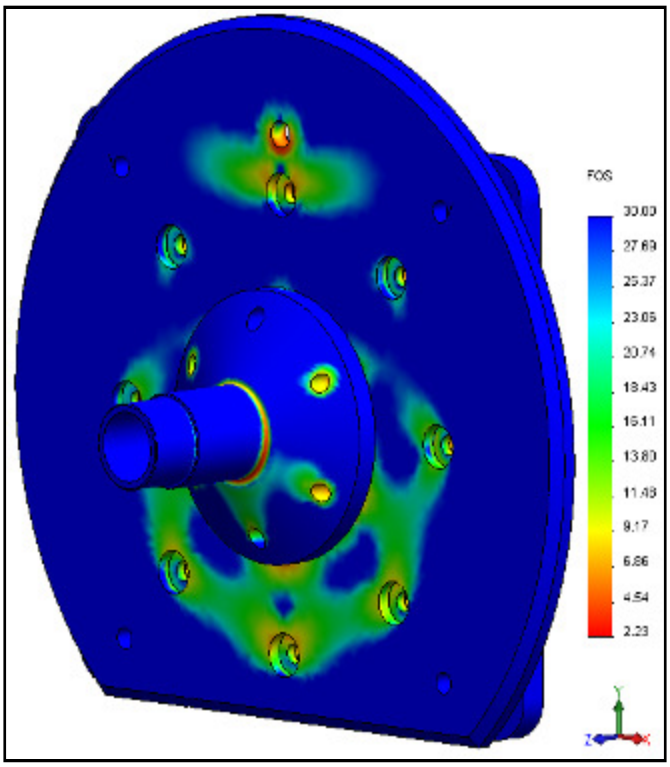

Figure B.11: Hub Vertical FEA - Snout factor of safety distribution

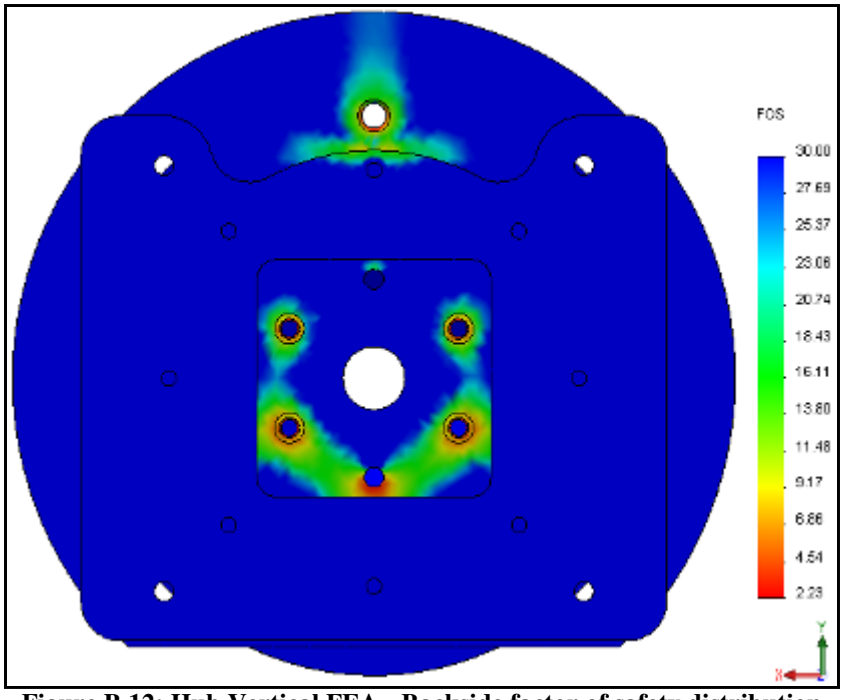

Figure B.12: Hub Vertical FEA - Backside factor of safety distribution

B.1.5.3 Lateral Loading Figures

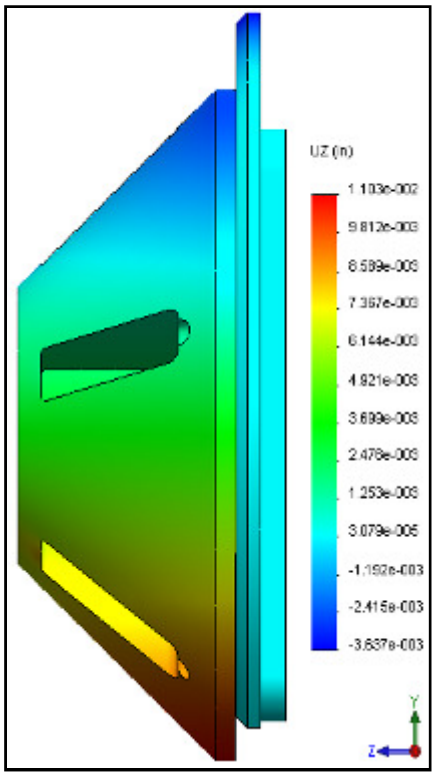

Figure B.13: Hub Lateral FEA - Lateral displacement

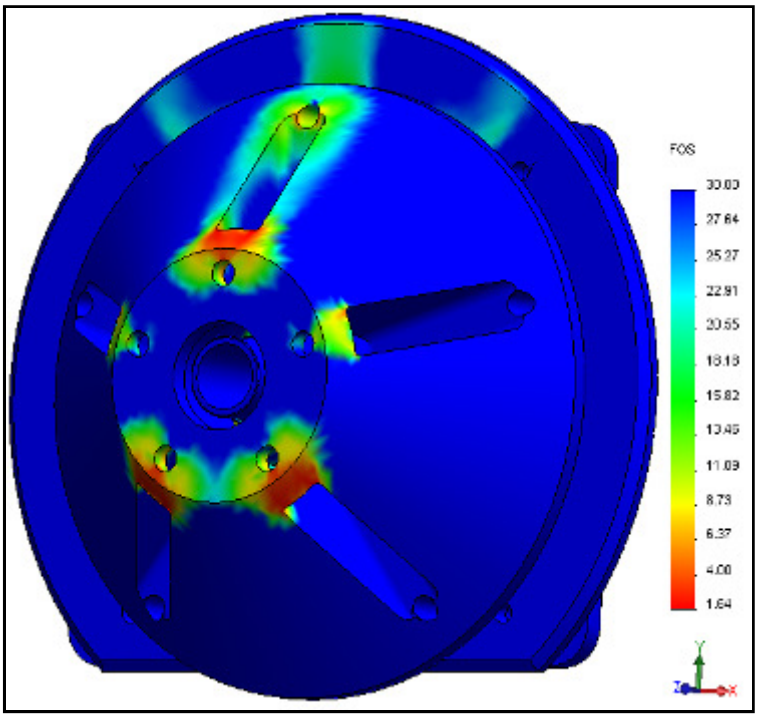

Figure B.14: Hub Lateral FEA - Hub factor of safety distribution

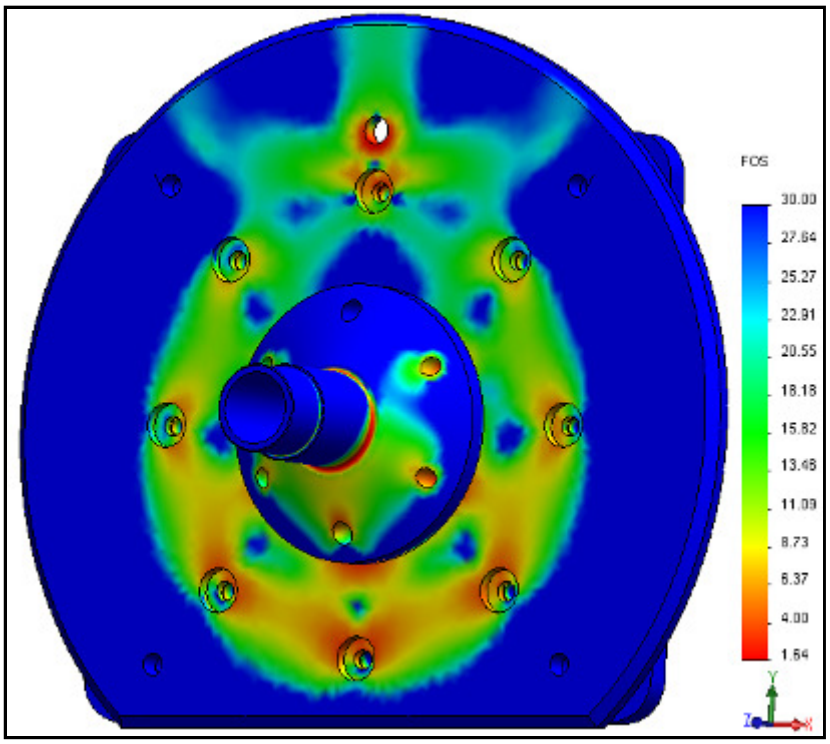

Figure B.15: Hub Lateral FEA - Snout factor of safety distribution

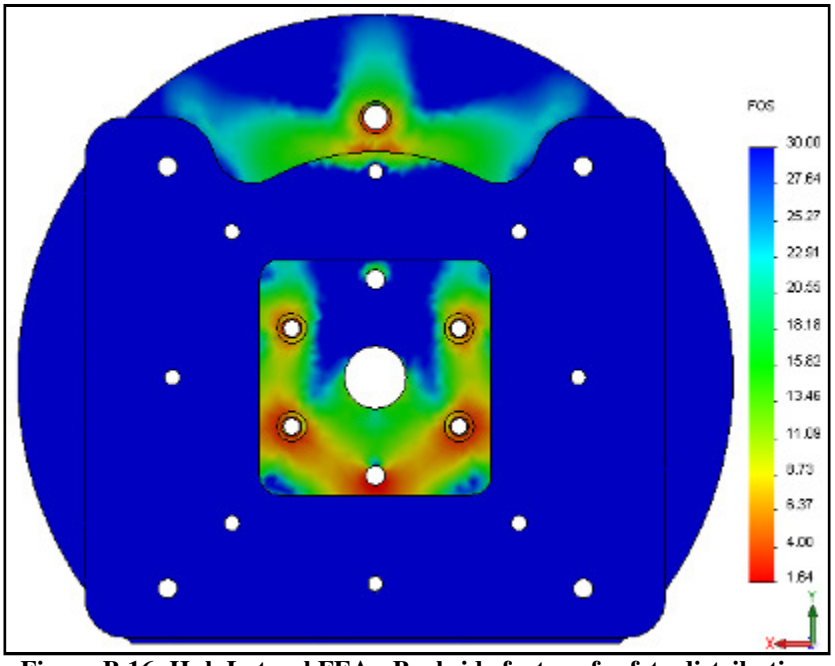

Figure B.16: Hub Lateral FEA - Backside factor of safety distribution

B.1.5.4 Longitudinal Loading Figures

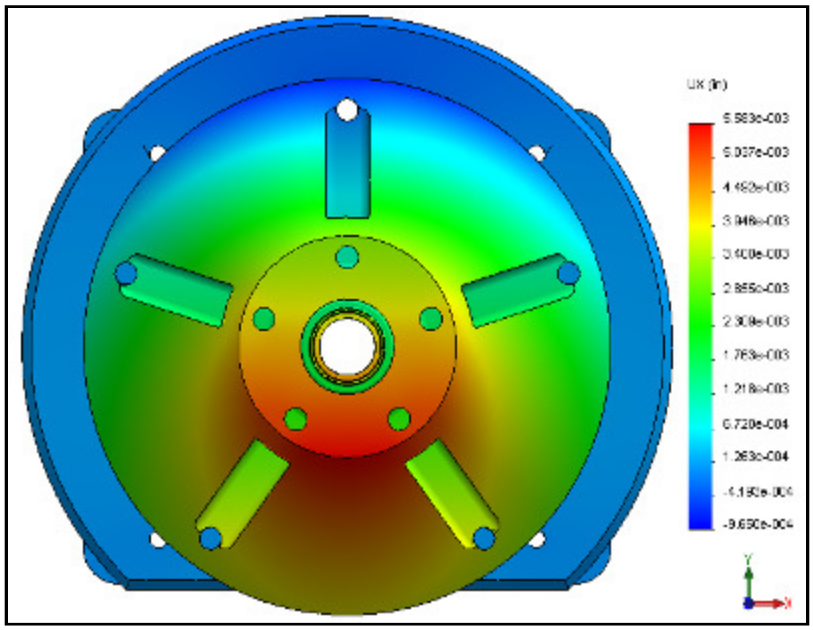

Figure B.17: Hub Longitudinal FEA - Longitudinal displacement

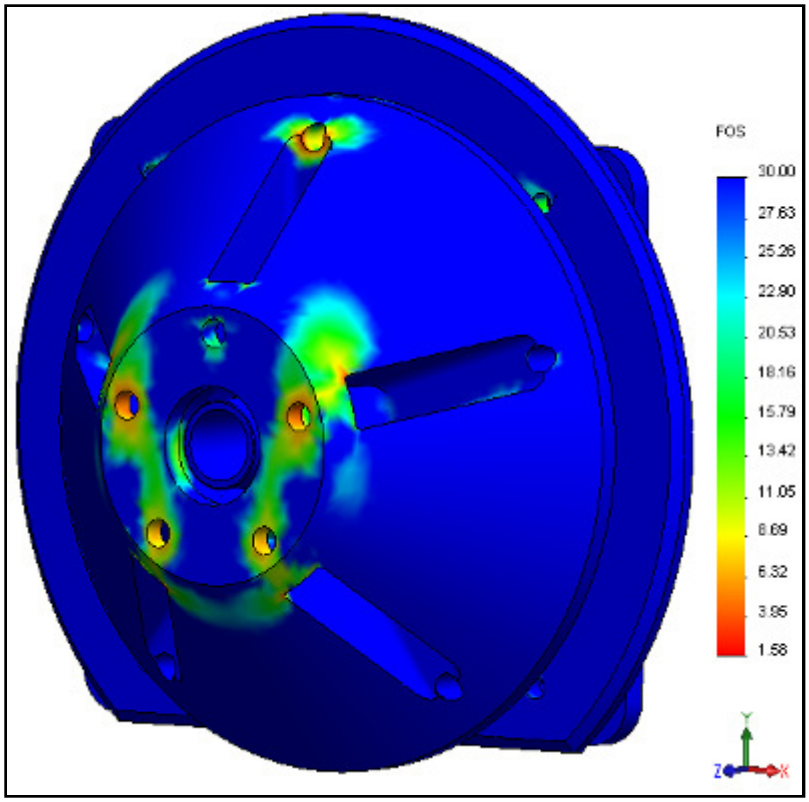

Figure B.18: Hub Longitudinal FEA - Hub factor of safety distribution

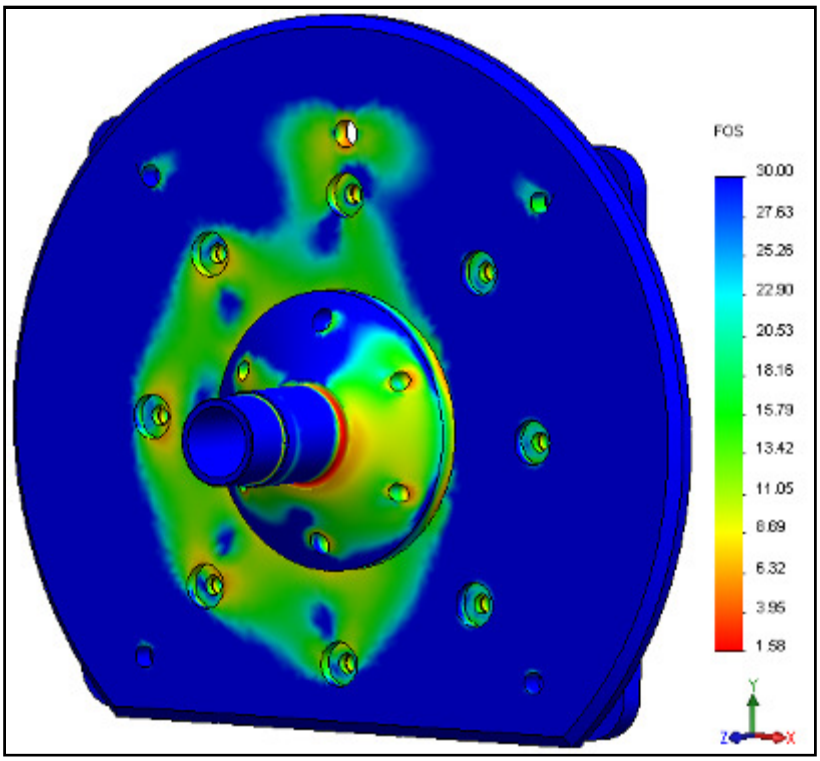

Figure B.19: Hub Longitudinal FEA - Snout factor of safety distribution

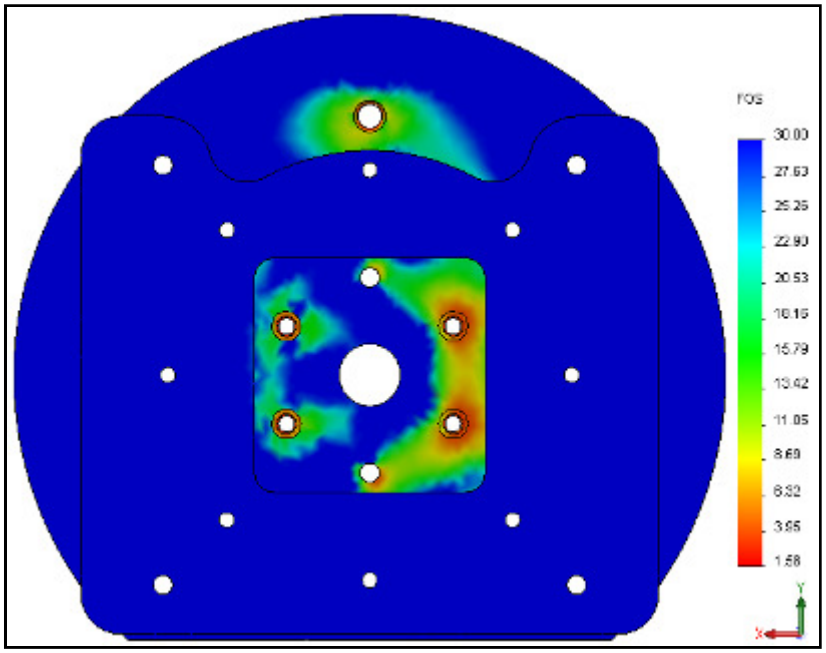

Figure B.20: Hub Longitudinal FEA - Backside factor of safety distribution

B.2 Connecting Rod End Mounts

The connecting rod end mounts for the tire test rig frame are analyzed individually using the worst cast loading which these mounts see during loading situations. In this case, each mount is subjected to 3000lbf vertical loading in order to check displacement and factor of safety results. This loading condition is applied at the pin holes of the mount using a bearing load. Both mounts are made from 4130 steel normalized at 870°C and are constrained using a grounded bolt into a virtual wall which is used to simulate the floor or static I-beam to which they attach. The part mesh element size is 0.0987in and tolerance of 0.0049in with mesh controls of half of these mesh conditions applied around bolt/pin holes.

B.2.1 Static I-Beam Mount

The static I-beam mount joins the rear connecting rods of the frame to the static I-beam of the K&C rig. Due to space and installation considerations, these mounts are made to be very simple and adjustable in terms of rotation angle in order to account for slight differences in installation of the tire test rig. While a more robust mount would be beneficial in terms of installation stiffness for the test rig, the design of this mount is used in order to aid in installation simplicity at the cost of stiffness. Figure B.21 gives the factor of safety distribution of the mount with the minimum factor of safety of 1.65 existing at the upper edge of the part which resides against the virtual wall constraint imposed by the static I-beam.

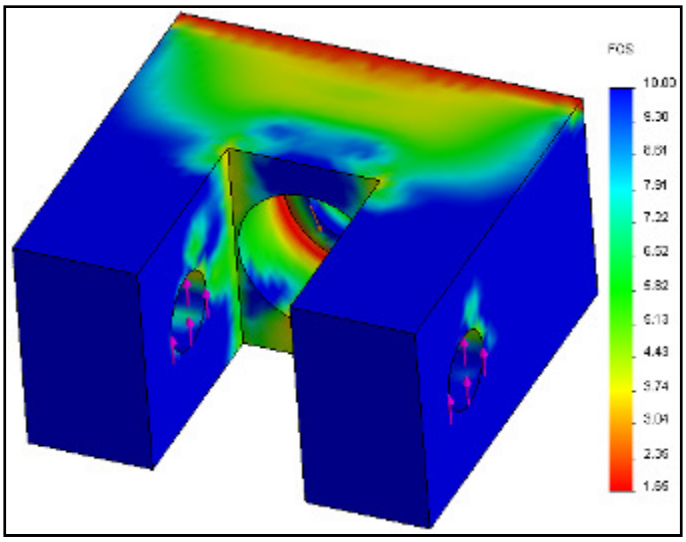

Figure B.21: Static I-Beam Mount FEA – Factor of safety distribution

Figure B.22 shows the resultant displacement which corresponds to this loading condition. These displacement results indicate a component stiffness for the static I-beam mount of around 1420000lb/in.

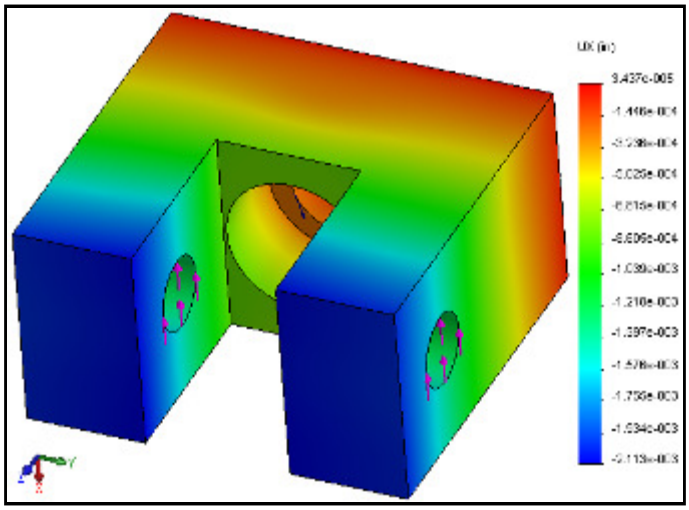

Figure B.22: Static I-Beam Mount FEA – Vertical displacement

B.2.2 Floor Mount

The floor mount joins the front connecting rods of the tire test rig to the concrete floor of the K&C room. These mounts are secured to the ground by four concrete anchor

bolts. For the actual part, center piece of the mount is welded to the floor plate, so a bonded contact connection is used in this FEA. Figure B.23 gives the factor of safety distribution of the mount with the minimum factor of safety 2.25 existing at the edge of the concrete anchor nut.

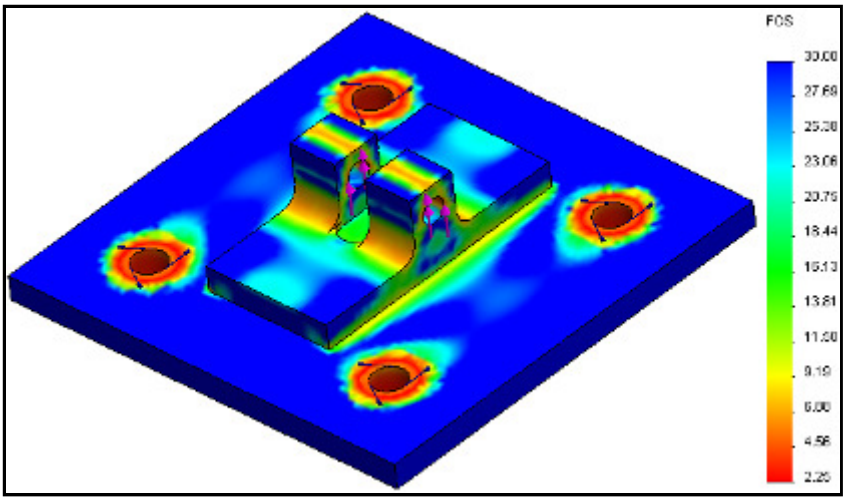

Figure B.23: Floor Mount FEA – Factor of safety distribution

Figure B.24 shows the resultant displacement which corresponds to this loading condition. Displacement results indicate a component stiffness of around 2420000lb/in.

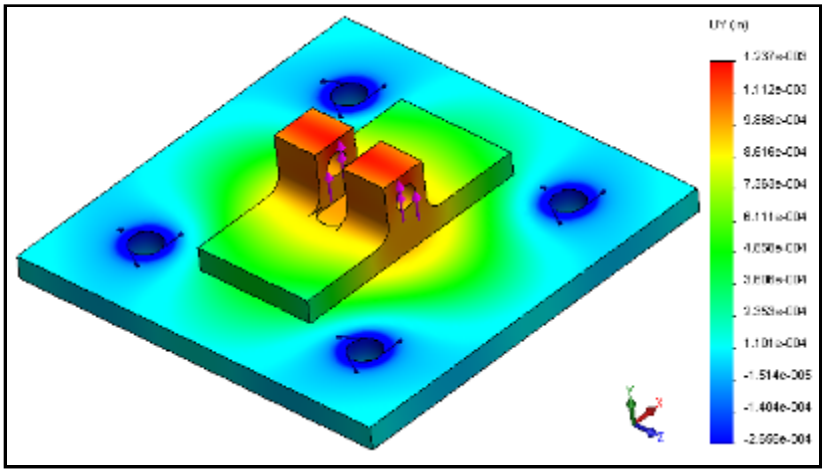

Figure B.24: Floor Mount FEA – Vertical displacement

B.3 Electro-Magnetic Clamp Mount

The electromagnetic clamp mounts are welded onto the frame ends in order to connect the frame to the K&C rig. These mounts are analyzed individually at the maximum force applied to the test rig in each axis. Therefore, the loads applied to these mounts are 6000lbf vertically, 4000lbf laterally, and 5000lbf longitudinally. Laterally and longitudinally, these mounts will take a large amount of the applied force. Vertically, they will not take as much for as the connecting rods will take the majority, but these mount are analyzed at the maximum vertical force just incase. The pieces of this mount are 1020 steel and are welded together. As such, bonded contact sets are used between all the components. The bolt holes on the component terminate in the electromagnetic clamp base in actuality, so in the FEA, these holes are constrained using a Grade 8 grounded bolts into a virtual wall using 80lb-ft as the installation torque. The part mesh element size is 0.1723in and tolerance of 0.0059in with mesh controls of one third these mesh conditions applied around bolt/pin holes. Figure B.25 through Figure B.30 give the FEA displacement and factory of safety distribution results from each axes. These figures show that the electromagnetic clamp mount performs well in each axis with no factor of safety less than 1.48. The maximum stresses occur on the underside of the bolt head and are amplified by the FEA since the mesh is kept reasonably coarse. Even with a coarse mesh, though, the mount is suitable for the test rig loads. The axial displacements indicate a longitudinal stiffness of 2550000lb/in, lateral stiffness of 468000lb/in, and vertical stiffness of 822000lb/in.

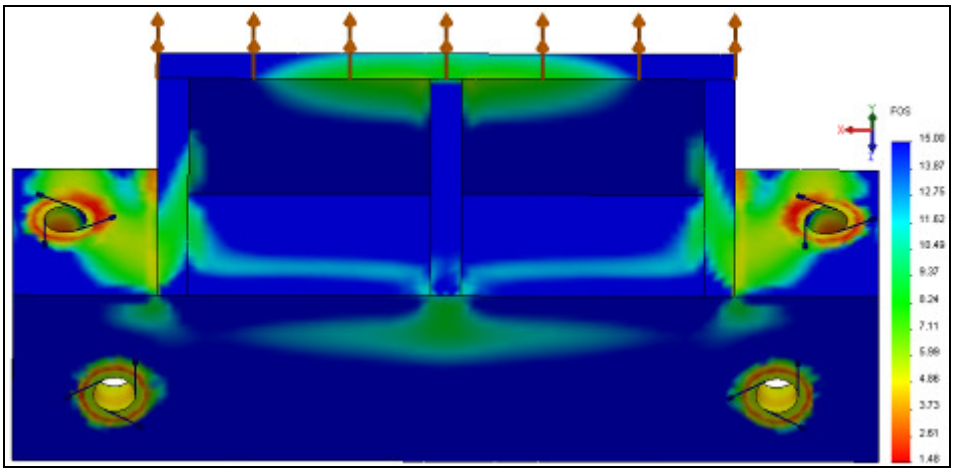

Figure B.25: Floor Mount FEA – Vertical factor of safety distribution

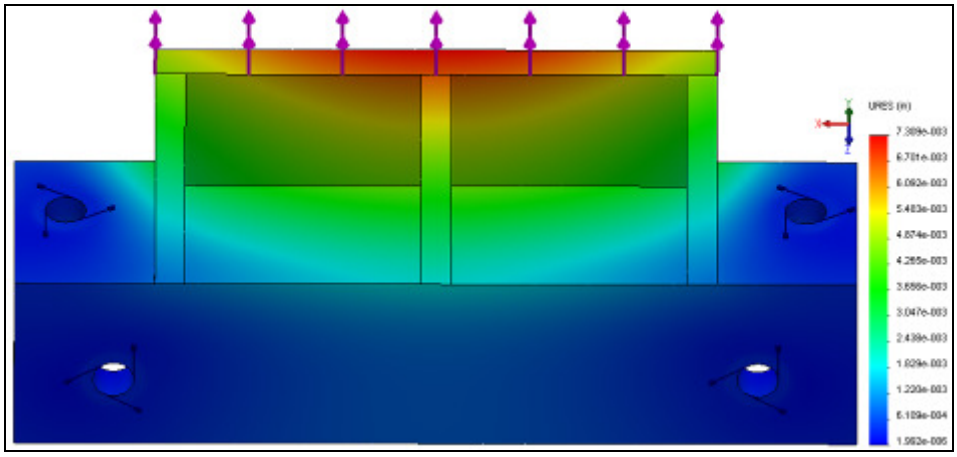

Figure B.26: Electromagnetic Clamp Mounts – Vertical displacement

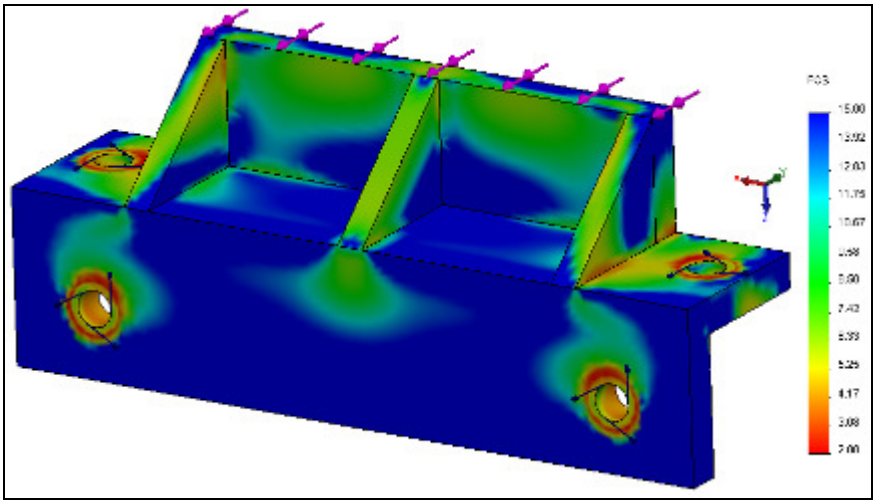

Figure B.27: Electromagnetic Clamp Mounts – Lateral factor of safety distribution

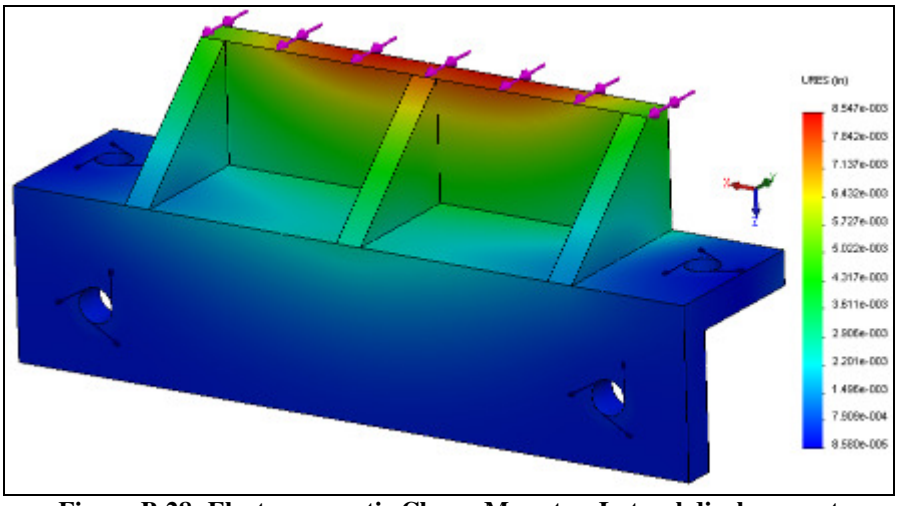

Figure B.28: Electromagnetic Clamp Mounts – Lateral displacement

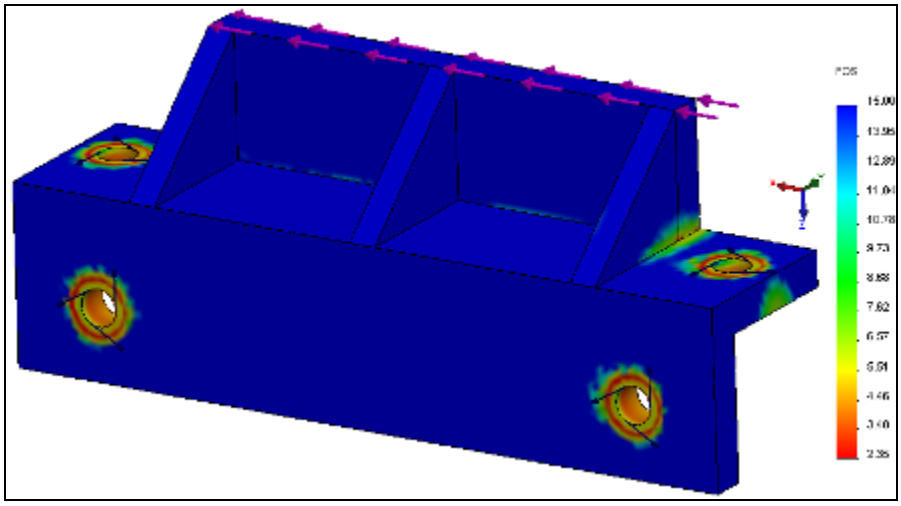

Figure B.29: Electromagnetic Clamp Mounts – Longitudinal factor of safety distribution

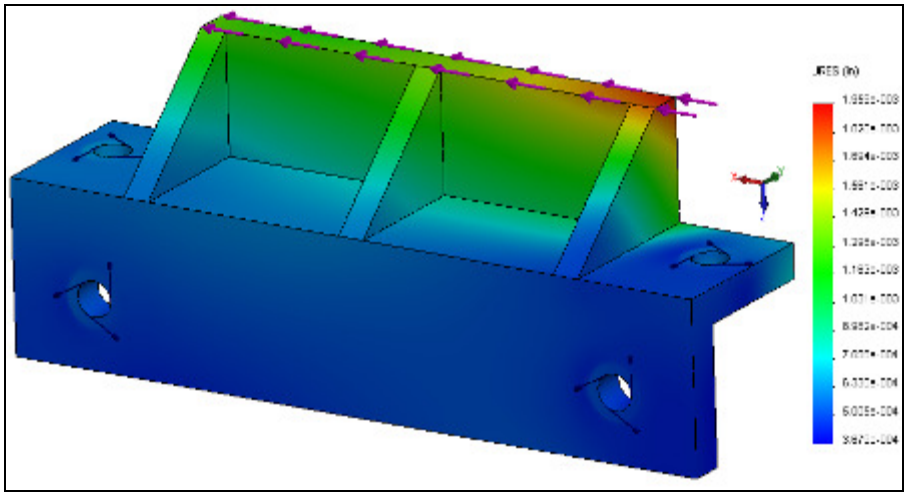

Figure B.30: Electromagnetic Clamp Mounts – Longitudinal displacement

B.4 Component Stiffness Results

The individual component stiffnesses are complied in

Table B.5: Component Stiffnesses

Component	Stiffness [lb/in]		
	Vertical	**Lateral**	**Longitudinal**
Hub Assembly	2400000	364000	893000
K&C Mount	1420000	-	-
Floor Mount	2420000	-	-
Electromagnetic Clamp Mount	822000	468000	2550000

The FEA of the entire test rig frame in Appendix F shows that the test rig including the connecting rods has a vertical stiffness of 310000lb/in, a lateral stiffness of 148000lb/in, and a longitudinal stiffness of 239000lb/in. With the electromagnetic clamp mount not having much bearing on vertical stiffness, the K&C and floor mounts act as spring in parallel which are in series with the test rig frame. The resultant vertical stiffness is then 287000lb/in. The electromagnetic clamp mount acts as a spring in series in lateral and longitudinal loading. Therefore, the effective lateral stiffness is 112000lb/in, and the effective longitudinal stiffness is 219000lb/in. These effective stiffnesses are larger than the test rig design goals.

Appendix C: Bolt and Pin Calculations

The critical bolts and pins which secure the various parts of the static tire spring rate are selected with worst case loading conditions in mind. These component selections are then verified to pass test loading conditions in an FEA study of the test rig. This section aims to describe the selection of these components. Equation C.1 is used to determine the shear stress on all of the bolts and pins. Factor of safety for the pin or bolt is given by Equation C.2. The term σ_{yield} is the tensile yield strength of the material whereas the .6 is a commonly accepted multiplication factor used to convert tensile strength to shear strength for steel (13). Equation C.3 combines Equations C.1 and C.2 such that the necessary bolt or pin diameter is solved for directly. Note that Equations C.1 and C.3 are for single shear, and the 4 becomes a 2 for double shear.

$$\tau_{bolt/pin} = \frac{4F}{\pi * d^{2}_{pin/bolt}} \quad \textbf{C.1}$$

$$F.O.S = \frac{\tau_{bolt/pin}}{\sigma_{yield} * .6} \quad \textbf{C.2}$$

$$d_{bolt/pin} = \sqrt{\frac{4F}{\pi * F.O.S * .6 * \sigma_{yield}}} \quad \textbf{C.3}$$

C.1 Connecting Rod Pins

The pins joining the connecting rods to their mounting points, shown in Figure C.1, are sized to accept the worst case shear loading possible, which is 6000lbf. In this loading scenario, one connecting rod is accepting all of the loading force applied to the test rig. The tensile yield strength of 1020 cold-rolled steel is 50800psi (14). Using a factor of safety of 1.2 for this double shear connection, Equation C.3 is used to solve for a

necessary pin diameter of .323inches. Therefore, a .375inch diameter solid clevis pin is used, McMaster-Carr part number 97245A337.

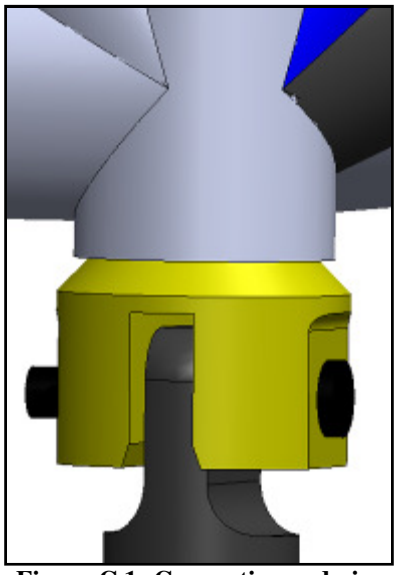

Figure C.1: Connecting rod pin

C.2 Expanding Diameter Pin

The expanding diameter pin which is used to secure the hub is sized to deal with the worst case loading seen at this location shown in Figure C.2. This worst case loading scenario originates from the shear force that is generated when 5000lbf of longitudinal force is applied at a point 13.75inches from the center of the hub plate. The expanding diameter pin is located at a distance of 6.625inches from the center of the plate, and therefore, the pin sees 10377lbf of shear loading. A .625 inch diameter expanding diameter pin from Carr Lane, part number CL-10-EXPH-1.00, has a double shear strength of 25,100lbf (9). This double shear strength for a .625inch diameter pin yields a single shear stress limit of 40907psi. Using Equation C.1, the expanding diameter pin at this location experiences a shear stress of 33824psi. The resultant factor of safety is 1.2. FEA results indicate that the worst loading this expanding diameter pin actually sees in

8250lbf which results in a factor of safety of 1.5. This low margin of safety is used in order to implement the smallest diameter expanding pin possible such that the size of the gearbox that is used to tighten it can be minimized to fit inside of the frame.

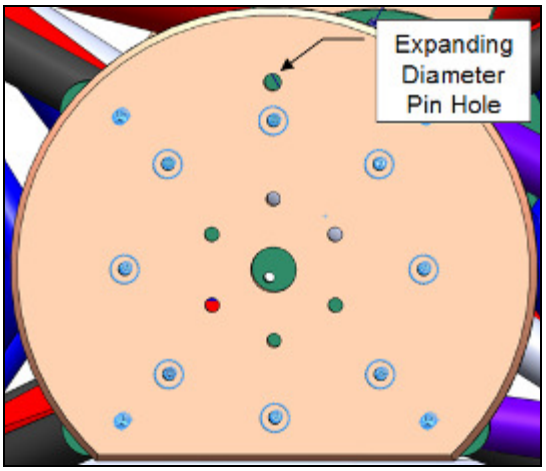

Figure C.2: Expanding diameter pin hole

C.3 Hub Plate/Frame Flange Bolts and Pins

Figure C.3 illustrates the bolts and pins which connect the hub plate to the frame flange.

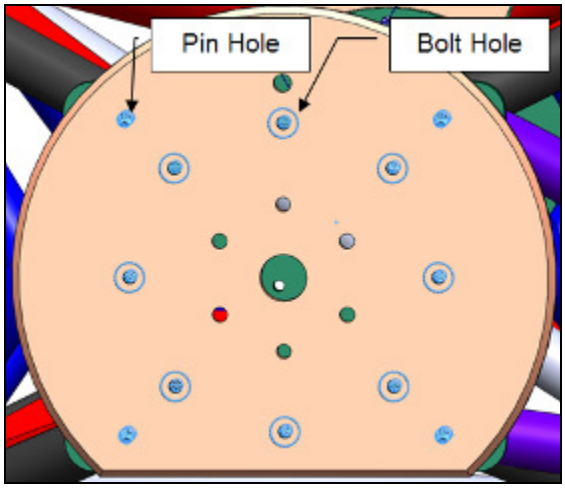

Figure C.3: Bolts and pins connecting hub plate to frame flange

A combination of bolts and pins are used to satisfy different design purposes. The use of pins to connect the two members ensures that no movement exists between these two parts during testing whereas the bolts reduce deflection in the hub plate the span between the hub snout mounting bolts, the inner bolt circle, and the pins. The sizing of these bolts and pins is done with the worst case loading in mind which they could encounter. This loading scenario is the shear force which is generated when 5000lbf of longitudinal force is applied at a point 13.875inches from the center of the hub plate. The pins are placed at a distance of 7.5inches from the center of the plate whereas the bolts are placed at a distance of 5.25inches. The shear forces that are exerted on the pins and bolts at these locations are around 9167lbf and 13095lbf, respectively. The pin is selected by using Equation C.1 to determine that the shear stress on one .5inch diameter pin is 46687psi. With a pin at each of the four corners of the plate, this shear stress reduces to 11672psi per pin. The shear strength of McMaster-Carr part number 97352A330 is 129870psi which yields a factor of safety of 11 per pin using Equation C.2. These pins are oversized such that if one pin takes all of the loading, it still exhibits a factor of safety of 2.75.

Grade 8 bolts are used on the test rig in critical locations, and Grade 8 bolts have a tensile strength of 150ksi (15). Therefore, these bolts have a shear strength of 90000psi. One Grade 8 7/16-20 bolt with a minor diameter of .375inches is subjected to 118560psi of shear stress. Using 8 of these bolts to take up the span area, though, reduces this shear stress to 14820psi per bolt which yields a factor of safety of 6 per bolt. The sizing of these bolts is mainly done to provide large clamping loads between the hub plate and the frame flange.

C.4 Hub Snout Pins and Bolts

The hub snout mounts to the center bolt pattern of the hub plate. This center bolt circle is seen in Figure C.4. The pins are positioned at the top and bottom holes in the pattern while the bolts take up the other four locations. The initial sizing of these pins is done with dimensional and part considerations in mind. The pins used on the hub are the same as those used on the extremities of the frame flange plate while the bolts are selected to be the largest bolts which fit in the design area of the thrust bearing holder face on the backside of the hub plate.

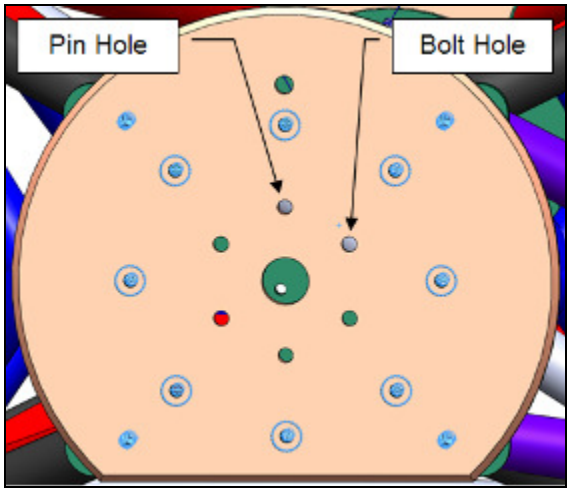

Figure C.4: Bolts and pins connecting hub snout to hub plate

The loads on these bolts and pins are identified through FEA because their worst case loading is not immediately apparent since the load path from the tire to the hub is through the wheel studs, through the hub, and resisted by the expanding diameter pin. The hub rides on the bearings which are pressed onto the hub snout. Therefore, in order to get a worst case loading, the bearings are treated as rigid connections in the FEA which generates a worst case shear loading of 6000lbf on each bolt and pin.

The shear strength of the pin, McMaster-Carr part number 97352A330 is 129870psi which yields a factor of safety of 4.25 per pin using Equation C.2. The bolts that are used to secure the hub snout tot the hub plate are ½ inch diameter, McMaster part number 92220A261, with a shear stress limit of 90000psi and a minor diameter of .40in. The shear stress on these bolts at 6000lbf is 47746psi which gives a factor of safety of 1.8 for each bolt.

Appendix D: Indexing Gear Train

The design requirements of the static tire test rig dictate that the entire assembly must be automated. To fulfill this requirement, one of the areas to address is the indexing of the wheel and tire assembly in order to avoid testing the tire on a belt splice. Figure D.1 labels the designed wheel and tire assembly area on the tire test rig.

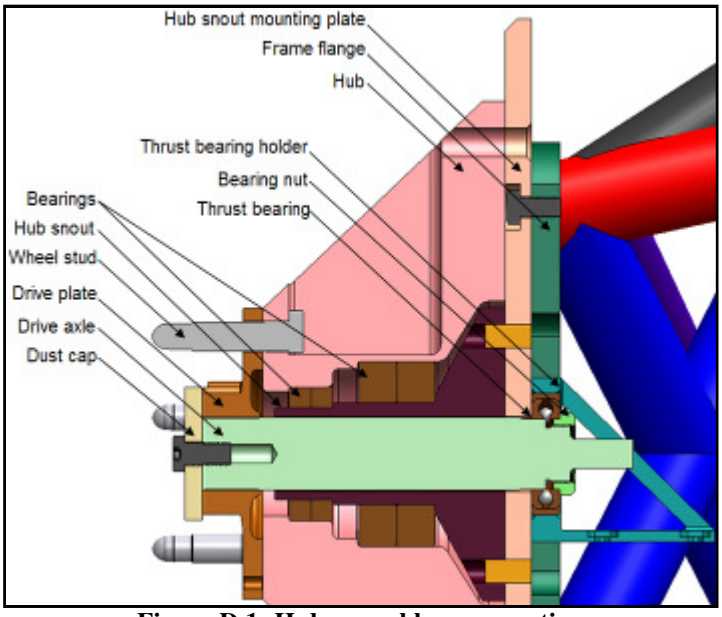

Figure D.1: Hub assembly cross section

Packaging considerations dictate that the motor which is used to rotate this assembly be mounted vertically. In order to accomplish this task, a 1:1 right angle gearbox from Tolomatic, part number 0122-0400, is mounted to the end of the drive shaft. The DC motor is selected by specifying that the desired acceleration output of the hub be from zero to one rpm in one second with a Solidworks-provided moment of inertia for the hub being .76Nm^2. Specifying a factor of safety of 3 on the moment of inertia to account for the unknown resistances of the right angle gearbox, bearing stiction, and wheel and tire inertia yields a required torque of .2in-lb. The DC motor which is

selected for this task is the Groschopp PM 6013 1010 motor. This motor is selected because it is the smallest 12 volt motor that is manufactured by same company as the motor used in the expanding diameter pin gearbox. The performance chart for this motor is shown in Figure D.2.

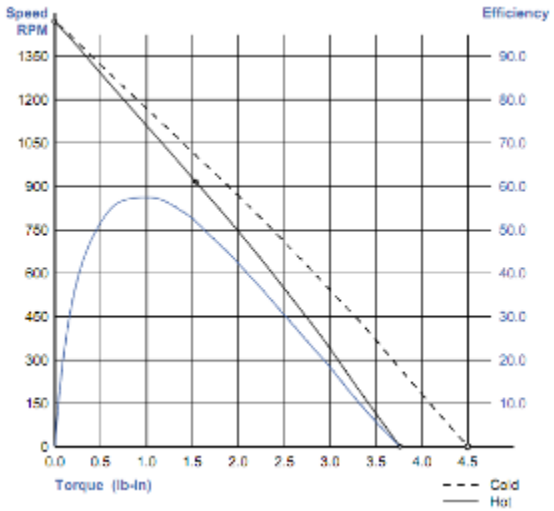

Figure D.2: Groschopp PM 6013 1010 12v DC motor performance chart

While this motor is oversized for the application, the performance of the motor is scaled by reducing the magnitude of current supplied. The packaging of this motor and right angle gearbox is shown in Figure D.3.

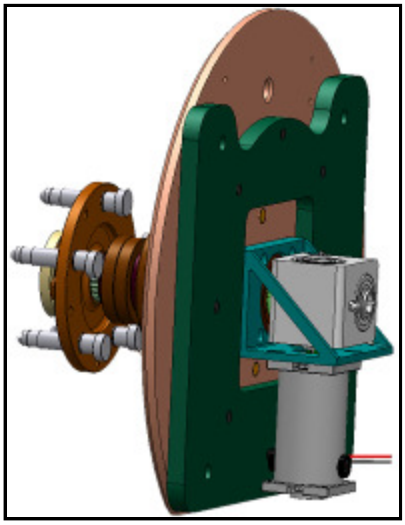

Figure D.3: Groschopp PM6013 motor packaging

Unfortunately, this design did not work in practice due to the large resistance that is supplied by preloaded bearings. In order to overcome this resistance, a gearbox is selected to attach to the head of the motor. The torque multiplication of the gearbox is determined by measuring the amount of weight that is required to turn the assembly. This measurement is performed by hanging weights from the assembled structure and measuring the amount required before rotation begins. Both sides of the test rig are measured and the worst case value is chosen. This value is determined to be 2lb-ft.

The gearbox which is selected is an SDP-SI planetary gearbox, part number A1C8MYS06018, which delivers a gear reduction of 144:1. This gear reduction yields a stall torque output for the DC motor of 45ft-lb with peak rpm being reduced to 6rpm at a torque of 12ft-lb. This gearbox is chosen because it was on closeout from it supplier for a low price and fit within the dimensional constraints of the area. The updated design is shown in Figure D.4.

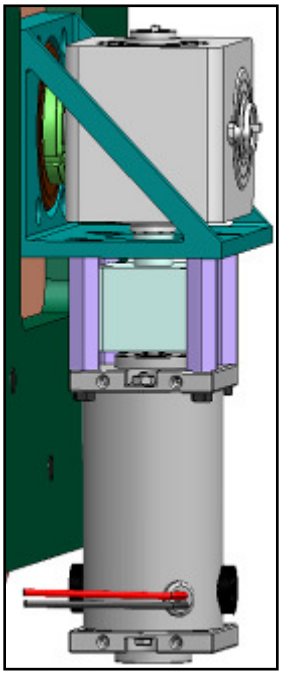

Figure D.4: Final hub indexing component layout

Appendix E: Gearbox Gear Train Design

The function of the gearbox assembly is to automate the repetition of the insertion, tightening, loosening, and removal of an expanding diameter pin during tire indexing operations. An expanding diameter pin is an assembly of male segments separated by female split bushings which expand when drawn together by compression using a center spindle and hex nut. The layout of this expanding diameter pin assembly is shown in Figure E.1.

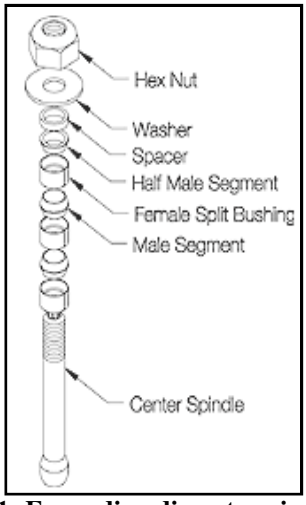

Figure E.1: Expanding diameter pin layout (9)

In order to properly expand this pin, the hex nut must be torqued to 83lbf-ft with the center spindle either being counter-rotated with respect to the hex nut (9). In order to accomplish this, the gear train is designed such that three gears are on one side of the gear box and two on the other with the number of teeth on the three gear side being half those on the two gear side with the pitch remaining constant. An unequal gear train arrangement ensures that the gears concentric with the expanding diameter pin are counter-rotating with respect to one another. Therefore, one gear attaches to the nut of the pin while the other gear drives a hex shaft which connects to the center hex of the pin.

Figure E.2 gives a side view of the gear train layout while Figure E.3 shows a cross section view of the counter-rotating hex shaft.

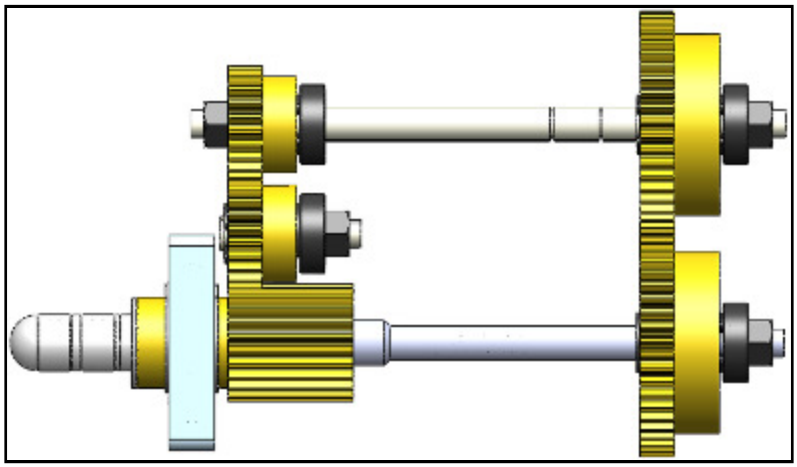

Figure E.2: Gear train layout

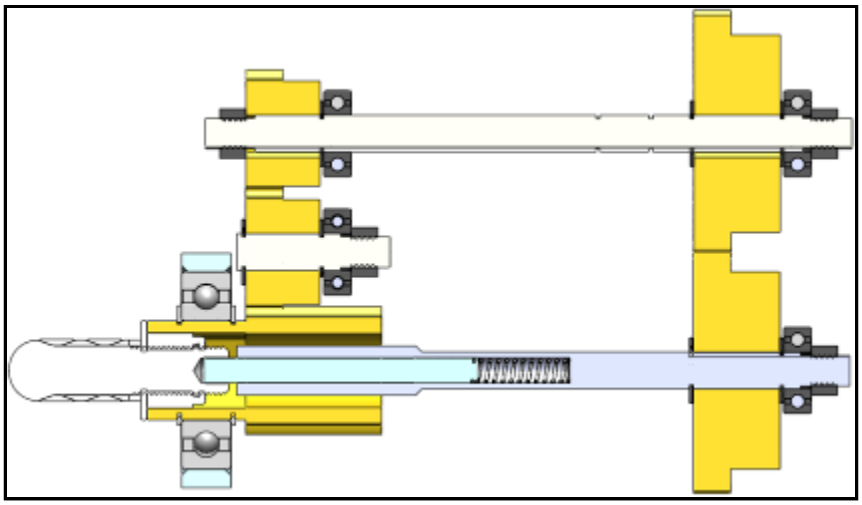

Figure E.3: Gear train layout cross section

The gear train is sized by the smallest gear which possesses enough material in which to cut a hex pattern for the hex nut of the expanding diameter pin. The number of teeth for the respective pitch is doubled in order to size the other side of the gear train. The spur gears which are used in this arrangement are 20 pitch with 24 and 48 teeth. The elongated bottom gear results from needing to actuate the expanding diameter pin one inch into the corresponding index hole on the hub assembly.

Considering that a design goal is to have the entire testing process automated, a motor and gear train must be used to torque down the nut on the expanding diameter pin. With packaging considerations in mind, a worm gear setup and external DC motor are decided upon for the purpose of torquing down the bolt. The worm drive allows precise torquing by means of little backlash and fits compactly within the gearbox. The goal for the worm and motor combination is to select one which requires minimal modification to attach the two components to one other and a maximum size of approximately the same pitch diameter of the 48 tooth spur gear, 2.4in. Also, all of the gearing of the motor must be done between the worm and the worm gear as the rest of the drivetrain is planned to be at a 1:1 ratio from the input to the gear train at the worm gear to the output at the expanding diameter pin. In order to accomplish the worm gear combination which is used is a 80 tooth 2.5in pitch diameter worm gear with a single thread worm. Driving this worm setup is a 12v Groschopp PM 8014 2006 DC motor whose speed, efficiency, and torque are shown in Figure E.4. Speed and torque are regulated by the control system which is used to monitor the automation of the test rig.

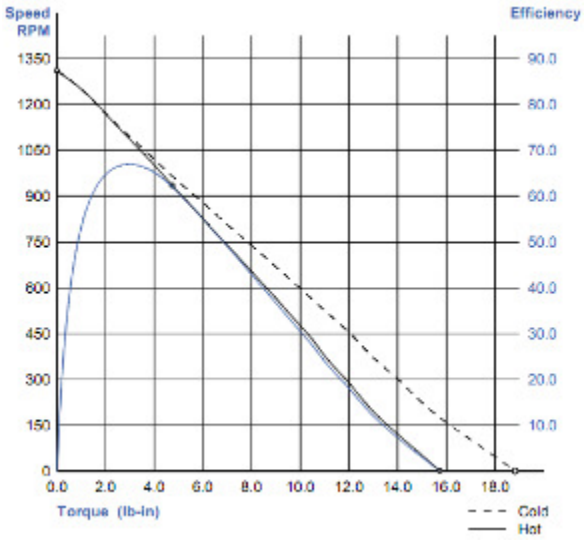

Figure E.4: Gearbox DC motor performance specs

At stall the motor produces roughly 16lb-in of torque, and therefore, this worm gear and motor arrangement is capable of 106lb-ft of torque being transmitted to the expanding diameter pin nut. This motor is oversized in order to apply slightly more torque when loosening the nut on the expanding diameter pin. The layout of the worm gear and worm on the gear train is shown in Figure E.5.

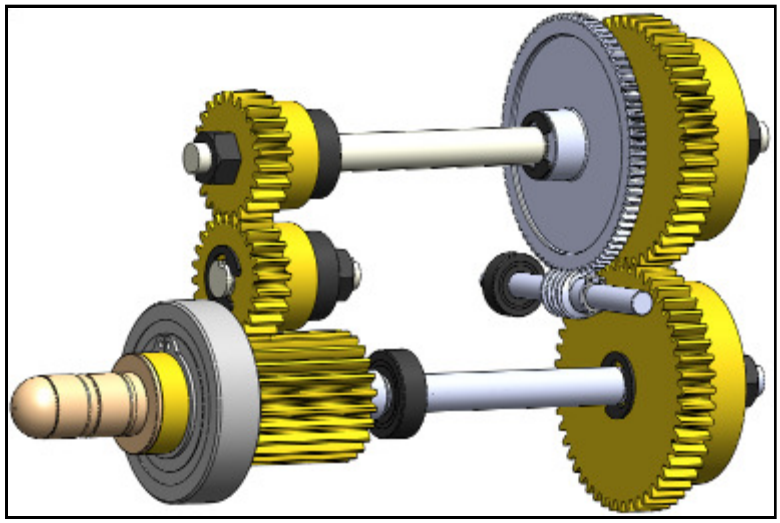

Figure E.5: Worm drive in gear train

The worm shaft is attached to the DC motor output shaft by a polyurethane and metal coupling. The motor and shafts are attached to the frame by mounting plates. These connections are shown in Figure E.6 and Figure E.7. A bill of materials for the gearbox is found in Appendix A.

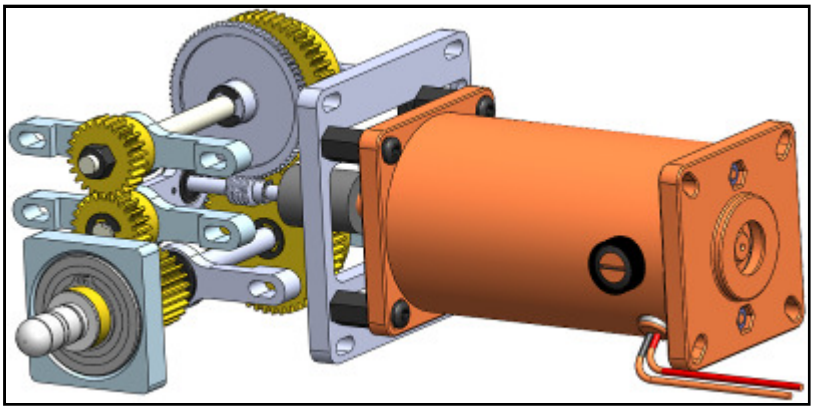

Figure E.6: Gear train with DC motor

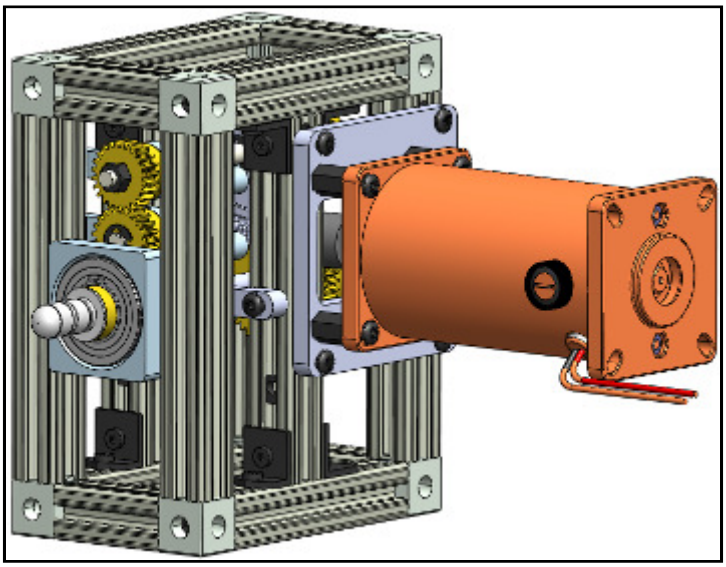

Figure E.7: Gearbox frame with gear train and DC motor

Appendix F: Frame Assembly FEA

F.1 Analysis Purpose

In order to assess the installation stiffness of the test rig, Solidworks Simulation FEA is employed. The goal of this analysis is to determine whether the tire test rig meets the compliance design objectives necessary in this application. These compliance design objectives revolve around making the test rig stiff enough that any measurement error of tire deflection which is incurred by the deflection of the test rig frame does not induce an error more than the tire to tire variation found in the project sponsor's race tires. This tire to tire variation is found to be around 5% (7). The graph of Figure F.1 displays the correlation between test rig spring rate and measurement error for the designed-for tire spring rate values of 5000lb/in vertical, 4000lb/in lateral, and 6000lb/in longitudinal. These spring rate values represent the maximum spring rates encountered for the project sponsor's race tires (8).

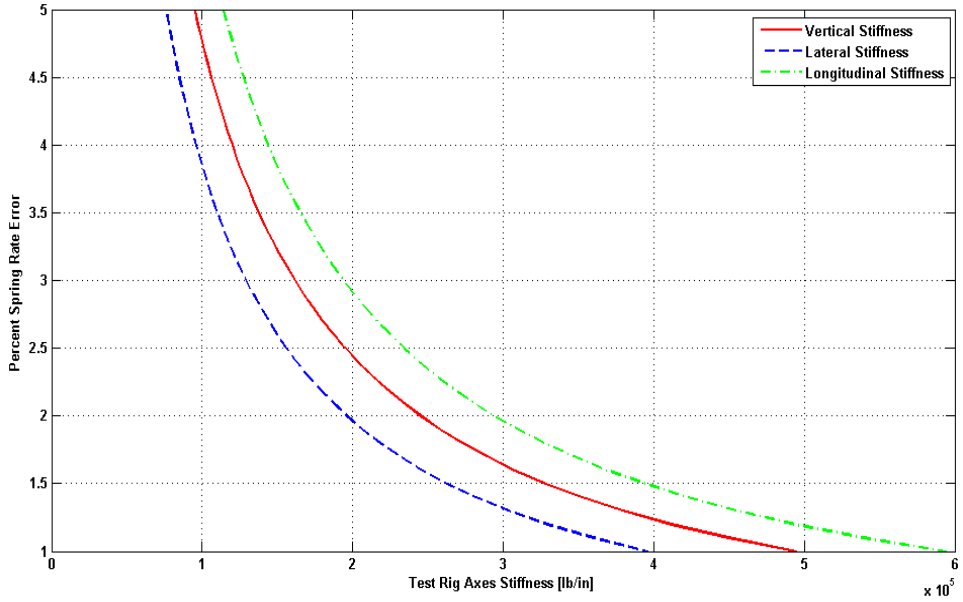

Figure F.1: Stiffness design requirements

Even though compliance errors can be accounted for since the K&C machine measures wheel center as well as elevator pad motion, a stiff test rig is still important. Stiffness is necessary in order to reduce frame fatigue, mitigate any induced camber or toe during testing, and allow for possible repurposing of the test rig for use on another measurement machine where wheel center motion is not tracked.

Table F.1 lists the tire stiffness which is used to calculate the minimum allowable test rig stiffness that achieves an error value of 5%. While a stiffer test rig is more desirable, a diminishing return on reduction of percent error when stiffness is added is illustrated by Figure F.1. Therefore test rig stiffness values which induce error values between five and one percent are the most practical.

Test rig stiffness with respect to camber and toe stiffness is also of design interest. The project sponsor's race cars exhibit an induced camber and toe stiffness of approximately 2000lbf/deg and 1250lbf/deg respectively (10). Therefore, a design objective is to create be an order of magnitude greater than these values.

Table F.1: Test Rig Stiffness Design Goals

Test Axes	Stiffness [lb/in]	Allowable Test Rig Stiffness [lb/in]
Tire -Vertical	5000	≥95000
Tire - Lateral	4000	≥76000
Tire - Longitudinal	6000	≥114000
Camber	2000	≥20000
Toe	1250	≥12500

F.2 Model Layout and Assumptions

The FEA model is shown in Figure F.2 and is a nearly complete test rig assembly with the removal non-structural parts such as the gearbox. Table F.2 lists the components which are included in this model.

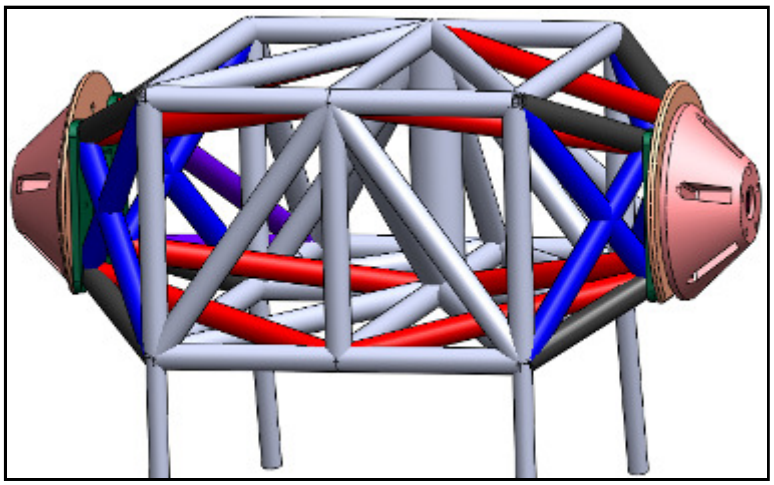

Figure F.2: Frame assembly FEA model

Table F.2: FEA Model Components

Part	Material / Sizing
Frame	• 1020 Steel • All 2" OD x .188 wall tubing with one 4" OD x .25 wall tube
Connecting Rods	• 1020 Steel • 1.5” OD solid rod
Frame Flange	4130 Steel Normalized @ 870°C
Hub Snout Mounting Plate	4130 Steel Normalized @ 870°C
Hub	4130 Steel Normalized @ 870°C
Hub Snout	4130 Steel Normalized @ 870°C

The frame and connecting rod tubing is chosen to be 1020 steel because it is readily available, cheap, replaceable, and easy to machine and weld. The assumption is made that tubing stresses are not going to be an issue since the frame is overbuilt. The 4130 steel which used for non-tubing parts is implemented because it is high strength while remaining machinable and non-exotic. The components which it is used for are subjected to high stresses over a large number of testing cycles.

The tubing in Figure F.2 is not shown as notched because the frame is evaluated as a weldment structure which treats the tubing as 1D beam elements rigidly connected at nodes with continuous profiles. A weldment structure is used because the displacement, forces, and overall factory of safety of the frame layout is the concern, not stresses in the

tube profiles and at tubing junctions. It is understood that the welded frame will not be as stiff as the FEA predicts.

Because it is only possible to connect weldments to solid bodies at nodes, the electro-magnetic mounts are not included in this analysis since they are not welded to the frame entirely at a node. This node connection is valid at the frame flange plate since it is only connected to the frame at tubing junctions. Therefore, the clamp mounts are analyzed by themselves while their mounting area on the frame is treated as fixed during the frame analysis.

Another assumption made in the layout of the model includes treating the pins which join the connecting rods to the frame, the floor, and the static I-beam as rigid. More specifically, the connecting rods are treated as spanning the distance from their floor or static I-beam intersection all the way to their respective connection node at the bottom of frame. This assumption is made because, like the clamp mounts, a solid body such as a pin cannot meshed with a weldment structure unless it connects to a node.

Even though the static I-beam and floor mounting plates do connect to the weldment structure at nodes, they are also excluded from the analysis. Since it is possible to extract forces at nodes from the analysis, these mounts are subjected to component-only FEA using the forces which are obtained from the frame FEA, and their displacements are added to the measured frame displacement. This method is utilized in order to facilitate meshing and keep the model simple.

Another excluded part is the axle which runs though the center of the hub snout. This part is excluded in order to keep the model simple because its addition to the frame

FEA would require the drive plate, bearing cap, indexing assembly bracket, and another bearing, for which no stiffness information is available, to be included in the analysis. Therefore, it is determined the axle should not be a contributing member to the analyzed stiffness of the frame. The frame should meet the design goals without the stiffness of this part included.

F.3 Connections

The frame structure is connected by joints at tubing intersections as seen in Figure F.3, and these joints operate as rigid connections in the analysis.

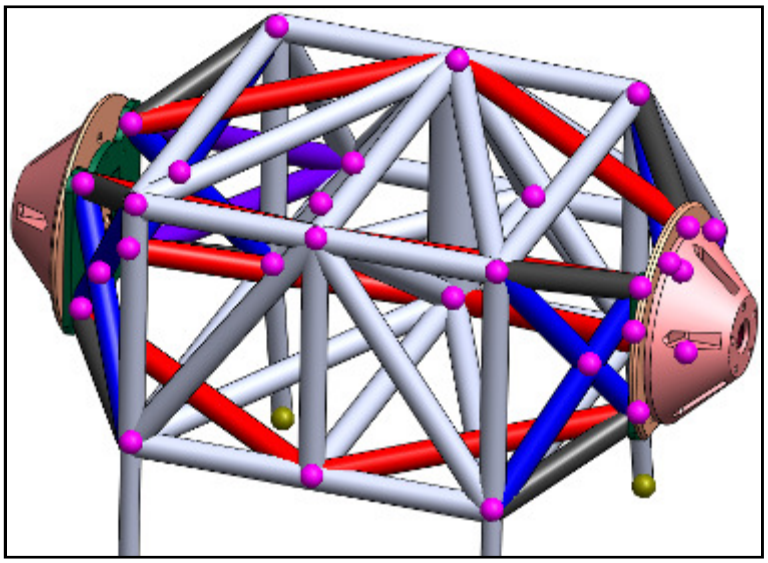

Figure F.3: Frame joints

The joints that join the connecting rods to the floor and static I-beam are set as fixed mounting points as shown in Figure F.4.

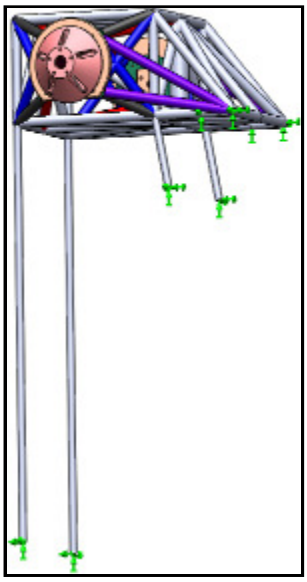

Figure F.4: Fixed Mounts

Also shown in Figure F.4 are the fixed joints of the electro-magnetic clamp mounts. One joint sits at the foremost point of the connection between the clamp mount and the frame and the other sits at the rearmost point.

The frame flange is connected to the tubing structure by using a bonded contact set between the flange and the four tubing joints which reside on its backside. The front side of the frame flange provides the connection points to the hub snout mounting plate. These connections are a series of bolts and pins shown in Figure F.5.

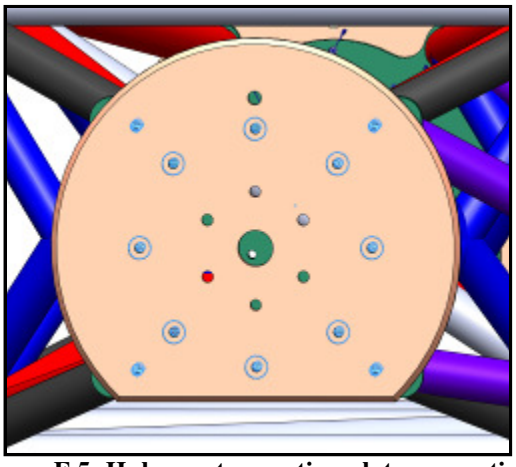

Figure F.5: Hub snout mounting plate connections

The four hole pattern on the outside of the plate is for removable dowel pins. These connections are set as no translation and no rotation pin connections between hub snout mounting plate and the frame flange. The inner bolt circle consists of eight bolt connections. These bolt connections are given the properties of 7/16-20 hex cap screws with 145000psi tensile strength and an axial clamping load of 10000lbf (15,16). Sizing for these bolts is done in 0. The contact set between the frame flange and the hub snout mounting plate is set to no penetration.

The next connection set occurs between the hub snout and the hub snout mounting plate as shown in Figure F.6.

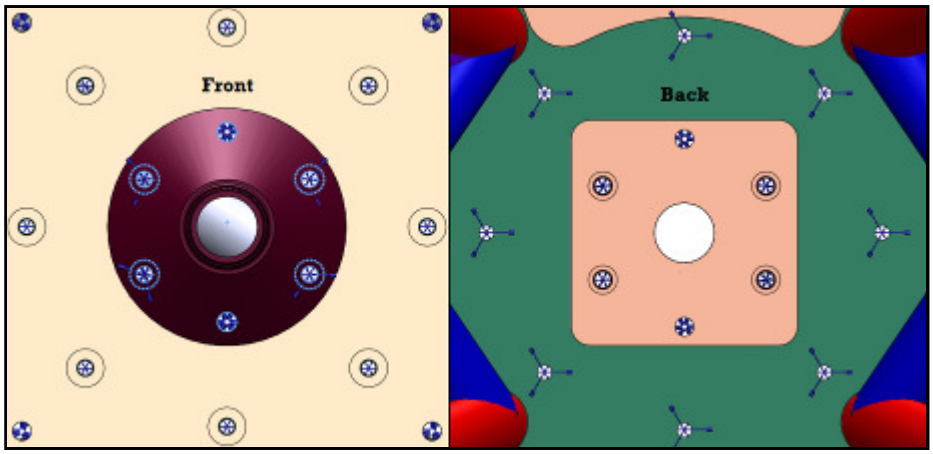

Figure F.6: Hub snout connections

The hub snout is attached with a combination of pins and bolts. The pins are used in order to take up any rotational play which might exist from only using bolts on this piece and are located at the top and bottom of the snout. The pins are set as no translation and no rotation pin connections while the remaining four bolt holes are secured using the same bolt type and properties of those which are used to connect on the hub snout mounting plate to the frame flange. In order to connect the hub to the hub snout, the

bearings are represented as rigid connections as seen in Figure F.7. A rigid connection is used in order to place the hub snout in a worst case loading situation where all of the input forces and moments that are applied at the hub are transmitted to the hub snout and expanding diameter pin connection as shown in Figure F.8. The hub snout and the hub are given a no penetration bonding condition to the hub snout mounting plate.

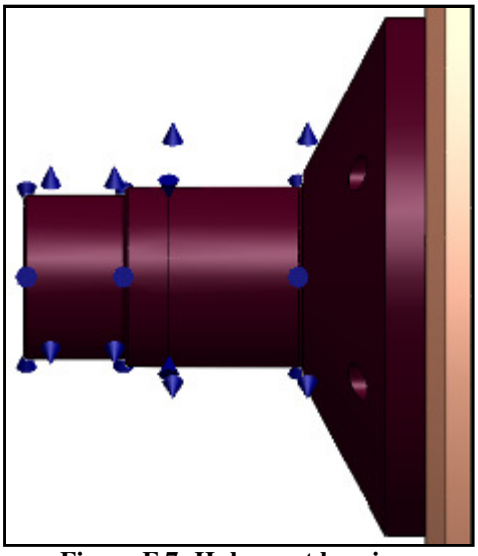

Figure F.7: Hub snout bearings

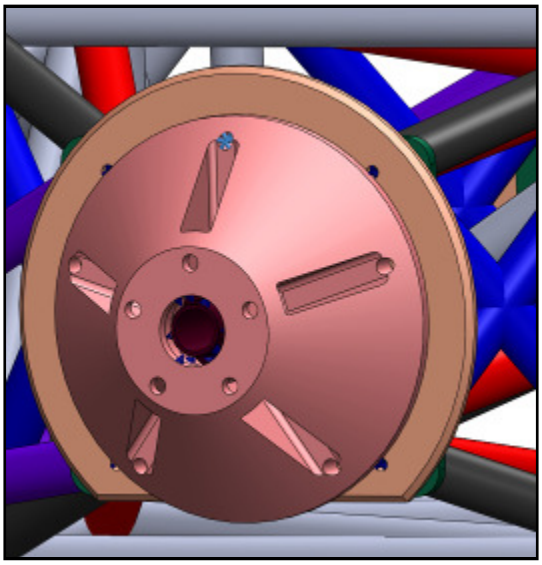

Figure F.8: Expanding diameter pin

F.4 Loads

The loads which are used in the FEA are set by the test range to which the rig is expected to be subjected. The load is applied as a remote point load in plane with the contact face between the wheel and the hub at the contact patch of the project sponsor's nominal race tire, which yields a hub center to contact patch radius of 13.875in. Table F.3 gives the forces applied and their corresponding moments in the SAE coordinate system.

Table F.3: Hub FEA Loading Conditions

Axes	Force [lbf]	Load Location
Vertical (Z)	-6000	Wheel stud holes
Lateral (Y)	±4000	Face of wheel stud holes
Longitudinal (X)	±5000	Wheel stud holes

Figure F.9 through Figure F.11 illustrate these loads and locations on the hub with the frame structure hidden. While these locations are not entirely realistic representations of how the loads applied to the tire are transferred to the hub, they provide a reasonable approximation.

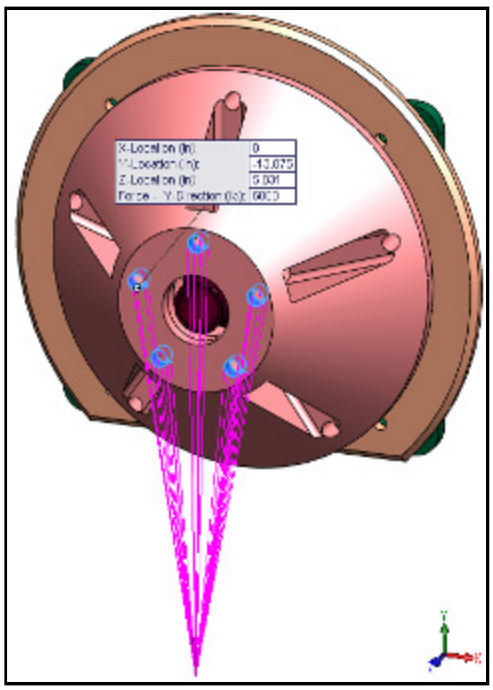

Figure F.9: Hub vertical loading

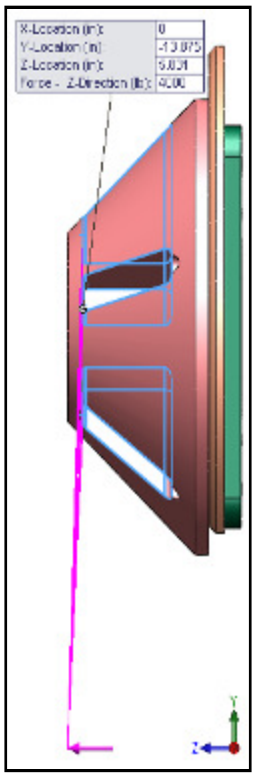

Figure F.10: Hub lateral loading

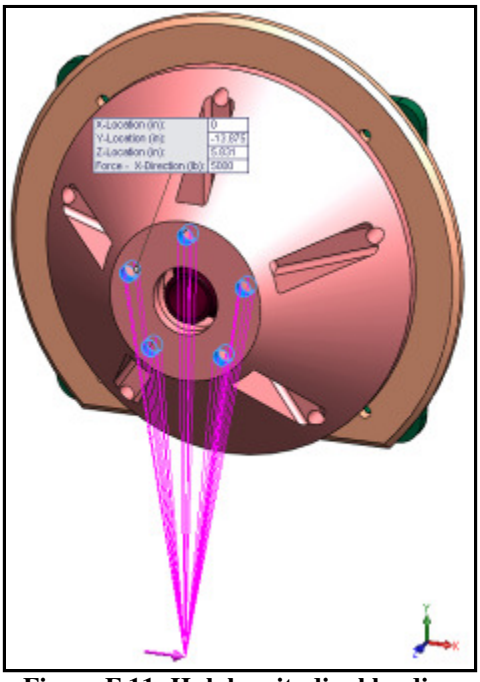

Figure F.11: Hub longitudinal loading

These loads are applied only to one hub side of the test rig while the other side is left unconstrained. This arrangement ensures that the test rig is analyzed in a near worst

case scenario. In actual testing conditions, a wheel and tire assembly is mounted on the non-tested side of the rig and preloaded.

F.5 Mesh

SolidWorks' beam element to solid element meshing is an exceedingly finicky tool. The mesh controls are adjusted with little regard to analyzing minute stress regions and are instead adjusted simply to allow the structure to mesh properly. Stresses are of a secondary concern as component displacement is of more interest in this assembly FEA. FEA for individual components is run to analyze stresses, as found in Appendix B. Mesh controls are applied around holes in order to more accurately capture forces on the bolts and pins in these areas. High quality meshing is not possible with this mixed meshing between solid and beam elements so mesh controls are adjusted from fine back to coarser settings until the model is able to mesh successfully. Figure F.12 through Figure F.15 show the assembly mesh results.

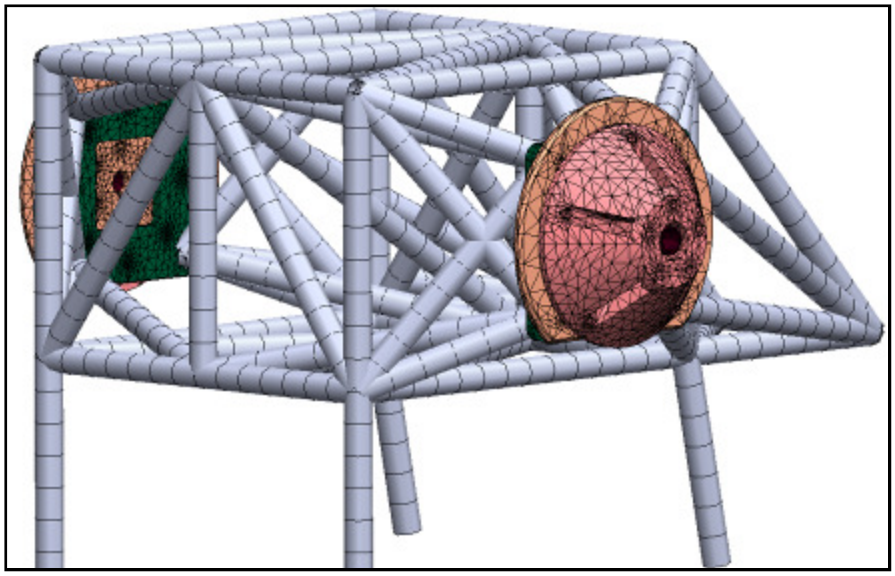

Figure F.12: Overall assembly mesh

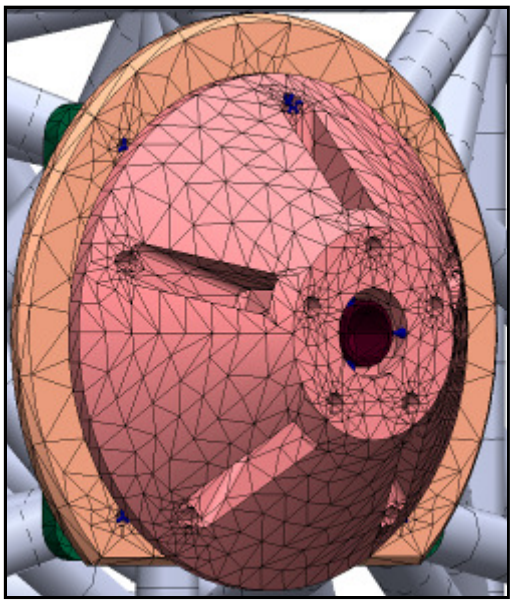

Figure F.13: Assembly mesh – hub

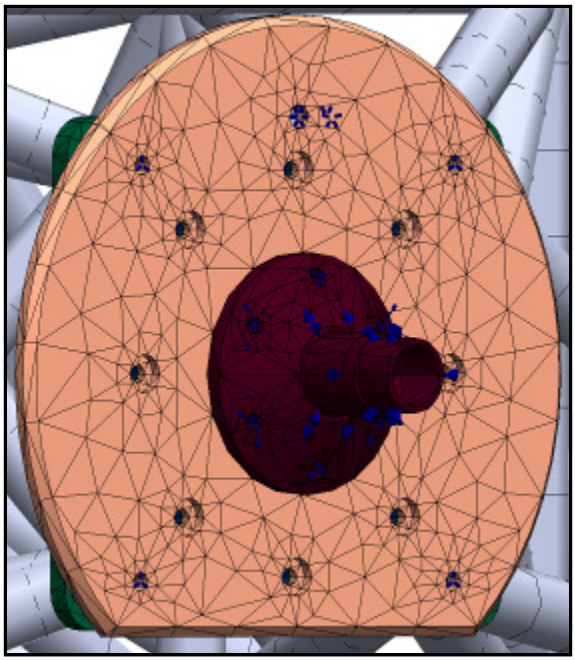

Figure F.14: Assembly mesh – hub snout and mounting plate

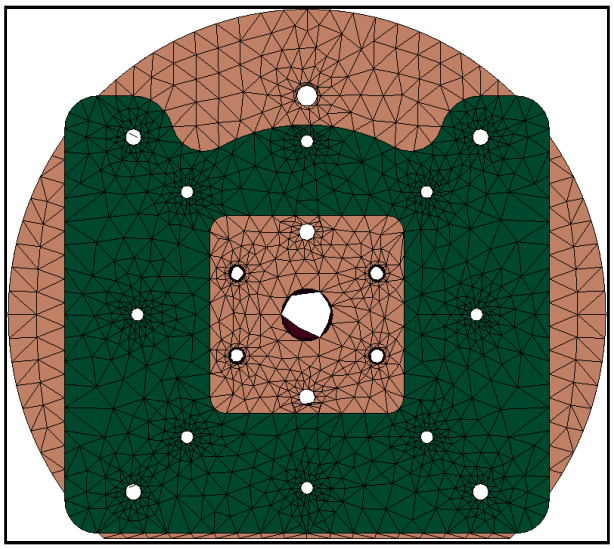

Figure F.15: Assembly mesh – frame flange

F.6 Results

The stiffness of the test rig is evaluated in two planes, the backside of the frame flange and interfacing surface between the hub and the wheel center, with four points on each. These two locations are evaluated in order to see the difference between the compliance allowed by the frame and that allowed by the frame plus the wheel and tire assembly mounting components. Figure F.16 illustrates the location of these points.

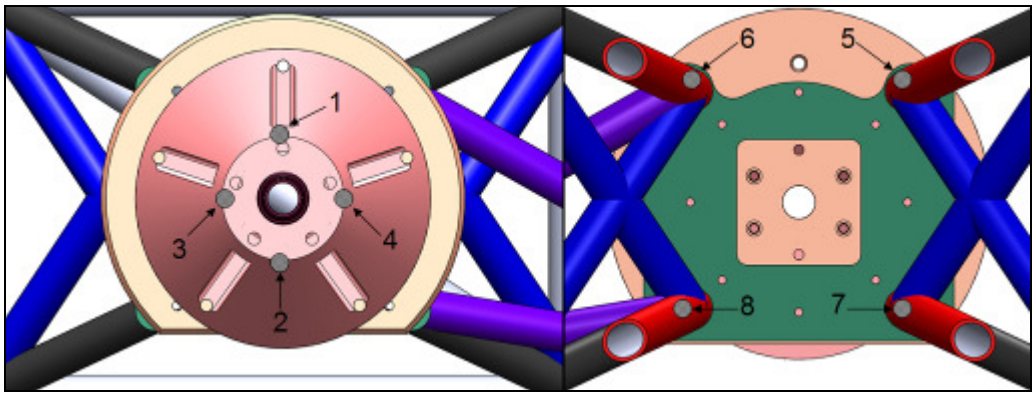

Figure F.16: Displacement Measurement Points

Points 1-4 are located on the edges of the face of the hub plate while points 5-8 are found at the intersection of the support tubing and the frame flange. The coordinate

system for the test rig originates at the center of the frame tubing structure. Therefore, it sits along the hub snout centerline in the center of the frame tubing. Looking at the page, the Y-axis is positive up, the Z-axis is positive left, and the X-axis is positive coming out of the page. The coordinates of the measurement points are provided in Table F.4, and these points are used to calculate the rotation of the hub and frame flange in camber and toe. These coordinates combined with the measured displacements from the FEA results, Table F.5 through Table F.7, are used to evaluate the stiffness of the rig in its three loading aces as well as camber and toe stiffness.

Table F.4: Measurement Point Coordinates

Point	X- Coordinate [in]	Y-Coordinate [in]	Z-Coordinate [in]
1	28.833	3.100	0
2	28.833	-3.100	0
3	28.833	0	3.100
4	28.833	0	-3.100
5	22.077	6.103	4.841
6	22.077	6.108	-4.835
7	22.077	-4.692	4.447
8	22.077	-4.420	-4.430

Table F.5: Vertical (Y-Axis) Loading FEA Results

Point	X Displacement [in]	Y Displacement [in]	Z Displacement [in]
1	-0.0030	0.0189	-0.0035
2	0.0088	0.0189	-0.0026
3	0.0030	0.0193	-0.0030
4	0.0024	0.0184	-0.0031
5	-0.0031	0.0084	-0.0034
6	-0.0026	0.0069	-0.0039
7	0.0046	0.0087	-0.0022
8	0.0029	0.0074	-0.0017

Table F.6: Lateral (X-Axis) Loading FEA Results

Point	X Displacement [in]	Y Displacement [in]	Z Displacement [in]
1	0.0065	0.0195	-0.0071
2	0.0271	0.0194	-0.0068
3	0.0182	0.0196	-0.0069
4	0.0151	0.0193	-0.0069
5	0.0079	0.0020	-0.0045
6	0.0040	0.0017	-0.0048
7	0.0159	0.0030	-0.0047
8	0.0114	0.0027	-0.0034

Table F.7: Longitudinal (Z-Axis) Loading FEA Results

Point	X Displacement [in]	Y Displacement [in]	Z Displacement [in]
1	0.0079	0.0014	-0.0158
2	0.0090	0.0014	-0.0210
3	0.0150	-0.0013	-0.0188
4	-0.0013	-0.0014	-0.0182
5	0.0127	-0.0018	-0.0023
6	0.0006	0.0026	-0.0023
7	0.0099	-0.0010	-0.0070
8	0.0047	0.0021	-0.0064

Table F.5 and Table F.9 give the resultant stiffness values that are obtained from the FEA point displacement data. The stiffness values of the frame are approximately double those of the hub face, but the stiffness values at the hub exceed the design objectives set for the project as found in Table F.1. Therefore the main test rig frame assembly design is suitable for the project. Figure F.17 through Figure F.19 illustrate the displacement results from the FEA. The frame tubing exhibits a factor of safety much greater than 2 in all loading conditions while the performance of the hub assembly parts is further analyzed in Appendix B.

Table F.8: Stiffness Results @ Hub

	Vertical Loading	Lateral Loading	Longitudinal Loading
Vertical Stiffness [lb/in]	310398	204603	3513703
Lateral Stiffness [lb/in]	683838	147765	332667
Longitudinal Stiffness [lb/in]	1708428	560695	238663
Camber Stiffness [lb/deg]	55045	21052	454545
Toe Stiffness [lb/deg]	1000000	142857	39682

Table F.9: Stiffness Results @ Frame

	Vertical Loading	Lateral Loading	Longitudinal Loading
Vertical Stiffness [lb/in]	688626	1335113	1928268
Lateral Stiffness [lb/in]	1305199	251889	394944
Longitudinal Stiffness [lb/in]	1545595	840336	716845
Camber Stiffness [lb/deg]	169787	96677	1332979
Toe Stiffness [lb/deg]	1481052	154397	95341

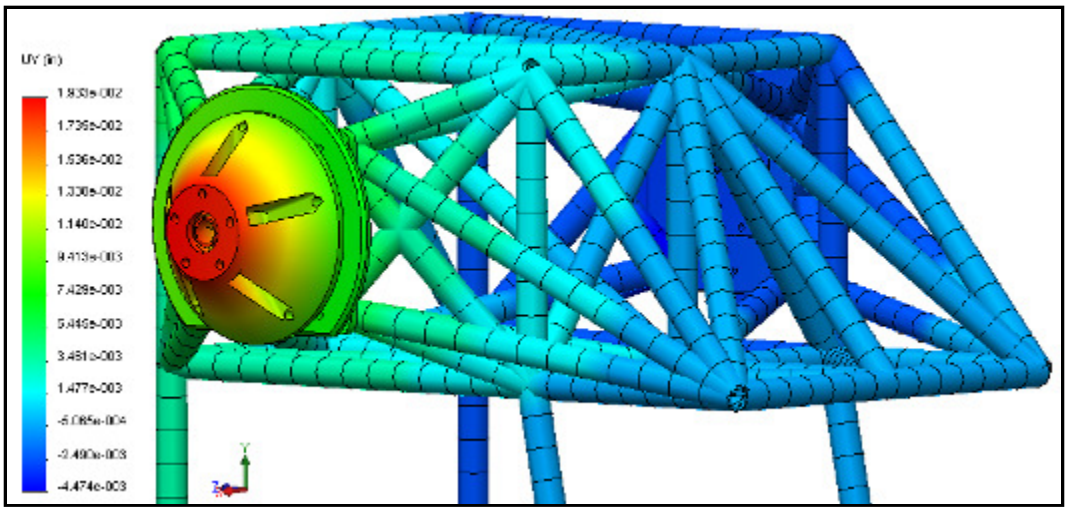

Figure F.17: Frame vertical displacement from vertical loading

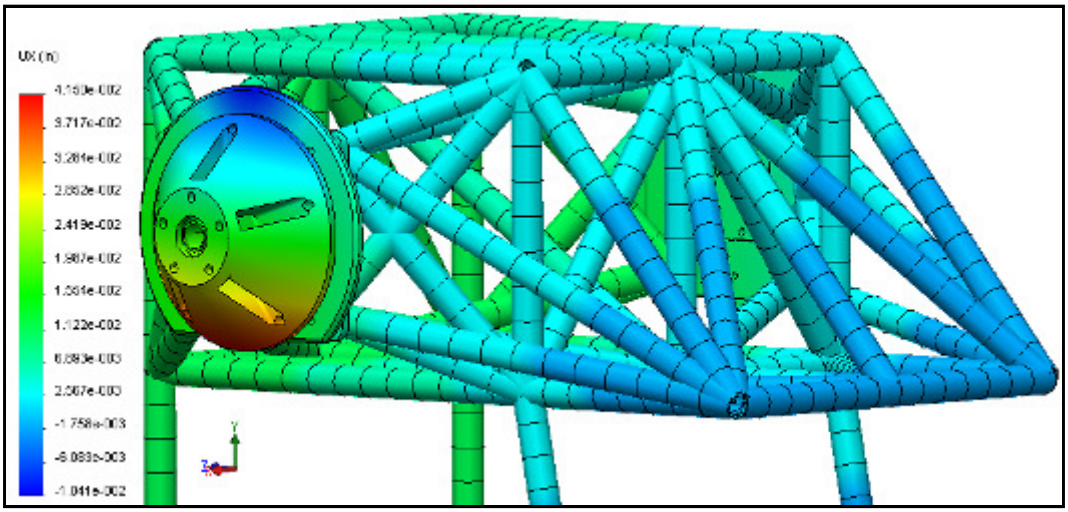

Figure F.18: Frame lateral displacement from lateral loading

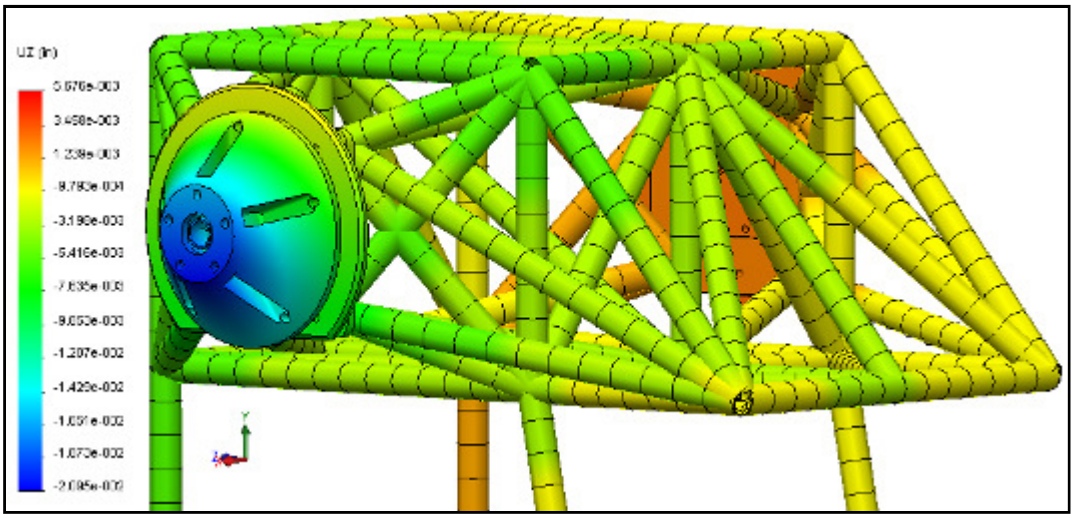

Figure F.19: Frame longitudinal displacement from longitudinal loading

In addition to deflection results, these tests are used to evaluate the stress that is imparted on the test rig frame tubes in order to ensure that no tubes are yielding during loading. In each test axis, no frame tube area is in danger of yielding or fatigue as the minimum factor of safety which exists for all loading conditions in any tube of the structure is 7.

Using the same setup as the static loading testing, a frequency analysis FEA is run on the test rig. The same mesh is used but instead of components being bolted together, they are specified as bonded. The hub is still connected to the hub snout with rigid links and a pin connector is used between the hub and the hub snout mounting plate. The results this FEA show that the first mode and second modes in every test condition are modes of the longer front connecting rods at around 32Hz with the second mode being only slightly higher than the first. These modes are the connecting rod bending in perpendicular planes with the same mode shape being that of a single peak waveform. These first and second mode frequencies are much higher than the maximum planned test frequency of 20Hz. The only component difference between the static and frequency FEA's is the inclusion of a connecting turnbuckle between the front two connecting rods. This turnbuckle FEA layout is shown in Figure F.20 while Figure F.21 gives the 3D representation of the actual turnbuckle rod which joins the two connecting rods for stiffness.

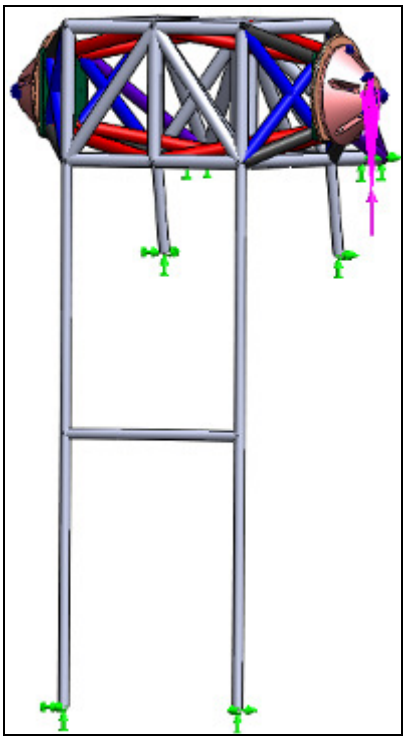

Figure F.20: Frequency analysis structure

Figure F.21: Connecting rod turnbuckle connector

Appendix G: Data Processing GUI Layout

In order to process the test data from the tire test rig, a MATLAB-based graphical user interface (GUI) is created. This GUI allows a user load the raw .tab files output by the K&C rig, visualize the post-processed data, remove outliers in the processed data if necessary, examine trends, fit the data, view fitting results, monitor the performance of the test rig frame over time, and save the results into a formatted .mat structure. This GUI also allows the user to compare the K&C test data to rolling tire test data in terms of stiffness and overturning moment for vertical tests. Files which are generated by the GUI can be loaded back into the GUI in order to view fitting results, processed data, or append new results to the file. This appendix section gives a brief visual tour of the GUI's layout starting with Figure G.1.

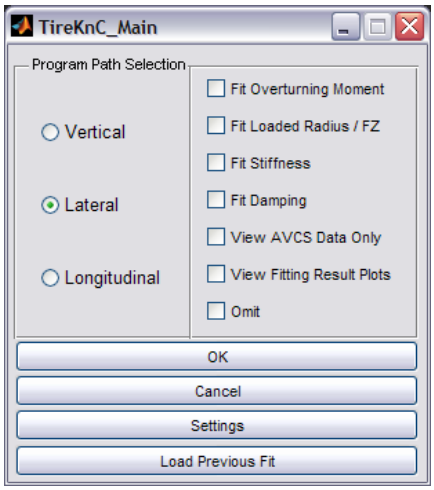

Figure G.1: GUI main window

Figure G.1 shows the main GUI window. This window allows the user to setup the execution path of the program which encompasses viewing and/or fitting the test data or viewing the fitting results from a previous fit from as many of the three test axes as the user desires. Selecting the viewing paths is possible only on an individual basis whereas

all of the fitting paths can be selected at once. By selecting a fitting path, the user must view the processed data and fitting results anyway. In addition to these options a previous fit file can be loaded at this point by clicking the 'Load Previous Fit' button. Loading a previous fit is done in order to append new results to an existing structure or to view the processed AVCS data or fitting results. Selecting the 'Settings' button brings up the window shown in Figure G.2.

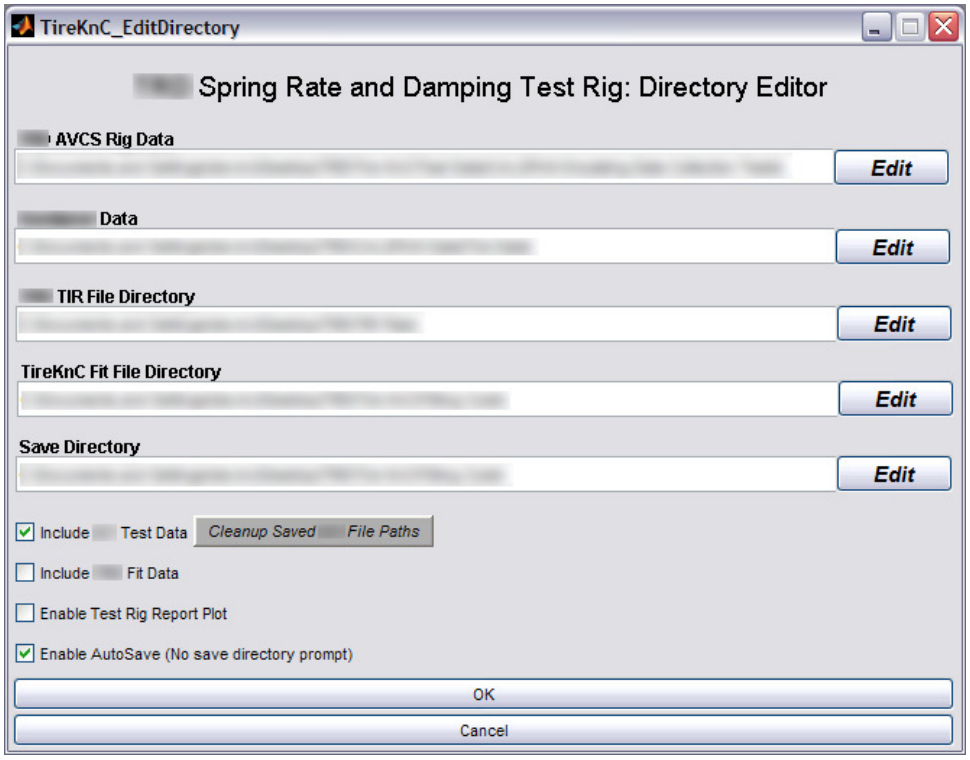

Figure G.2: GUI settings window

In the settings window, default directory locations for prompts throughout the program are adjusted. Other options consist of including rolling tire test and fit data. Rolling tire test data is used to compare to the calculated tire vertical spring rates while the rolling tire fit data is compared against the overturning moment that is measured from vertical testing. The 'Enable Test Rig Report Plot' checkbox brings up a plot at the end of the program which illustrates the vertical, lateral, and longitudinal spring rates of the test

rig, and the possible measurement error induced over time (Figure G.13). 'Enable AutoSave' automatically saves the output data structure into appropriate directory without prompting the user unless another file with the same name exists in the directory.

Once setting selections are complete, the main GUI window reappears and the 'OK' button is pressed to start the body of the program. Figure G.3 shows the next window encountered in the program unless the only the 'View Fit Results Only' or 'Omit' paths are chosen for the program's path. For the case of Figure G.3, loaded radius is being fit in the vertical test axis, and the window displays vertical force versus displacement in SAE coordinates. The tabs at the top of the figure window give the user the option to view displacement, spring rate, damping, or overturning moment for each inclination angle which is tested.

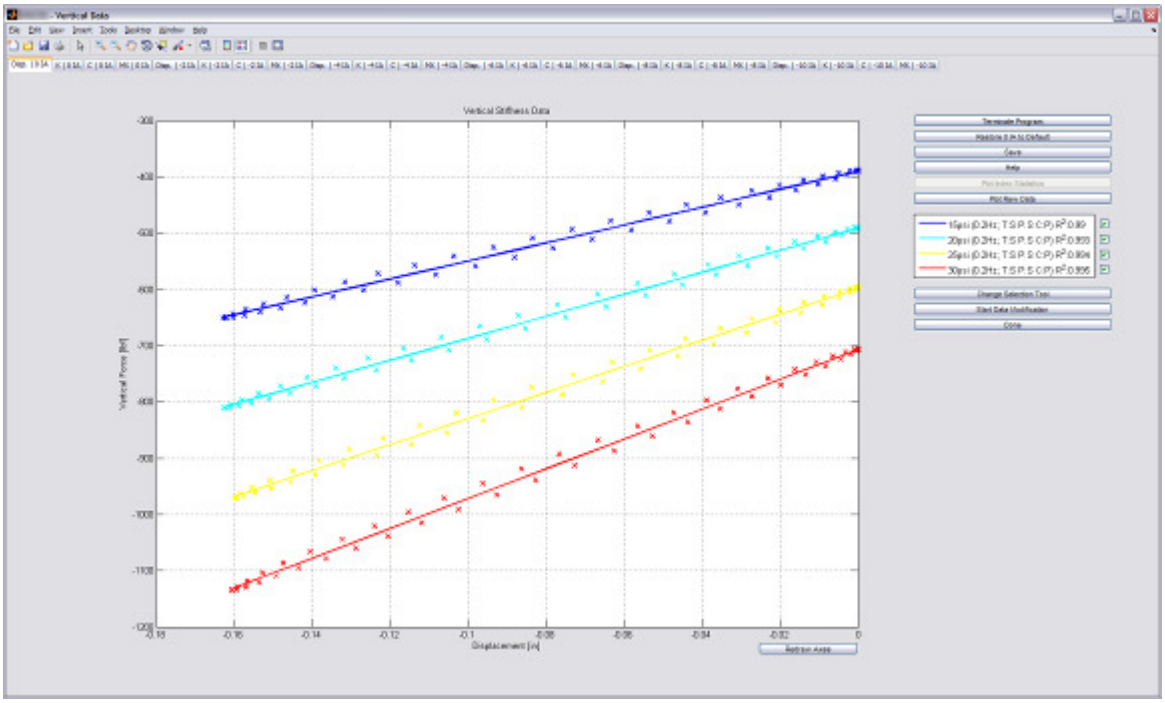

Figure G.3: GUI post-processing window – Displacement results

A number of buttons are available on each displacement tab which include the following:

- Terminate Program – Ends entire GUI operation
- Restore [current inclination angle tab]IA to Default – If the data has been modified in any way, selecting this button will restore the data to exactly that which is output from the K&C rig
- Save – Saves the current post processed data to an output structure
- Help – Provides program assistance
- Plot Index Statistics – Plots the spring rates that are calculated from multiple indices testing. This option is not available if data from only one index is loaded. An example of the plot given by pressing this button is shown in Figure G.5 while Figure G.4 shows the post-processing window with index options. This new table allows the user to switch between the plots of different indices.
- Plot Raw Data – Plots the unprocessed displacement data from the test rig for the inclination angle tab on which this button is pressed as shown in Figure G.6.
- Legend checkboxes – The legend displays information about the data including tire properties, test frequency, and R-squared values. The checkboxes on the side of the legend allow the user to hide a particular

outer liner pressure's data set in the all of the plots in the GUI. The data set which is hidden is the one identified next to the selected checkbox inside the legend.

- Change Selection Tool – Allows the user to change the method of selecting data points to modify.

- Start Data Modification – Begins process where the user is prompted to select data points to remove from the data set. After this process is done, all of the

- Done – Moves the program along to the next axes' post-processing window or onto fitting.

- Redraw Axes – Rescales the axes to better fit the data in the plot window. This option is used typically when a data set is hidden via a legend checkbox.

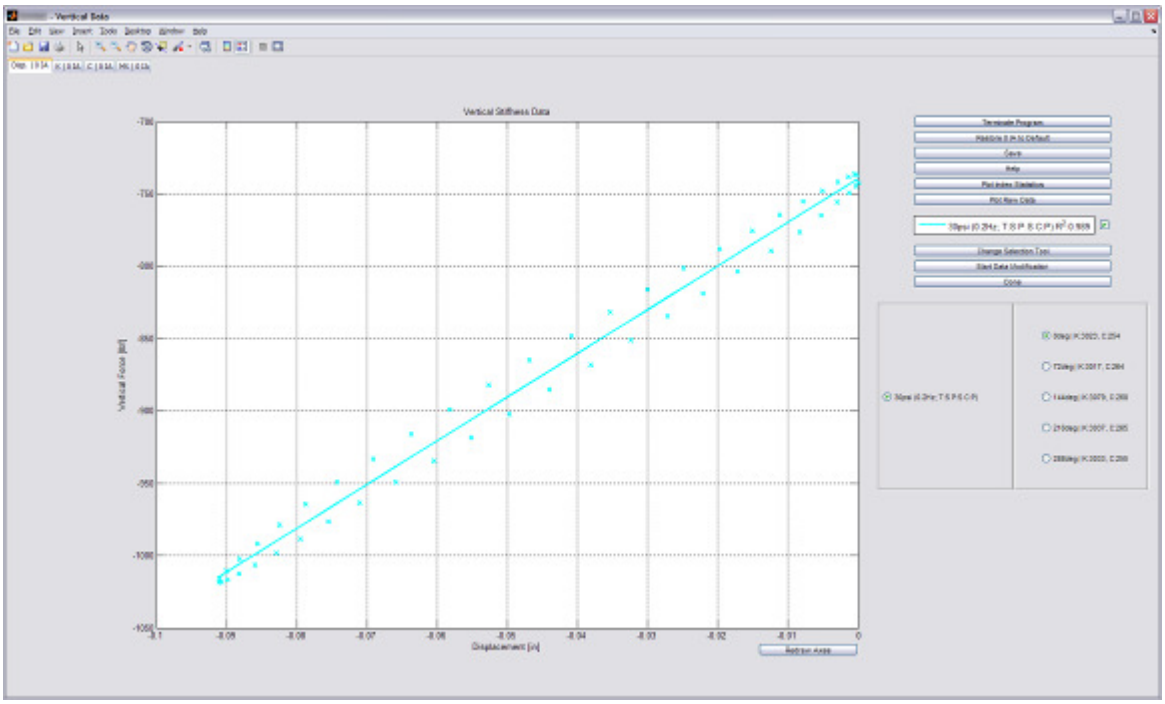

Figure G.4: GUI post-processing window – Index options

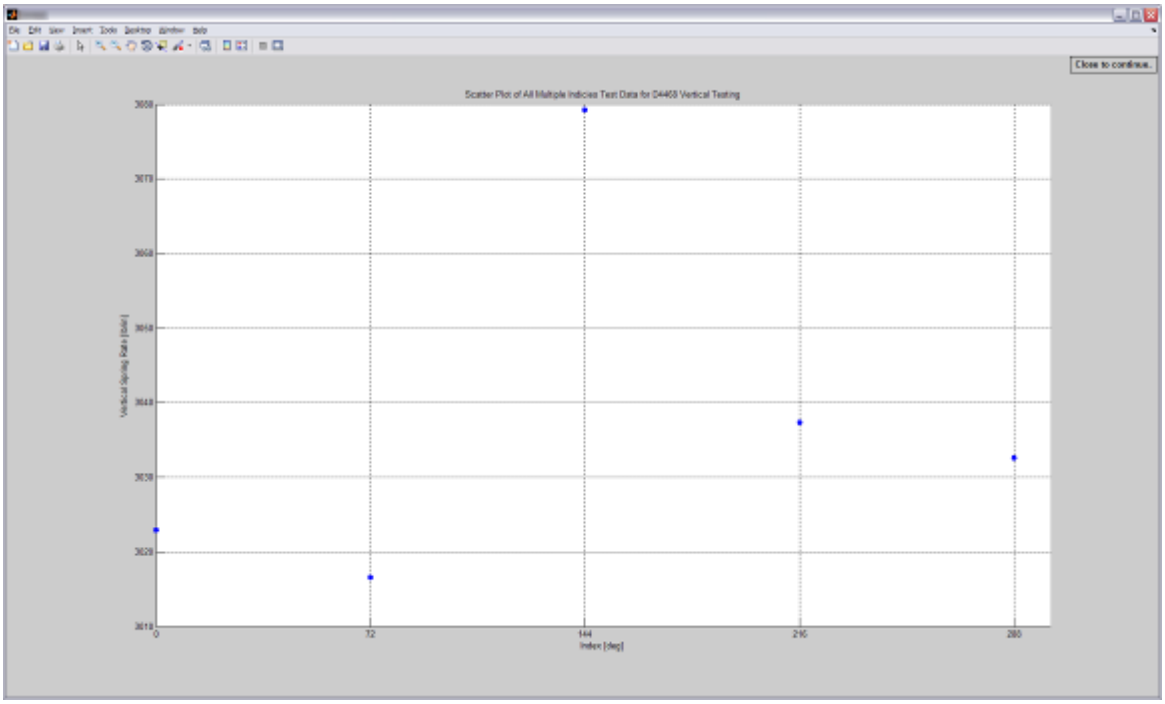

Figure G.5: GUI index statistics window

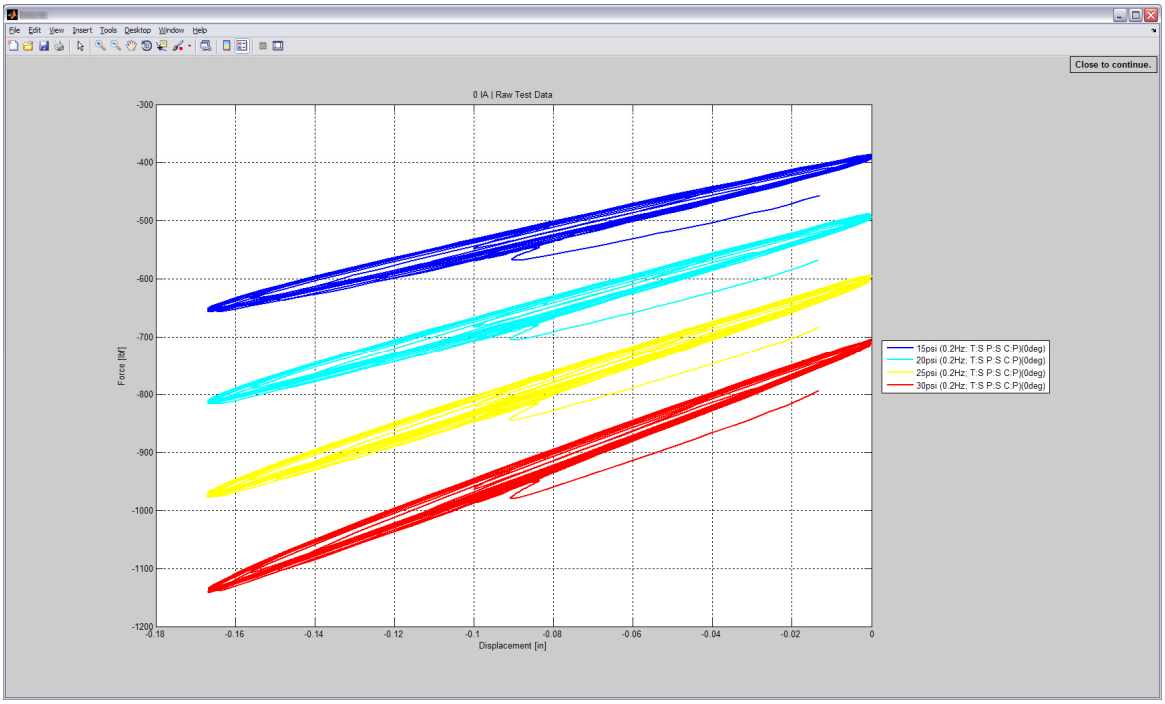

Figure G.6: GUI raw data window

The tabs of spring rate, damping, and overturning moment on the post-processing GUI window are shown in Figure G.7, Figure G.8, and Figure G.9, respectively.

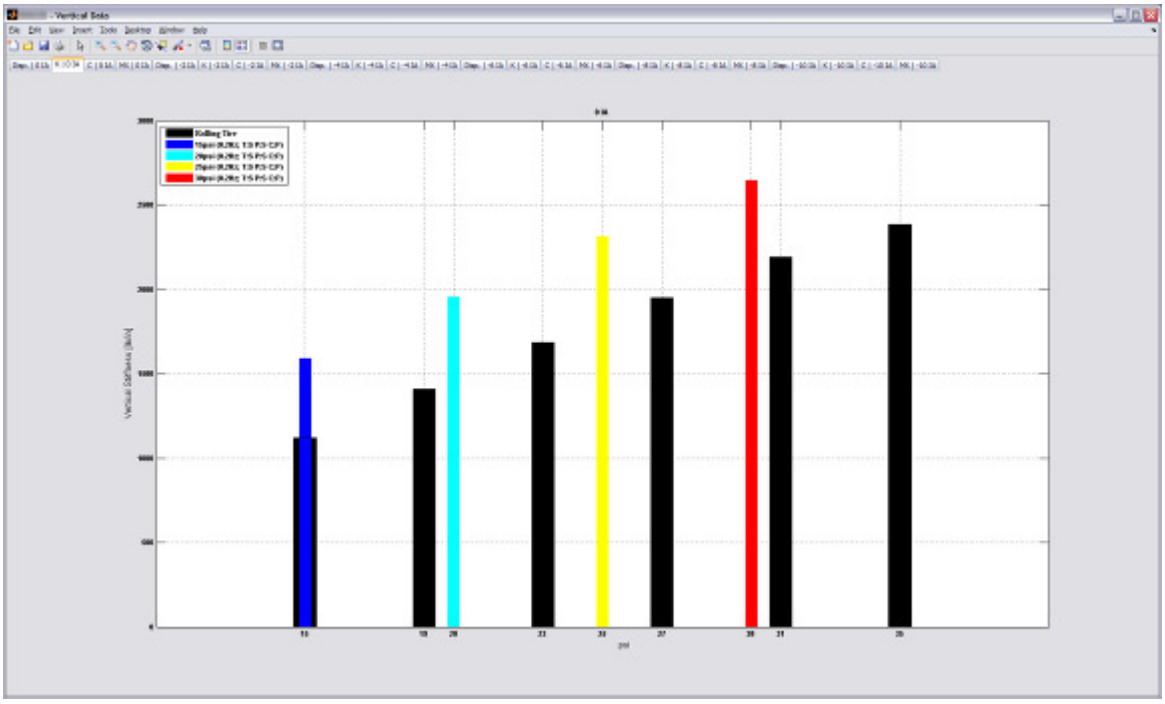

Figure G.7: GUI post-processing window – Spring rate results

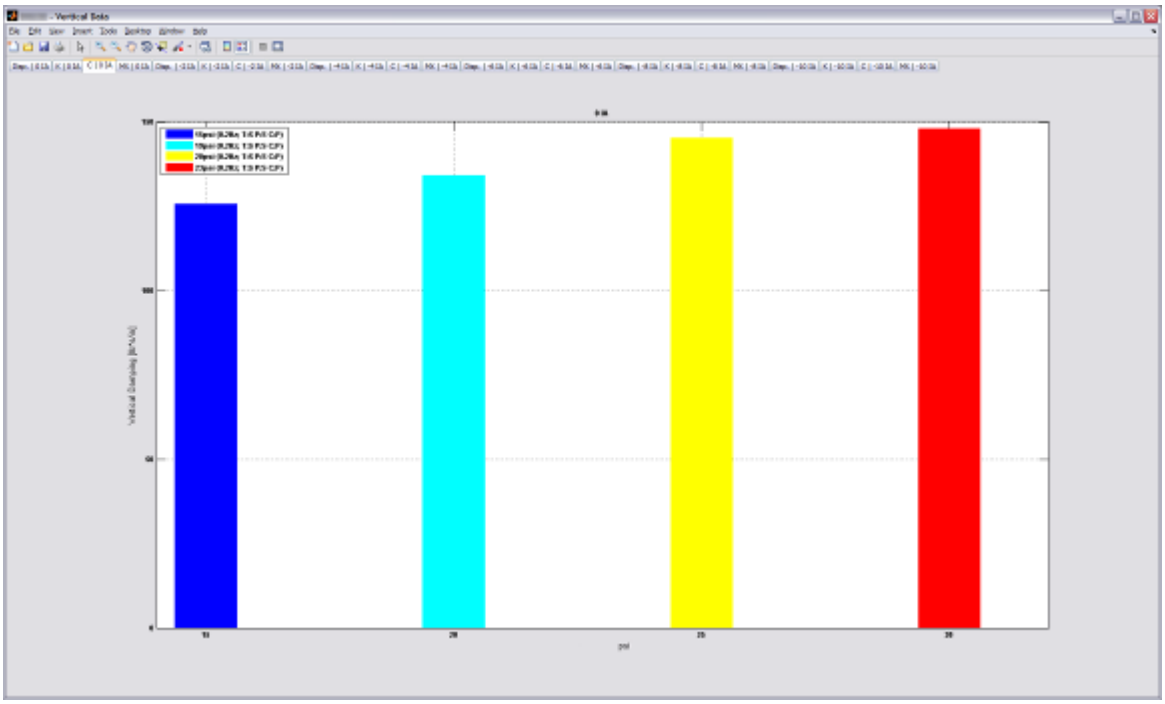

Figure G.8: GUI post-processing window – Damping results

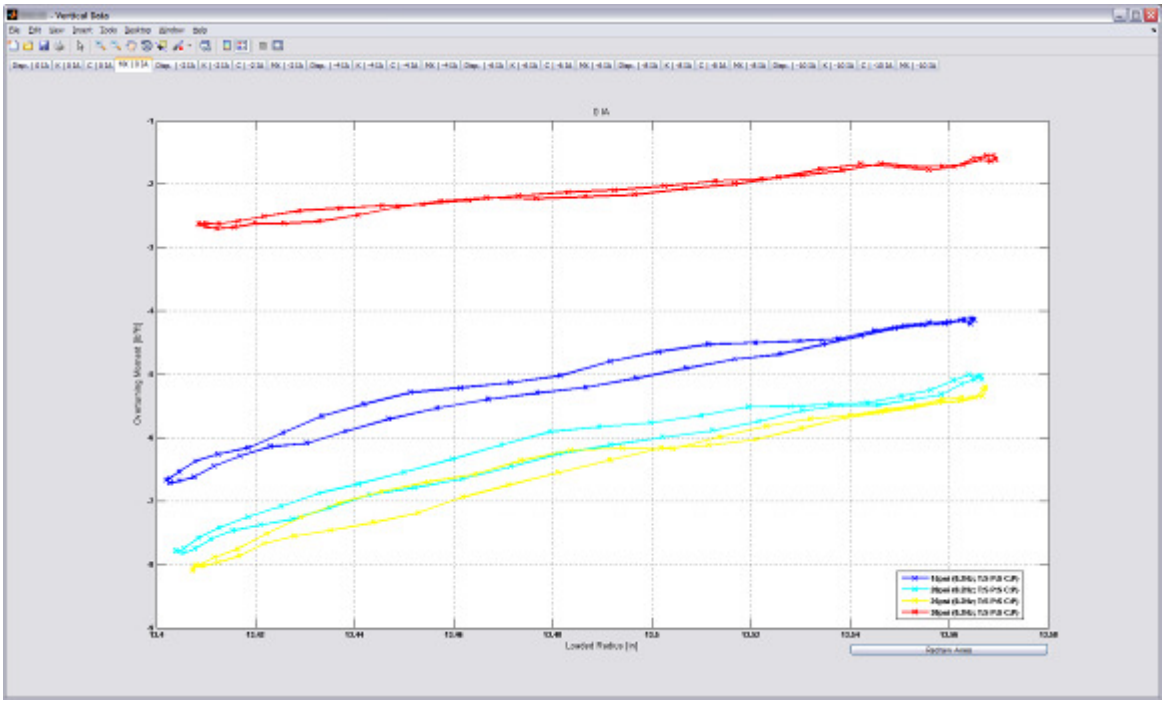

Figure G.9: GUI post-processing window – Overturning moment results

Figure G.7 shows the tire test rig measured spring rate versus the rolling tire data for the project sponsor's race tires. The rolling tire data always shows a spring rate less than that which is measured on the tire test rig due to the dynamics of a rolling on a tire's rubber compound. The other two figures allow for the user to inspect the processed data which is output from the test rig in a simple format considering the large quantity of data input to the GUI from each test.

After the user presses the 'Done' button for the final time depending on the number of axes being fit, the next window to emerge is shown in Figure G.10.

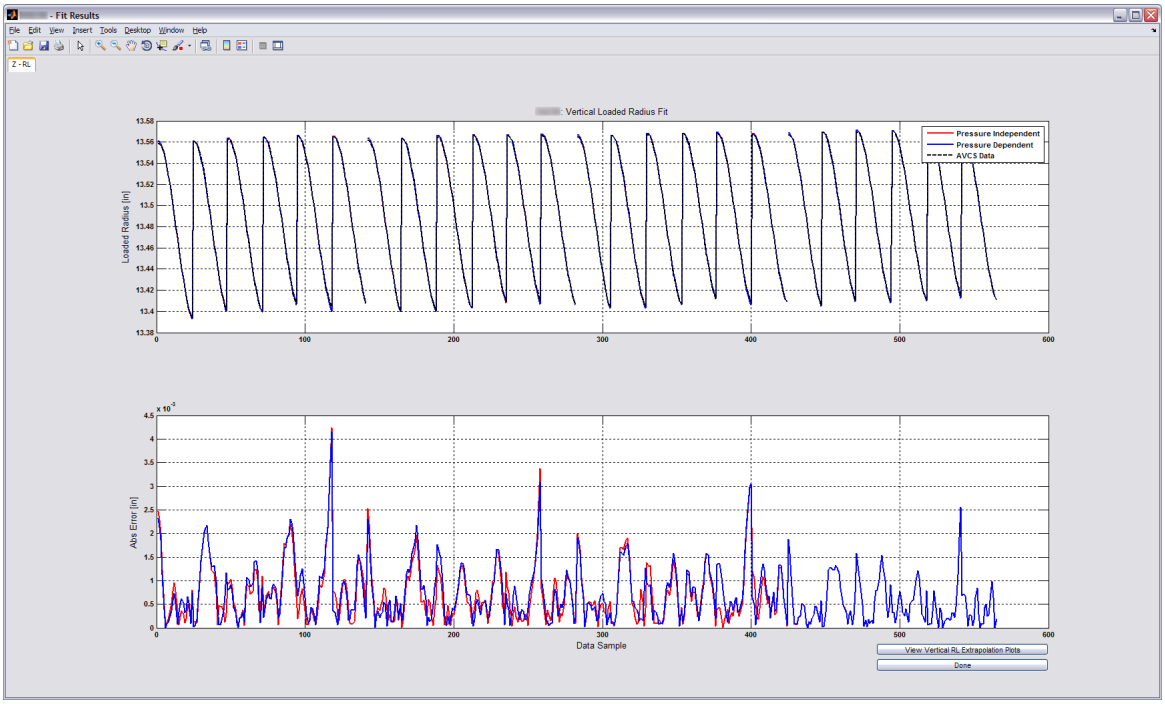

Figure G.10: GUI results window

Figure G.10 displays the results of the fitting routines which are selected by the user in the main GUI fitting window of Figure G.1. The top plot of this figure shows the pressure independent and dependent fitting results with respect to the test data while the bottom plot shows the error for the pressure independent and dependent fits. The buttons

below the bottom plot are for viewing the extrapolation plots for the fit or for the user to indicate that they are done. Figure G.11 gives an example of the window visible after pressing the extrapolation button.

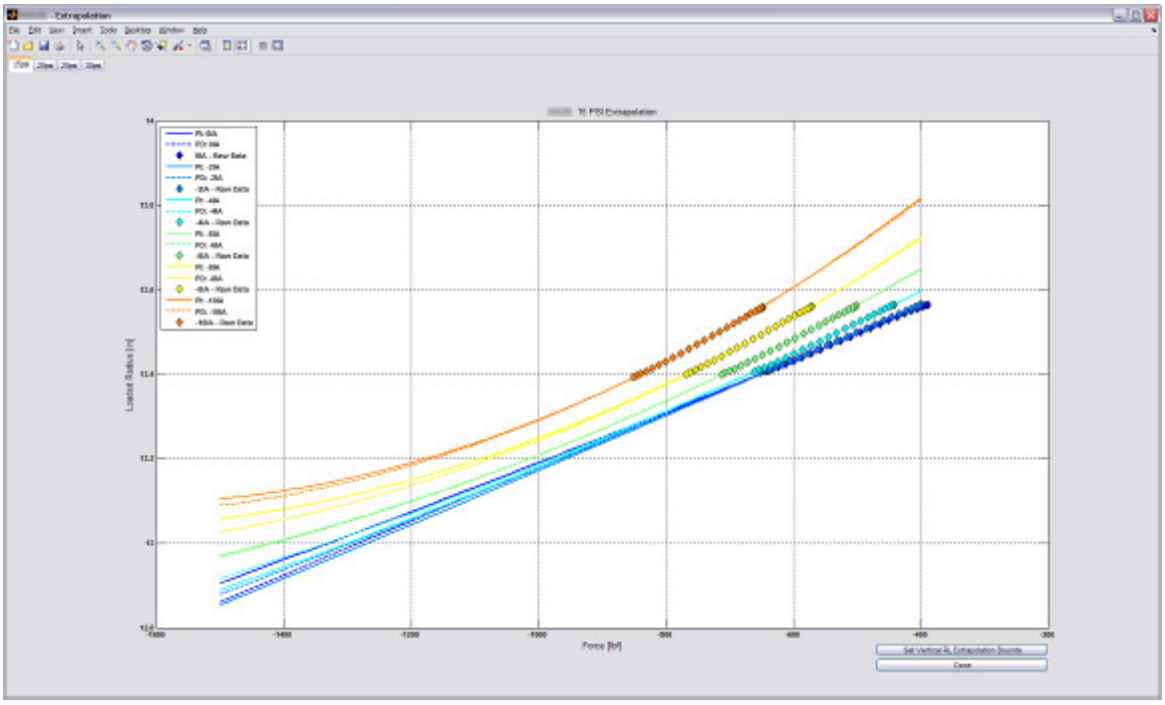

Figure G.11: GUI extrapolation window

Not only can the extrapolation plot limits be adjusted and redrawn, but also the limits for allowable extrapolation for this data in vehicle simulations are adjusted by the 'Set [current dataset] Extrapolation Bounds' button at the button on the x-axis of the plot. The extrapolation limits modification window is shown in Figure G.12

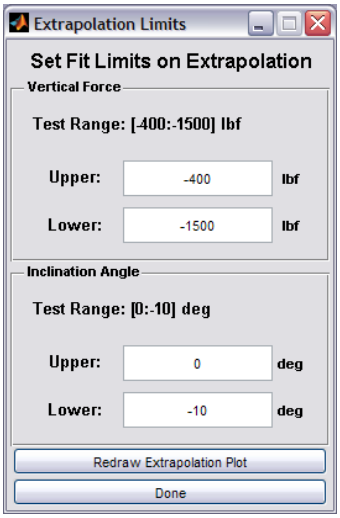

Figure G.12: GUI extrapolation window

Once the user is done with investigating extrapolation and the 'Enable Test Rig Report' option is selected on the settings window at the start of the program, the test rig stiffness report of Figure G.13 is the last window which is generated by the tire test rig GUI program. These test rig report plots allow the user to monitor the stiffness of the test rig on the right and left sides in the vertical, lateral, and longitudinal axes time.

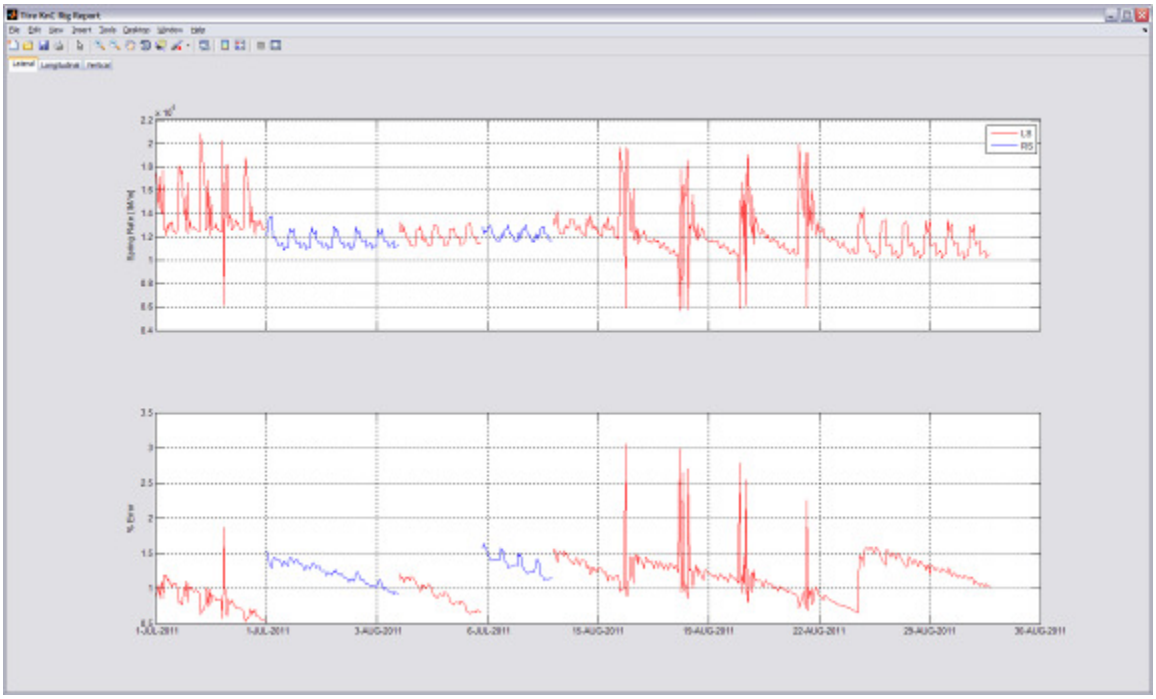

Figure G.13: Test Rig Stiffness Report